

Cascaded Monolithic Fabry-Pérot Filter System for Two-Photon Quantum Interference Experiments

**Diploma Thesis
in fulfilment of the requirements for the degree
Diplom-Physiker**



**Technische Universität Berlin
School II: Mathematics and Natural Sciences
Department of Solid-State Physics**

**authored by
Christoph Berkemeier**

Version: 1.01c

Berlin, August 2013

1. Reviewer: Prof. Dr. Axel Hoffmann
2. Reviewer: Prof. Dr. Oliver Benson

Hiermit erkläre ich, dass ich die vorliegende Arbeit selbstständig und eigenhändig sowie ohne unerlaubte fremde Hilfe und ausschließlich unter Verwendung der aufgeführten Quellen und Hilfsmittel angefertigt habe.

Berlin, den

Unterschrift

Zusammenfassung

In der vorliegenden Arbeit wird die Eignung eines kaskadierten monolithischen Fabry-Pérot Filters für Zwei-Photonen Quanten Interferenz Experimente untersucht. Das Filter System soll dazu dienen, um Photonen aus unterschiedlichen Quellen zur Ununterscheidbarkeit zu filtern. Ununterscheidbarkeit ist eine Voraussetzung, um Experimente wie die Verschränkungsvertauschung von verschränkten Photon durchzuführen. Die Vertauschung von Verschränkung wiederum ist ein zentrales Element eines Quanten Repeaters, der die Quantenkommunikation über weite Entfernnungen ermöglichen soll. Der Quanten Repeater der Quantenkommunikation soll ein Analogon sein zum Signal Verstärker in der klassischen optischen Kommunikation über Glasfasern, weil das Klonverbot den klassischen Verstärker nutzlos macht.

In dieser Arbeit wird der Aufbau und die Charakterisierung eines Fabry-Pérot Filter System wird aus zwei einzelnen Filtern diskutiert. Das Gesamtsystem hat dabei eine Halbwertsbreite von 200 MHz, einen freien Spektralbereich von etwa 500 GHz und eine Unterdrückung von bis zu 60 dB. Für die Anwendung wichtige Parameter, wie die Stabilität der zentralen Filter Transmissions Frequenz und deren Regelbarkeit, werden untersucht und hier dokumentiert.

Um die Einsetzbarkeit als Spektrometer mit einem spektralem Auflösungvermögen von $> 10^6$ aufzuzeigen, wird ein Ausschnitt aus dem Frequenzspektrum einen optischen parametrischen Typ-II Oszillators, der weit unterhalb der Schwelle betrieben wird, vermessen. Dafür werden beide Filter parallel in 40 MHz Schritten verschoben. Das Messergebnis ist dabei in Übereinstimmung mit der Theorie.

Die Ununterscheidbarkeit von Photonen wird mit dem polarisationsabhängigen Hong-Ou-Mandel Effekt untersucht. Dabei werden die Photonenpaare des optischen parametrischen Oszillators gefiltert und ihre Quanten-Interferenzfähigkeit gemessen. Die erreichte Sichtbarkeit ist etwa 97 %.

Abstract

In this diploma thesis the application of a cascaded monolithic Fabry-Pérot filter system for two-photon quantum inference experiments will be studied. The filter system should filter photons from dissimilar sources to indistinguishability. Indistinguishability is a precondition of experiments of entanglement swapping for entangled photons. Entanglement swapping is a core element of a quantum repeater, which enables quantum communication over wide distances. The quantum repeater for quantum communication should be the analogon of the signal amplifier for classical optical communication over fibre, because the No-Cloning theorem renders classical amplifiers useless. In the course of this thesis will be discussed the setup and characterisation of a Fabry-Pérot filter system out of two single filters. The cascaded filters have a full width half maximum of 200 MHz, a free spectral range of about 500 GHz and a suppression up to 60 dB. The stability of the central filter frequency and the tunability are investigated and documented.

To demonstrate the applicability of as a spectrometer with a spectral resolving power of $> 10^6$, a part out of the frequency spectrum by a type-II optical parametric oscillator, far below threshold, will be measured. Both filters will be shifted in 40 MHz steps. The measurement agrees with the theoretical calculation.

The indistinguishability is vital for entanglement swapping. Therefore it will be explored with the polarisation-based Hong-Ou-Mandel effect. The photon pairs of the optical parametric oscillator will be filtered and their capability of quantum-interference will be measured. The result is a high visibility of 97 %.

Contents

1. Introduction	7
2. Quantum Communication	9
2.1. Foundation of Quantum Communication	9
2.2. Encoding and Protocols	13
2.3. Long Distance Quantum Communication	14
3. Fabry-Pérot Filter Cavity Theory	17
3.1. The Beginning of Fabry-Pérot Interferometry	17
3.2. Ideal Fabry-Pérot Interferometer	18
3.2.1. Free Spectral Range	18
3.2.2. Full Width Half Maximum	19
3.2.3. Finesse	20
3.2.4. Suppression	20
3.3. Etalon Stability	21
3.3.1. General ABCD Matrix Properties	21
3.3.2. Applied for a two curved mirrors etalon	23
3.4. The Gaussian Beam in the Etalon	26
4. Monolithic Fabry-Pérot Filter Experiments	28
4.1. Selection of Lenses, FSR and FWHM	28
4.2. Characterisation of the Fabry-Pérot Filters	32
4.2.1. Setup	32
4.2.2. Transmission and Line Width	33
4.2.3. Free Spectral Range	37
4.2.4. Finesse	40
4.2.5. Birefringence	40
4.3. Temperature Tuning	41
4.3.1. Setup	41
4.3.2. Stability	45
4.3.3. Tunability	48
4.3.4. Suppression	51
4.4. Monolithic Fabry-Pérot Filter Conclusion	52
5. Filtering Optical Parametric Oscillator Photons	53
5.1. Quantum Dots	53
5.2. Optical Parametric Oscillator	54
5.3. Optical Parametric Oscillator Experiment	62

5.4. Optical Parametric Oscillator Conclusion	66
6. Hong-Ou-Mandel Effect with Filtered Photon Pairs	69
6.1. Introduction to the Hong-Ou-Mandel Effect	69
6.2. Hong-Ou-Mandel Setup	72
6.3. Results and Discussion	74
6.4. Hong-Ou-Mandel Effect Conclusion	75
7. Conclusion and Outlook	76
7.1. Filtering Quantum Dot Photons	76
7.2. Indistinguishability	76
7.3. Entanglement Swapping	77
A. Derivation of the Ideal Fabry-Pérot Interferometer	78
B. Filter Properties Overview	82
List of Abbreviations	83
List of Figures	84
Publications and Talks	86
Acknowledgement	87
Bibliography	88

1. Introduction

Radio, telephone, and the Internet are the latest technologies, in what originated with letters and telegraphy. Let it be private, business or diplomatic communication, there has always been a demand for protection of the content. At first, simple mechanic cryptographic devices were used to encode messages, but later these developed into complex machines. In the same time, cryptography grew from crossword puzzles into serious mathematical algorithms.

Quantum physics was introduced into cryptography to circumvent one major problem and to solve another. The major problem to circumvent is the unsolved problem of complexity[30, 42, 18, 22], if class $P = NP$. The problem applied to cryptography, describes on an abstract level, whether there is a quick way possible to compute the secret key of most cryptographic algorithms. According to Kerkhoff's principle[35], cryptographic algorithms are designed to rely exclusively on the secrecy of the key, and therefore they could be broken. The One-Time-Pad (OTP) algorithm would not be affected and is a provable secure algorithm[62]. The major drawback of the OTP is the problem of the key distribution, which can be solved with quantum key distribution. Wiesner [71] laid out the path to the first quantum communication scheme. Bennett and G.Brassard [2] designed the first quantum communication protocol, named BB84. It is based on the impossibility to measure the quantum state of a single quantum without disturbance of the state and without the possibility to clone the quantum state of a single photon. Single quanta are not necessarily photons, but photons can be transmitted undisturbed over long distances. Single photon sources[23, 16] have been developed to meet the requirements for secret quantum communication. A more detailed introduction into the concepts of quantum communication will be given in chapter 2.

There are commercial quantum key distribution devices[56, 39] available and the next step will be to build multi node quantum networks over long distances in optical fibres. Optical fibres have inherent losses by scattering and absorption, which limit the maximum distances over which data can be sent. In classical communication, amplifiers can be incorporated every 150 km. Due to the inherent security provided by the No-Cloning theorem, classical amplifiers cannot be used in quantum cryptography. Instead, an automated repeater station needs to be developed. As Briegel et al. [9] noted, quantum repeater nodes are necessary to keep the communication in the regime of quantum physics and thereby secure. Quantum repeaters use the entanglement effect to distribute quantum states beyond the absorption limited reach. They also demand quantum memory to cache communication. Current approaches for entangled photon sources and quantum memories are based on dissimilar photon sources. Therefore the current goal is to build components for a quantum repeater, in which dissimilar sources can be connected - namely by entanglement swapping.

Some common sources for single photons are single atoms[23], ions[43], molecules[46], diamonds[19], quantum dots[44, 58, 76], parametric down conversion[11], and optical parametric oscillators[61]. These sources cover a wide range of wavelengths, with different emission properties such as count rates and bandwidths. Previous experiments in the working group have been operated around a wavelength of 894 nm near the caesium D1-line. This allows the stabilization of lasers to the absorption lines, absolute and relative frequency measurements, and to investigate the interaction between single photons and atoms like electromagnetically induced transparency experiments[27] for quantum memory. An optical parametric oscillator (OPO) operating at this wavelength has been set up for generation of heralded single photons and entangled photon pairs[36, 1]. On the other hand group member Kroh [38] characterised quantum dots (QD) emitting near 894 nm. Recently the entanglement between a quantum dot spin and a photon was shown[12, 20]. Hence both sources are promising single photon sources for a future realisation of a quantum repeater.

A vital aspect of such a repeater station is entanglement swapping[9]. Entanglement swapping does not only work with QDs and OPOs, but this approach would use QDs as a single photon sources in a quantum memory and OPOs as a sources for entangled photons. This is only possible if photons from these two entirely different sources are indistinguishable in every degree of freedom[64]. This implies that the frequency, bandwidth and length, arrival time at the beam splitter, and polarisation need to be indistinguishable. In experimental conditions the wavelength and the bandwidth typically are the most difficult to control, but here efforts towards this goal were made.

During the course of this thesis, a filter system was designed and set up to select a single frequency mode from an optical parametric oscillator, while simultaneously filtering the broader emission of a QD. The theory of Fabry-Pérot filters will be explored in chapter 3, while chapter 4 contains the characterisation of the filters and their performance.

Aside from its application in the quantum communication field, the filter system can be used for high resolution spectroscopy as well. In this work it was applied to analyse an OPO, as can be read in chapter 5.

The mentioned filtering for indistinguishability in the frequency domain demanded another experiment. The measurement of the Hong-Ou-Mandel effect[28] seemed to be a promising endeavour. During the course of this thesis photon pairs of an OPO were frequency filtered and their indistinguishability was manipulated by a half wave plate (HWP). The results will be presented in chapter 6.

2. Quantum Communication

In this chapter follows a introduction into quantum communication. At first the need for quantum communication will be demonstrated at the demands of the One-Time-Pad. The BB84 protocol for quantum cryptography will be discussed and at the end the demand for a quantum repeater for long distance quantum communication.

2.1. Foundation of Quantum Communication

Communication and cryptography have a long common history[34]. In the beginning, the cryptographic algorithms were, by today's standards, rather an obfuscation than a serious hindrance to tap communication. One of these algorithms is still popular today as an example of obfuscation. It is the ROT13 algorithm, which rotates the alphabet with a fixed number of letters. It is said, that Gaius Julius Caesar applied this algorithm. It leaves the probability distribution of the letters intact and allows to be broken with statistical evaluation. Modern algorithms like the American Encryption Standard (AES), ElGamal or RSA resist such blunt attack vectors. But they have their own weaknesses. The key distribution for a symmetric algorithm, such as AES, does not scale with the number of communication partners. Since every communication partner has to exchange a secret key with every other communication partner. Asymmetric algorithms, such as ElGamal and RSA, have a well scaling key distribution, because they use a private-public key system. The public key can be distributed over public communication channels like websites. Their algorithms are based on the inability to compute discrete logarithms or prime factors of large numbers.

Until now, there is no proof that these inabilities can be taken for granted. An algorithm that is proven to be secure, is the One-Time-Pad[62] (OTP). Miller [45] was the first to describe it in the year 1882 and later on it was reinvented by Gilbert Vernam and Joseph Mauborgne. The OTP is a very simple algorithm:

$$\begin{array}{l} (\text{Plaintext} + \text{Key}) \text{ modulo } \text{Alphabet} = \text{Ciphertext} \\ \text{Example: } (101000 + 110000) \text{ modulo } 2 = 011000 \end{array} \quad (2.1)$$

It combines a plain text with a random secret key modulo the number of encoding signs, often called the alphabet, to a cipher text. The alphabet here consists of 0 and 1. The simple algorithm though has high demands for its appliance. First of all, OTP, like all cryptographic algorithms, needs a random key. True randomness is hard to achieve, because there are neither a randomness software, nor an algorithm, nor even a definition of randomness. There are some tests to determine if a given data set is random. To generate true randomness, hardware random generators have been built,

which use thermal noise, lava lamps or photon arrival times[69] or similar processes. Figure 2.1 shows a schematic for a hardware random generator based on photon arrival times. The next demand of OTP is a secret key as long as the plain text. If the key is shorter than the plain text,

Key: BQ (2.2)

Plain Text: P H Y S I K

Applied Key: B Q B Q B Q

the applied key is not random. The least of the demands to mention is that the same key should never be used twice for encryption. Otherwise

Plain Text 1: 100010101 (2.3)

Plain Text 2: 101010010

Key: 100110101

Cipher Text 1: 000100000

Cipher Text 2: 001100111

Plain Text 1 - Plain Text 2: 001000111

Cipher Text 1 - Cipher Text 2: 001000111

both plain texts are related to each other as both cipher texts. This is an unacceptable information leak, which might be used as a hook to break the cipher text. These requirements can be met, but the problem is the distribution of secret keys. For classical key distribution the key must be printed, crafted or saved on a physical object, which could be copied during transport. A breach of the key security cannot be measured, but it is a matter of trust.

In the year 1982 Wootters and Zurek [73] showed that no single quantum can be cloned, which means that the state of a single quantum cannot be read and applied to another quantum without destroying the state of the first quantum. The proof

$$\begin{aligned} \text{Hypothetical Cloning Machine: } & |A_0\rangle |s\rangle \Rightarrow |A_s\rangle |ss\rangle \\ & |A_0\rangle (\alpha|v\rangle + \beta|h\rangle) \Rightarrow \alpha|A_v\rangle |vv\rangle + \beta|A_h\rangle |hh\rangle \end{aligned} \quad (2.4)$$

shows "that the linearity of quantum mechanics forbids such replication and that this conclusion holds for all quantum systems"[73]. If there is a cloning machine in the state $|A_0\rangle$, that clones the polarisation state $|s\rangle$ to $|ss\rangle$, then this machine would clone the photon state $(\alpha|v\rangle + \beta|h\rangle)$ to $\alpha|A_v\rangle |vv\rangle + \beta|A_h\rangle |hh\rangle$. No matter whether the resulting machine states are equal or not, the outcome is not two photons with the state $(\alpha|v\rangle + \beta|h\rangle)$. It is very important, that as long as only single quanta are used for information encoding, the information cannot be cloned. The idea to use single quanta as information carriers for quantum key distribution has been published by Wiesner [71] in 1983. Single quanta are not necessarily photons, but single photons can be transmitted unaffected over long distances. Single photons are defined by their anti-bunching dip of the correlation function $G^{(2)}$ as seen in the upper part of figure

2.2. There exists various sources for single photons like quantum dots (QD)[58, 76], defects in diamonds[19], optical parametric oscillators (OPO)[61] or others[16].

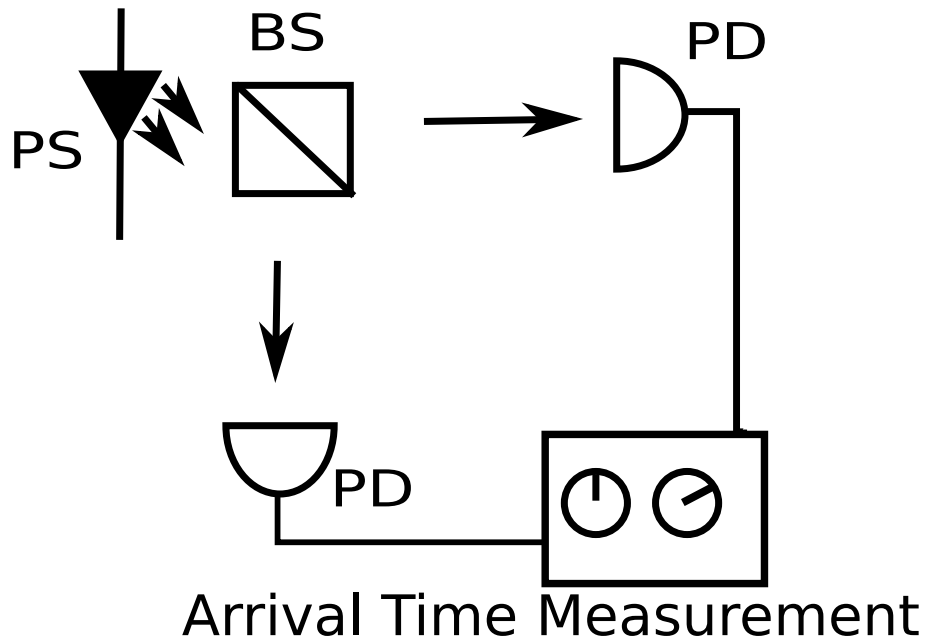


Figure 2.1: Photon Arrival Times Schematic. Photons from a photon source (PS) are sent onto a beam splitter (BS). Behind the beam splitter, the photons are detected in one of the photo diodes (PD). The time difference between both detection events at the photo diodes is used as a source of randomness.

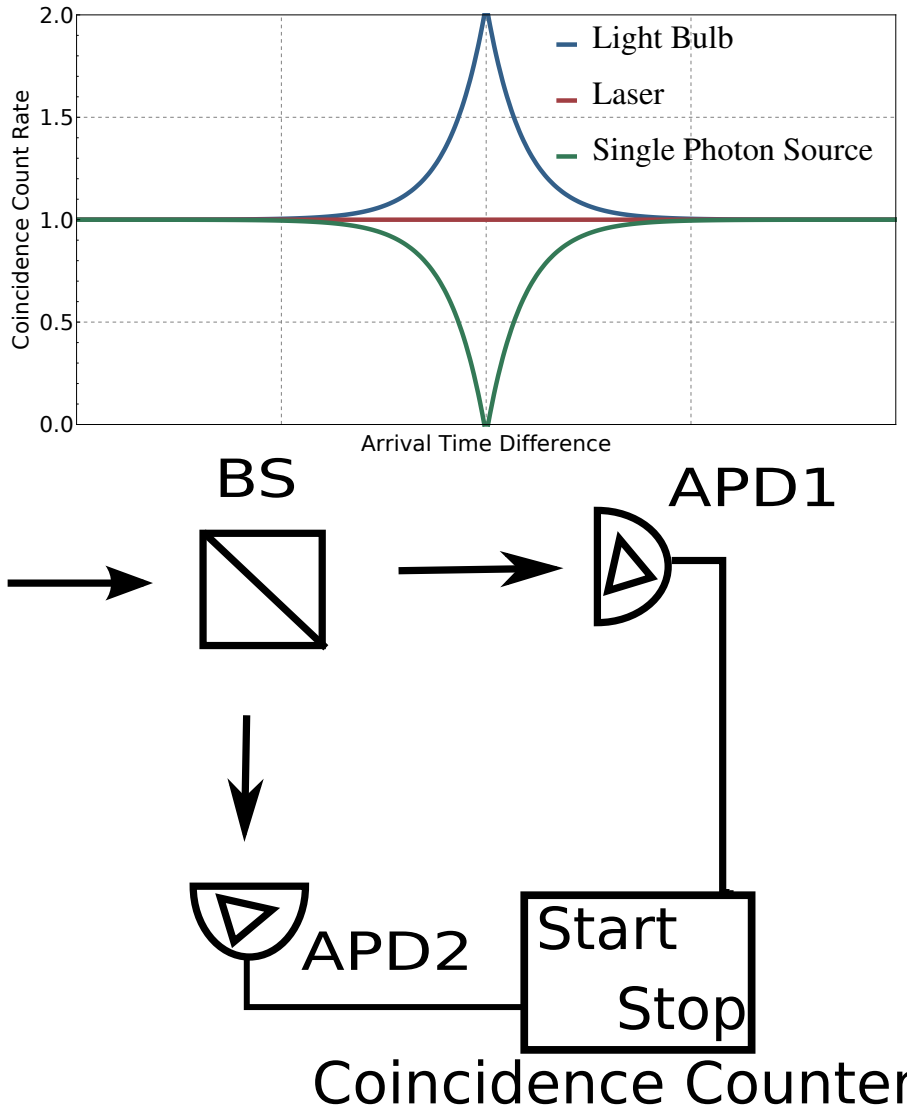


Figure 2.2: Coincidence Count Rates of Different Sources. With the setup below, photons arrive at the beam splitter (BS) and then get detected by either avalanche photo diode APD1 or APD2. The coincidence counter then measures a arrival times difference histogram. For the light bulb the bunching effect can be measured, many photons arrive at the same time. A stable laser source emits a stream of photons with no temporal correlations, that neither bunch nor anti-bunch. For the ideal single photon source, there are measured no coincidences for a certain arrival time difference in an ideal setup. This effect is called anti-bunching, when the probability of another photon event is the lowest right after a photon detection. In an experimental setting, a source can be said to exhibit single photon behaviour when the coincidence count falls below 50 % of the counts outside the dip.[26]

2.2. Encoding and Protocols

Classical information encodings depend on many particles, therefore, they cannot be applied for quantum communication with single photons. One of the first encodings was based on polarising photons. The sender, often called Alice, sends these photons to the receiver, often called Bob, who measures the polarisation of the photons. Quantum key distribution schemes are "used to transmit a supply of random bits between two users, who share no secret information initially"[2]. The message that should be kept secret could be transmitted over public channels, that cannot be altered by an eavesdropper, often called Eve. Charles Bennett and Gilles Brassard published in 1984 the first quantum key distribution protocol BB84[2].

The BB84 protocol utilises polarised photons in two ways. As can be seen in figure 2.3, Alice generates a string of random bits and then randomly decides on photon by photon basis whether to encode the bits either in a diagonal or rectilinear polarisation base. A scheme could be that 315° and 0° encode a 1 and 45° and 90° encode a 0. The photons are then sent to Bob who decides randomly whether to measure in the diagonal or rectilinear polarisation base - also on a photon by photon basis. Alice and Bob compare afterwards the used bases with each other over a public channel, that requires no secrecy. This exchange does not disclose any bit of the key, but instead scrubs the key of bits with non-matching basis.

Eve cannot clone the photons thanks to the No-Cloning theorem, but she can disturb the exchange, which will not stay unnoticed. In a Man-In-the-Middle attack Eve would measure all photons of Alice and send Bob her own pairs. The total error of the transmission would then be generated by Eve guessing the right bases of Alice's photons and by Bob guessing the right bases of Eve's photons. Even if Eve does not interfere with the exchange, some errors would reside. On the one hand there are imperfections of the instruments and on the other hand the transmittance of the polarisation is imperfect, because external effects could rotate it. Error correction schemes are available, but require additional bits, that can not be used for the key. Another idea is to let Bob send a photon to Alice, which is reflected, manipulated and then sent back to Bob[7]. This works as long as the polarisation manipulation is time independent, but doubles the chance of lost transmittance. Other protocols based on the BB84 have been published, which enhance the robustness of the communication by, for example, utilising three instead of two polarisation bases.

There is a number of alternative protocols[17, 3, 32, 33, 66], which emphasise different aspects, and use different methods.

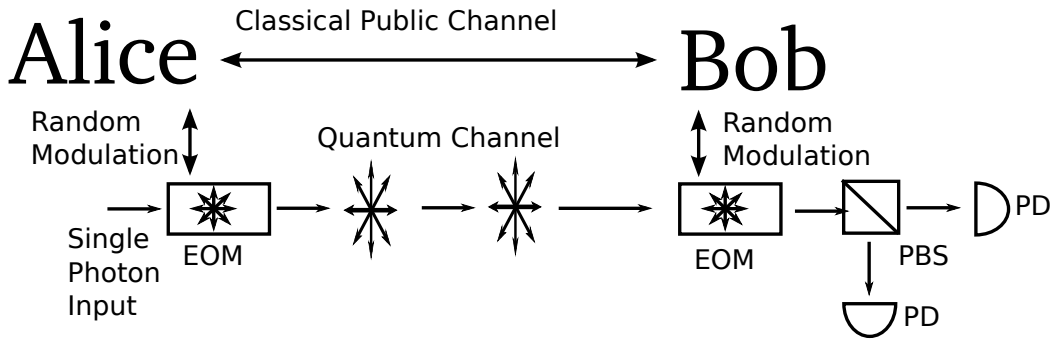


Figure 2.3.: BB84 Protocol. For the BB84 quantum key distribution protocol, the sender Alice encodes a random string with an electro-optical modulator (EOM) on a single photon stream. There are four possible polarization encodings of which each two make up an orthogonal basis. Bob at the receiver modulates randomly the incoming single photon stream with an EOM. If Alice and Bob choose randomly and independently from each other the same basis, Bob can measure the state Alice encoded. For the measurement the photons are split up at a polarizing beam splitter (PBS) and detected by photo diodes (PD) in each arm.

2.3. Long Distance Quantum Communication

One of the latest examples of real world quantum communication devices reaches between 150 km and 200 km of communication distance[67]. There are commercial systems[56, 39] to buy and apply for quantum key distribution, although these are also limited to tens of km. In the long term quantum computers and other, yet to be developed quantum devices, need to be connected over long distances. An option might be a direct communication link in free space. While recent experiments[52] operated at day light and variable weather conditions, the applicability is limited by buildings, mountains, and other obstacles blocking the line of sight, and high losses can severely limit count rates. Existing optical fibres can be used instead, but a signal with even the lowest damped wavelength of 1550 nm will be eventually absorbed. In classical optical fibre networks signal amplifiers are used every 150 km.

Briegel et al. [9] developed the scheme of the quantum repeater to extend the absorption limited distance a photon can travel through a fibre network. The repeaters will consist of quantum memories and entanglement elements, as it can be seen in figure 2.4. The memory elements can be used for network synchronisation and entanglement distillation[75, 14, 74], while the entanglement elements connect different memories. If two such sources are used some distance apart, a Bell State measurement can be performed mid-way. One photon from each source will be destroyed, whereby the two remaining photons (from different sources) will become entangled. In a Bell-state measurement the first two photons are destroyed and the latter two photons are entangled. This process is called entanglement swapping. A precondition of the entanglement swapping are indistinguishable photons. Santori et al. [57] showed indistinguishable photons by a quantum dot single-photon source. The various applications of quantum devices will require dissimilar single-photon sources. To connect these, the quantum network for these sources has to be developed. In the quantum network a chain of quantum repeaters will connect, as it can be seen in figure 2.5, Alice and Bob over

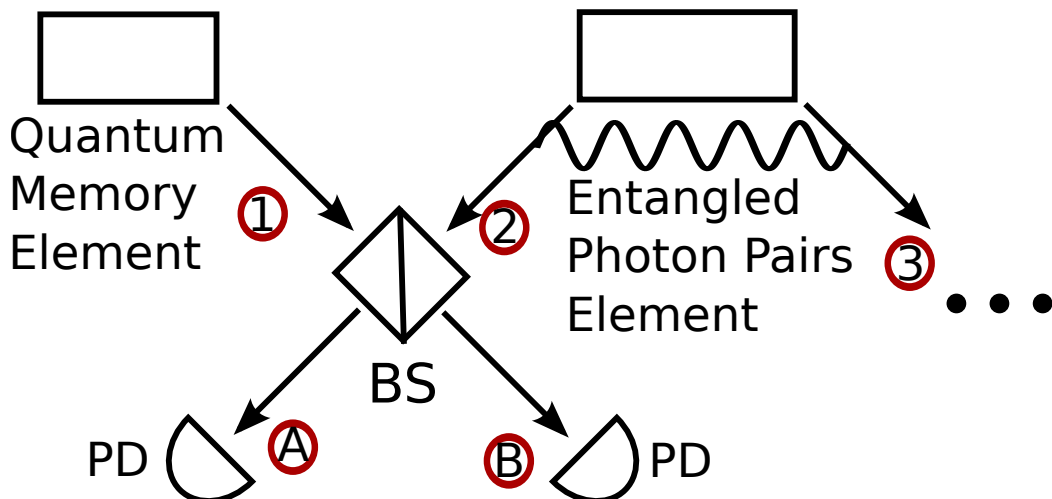


Figure 2.4: *Quantum Repeater Implementation.* For the favoured implementation quantum dots are going to be used as sources for quantum memories and optical parametric oscillators will provide entangled photon pairs. For the entanglement swapping photon ① by a quantum dot and photon ② of an entangled pair by an optical parametric oscillator are sent to a beam splitter (BS). Behind the beam splitter the photo diodes (PD) detect the photon events, which is a Bell-State Measurement. Distinguishable photons are detected either at detector ④ or ⑤ or at both detectors. If photon ① and ③ are indistinguishable, the photons bunch and either ④ or ⑤ register an event, but never both. As the entanglement at the beam splitter determines the state of the photon ③, the information will have been transmitted.

arbitrary distances. An important achievement will be entanglement swapping for dissimilar sources.

Out of the known single-photon sources this working group focuses on OPOs for entangled photons and QDs for memory elements. OPOs are widely tunable sources of photon pairs. The photon pairs are entangled and the OPO can be used in heralded mode, where the measurement of one photon determines the second. An OPO can produce a high count rate of single photons. QDs are highly integrable into fibres or devices. Their emission properties can be tailored to the application, although there are still problems to be solved. The mass production of suitable QDs will be possible with the production lines of the semiconductor industry.

The frequency emittance spectra of OPOs and QDs are broad, and need to be filtered for indistinguishability. One kind of filter is a Fabry-Pérot filter, which selects the frequencies by interference between two mirrors. Here it was decided to use monolithic Fabry-Pérot interference filters[51].

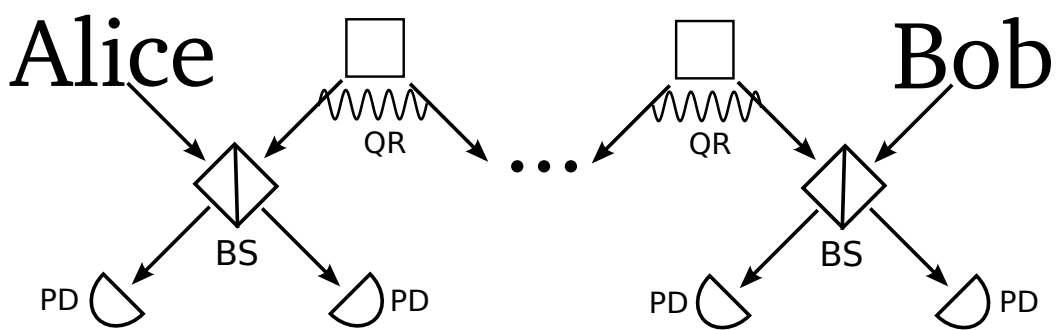


Figure 2.5.: Long Distance Quantum Communication. For quantum communication over distances beyond the absorption limit, Alice and Bob entangle photons with quantum repeaters over Bell-state measurements. The maximum distance between two quantum repeaters depends on the used wavelength and damping in the optical fibre. The C Band of optical fibres is a standardized transmission window between 1530 and 1565 nm, which has the lowest attenuation losses. With a wavelength of 1550 nm and the damping of 0.2 dB/km in widely-used optical fibres, classical amplifiers are distanced from each other about 150 km. Quantum repeater have to have similar ranges.

3. Fabry-Pérot Filter Cavity Theory

After a historic introduction in this chapter will presented the most important equations for the Fabry-Pérot filter. In a second part the Gauss beam in a cavity will be discussed.

3.1. The Beginning of Fabry-Pérot Interferometry

The interference phenomenon of light has been known since a time when physics was still called natural philosophy and the book "Opticks"[47] was published by Sir Isaac Newton in 1704. This long known phenomenon is the core element in the Fabry-Pérot interferometer. The principle setup of a Fabry-Pérot is visualized in figure 3.1. The idea to use measurement interference with two parallel silver-coated mirrors for an interferometer dates back to 1897, when Jean Baptiste Gaspard Gustav Alfred Pérot and Marie-Paul-Auguste-Charles Fabry[53] used it in an interferometer, which is today named after them to honour their achievement. The intended purpose of the interferometer was the measurement of the wavelength of the red cadmium line, which later on, in 1927, was used to define the meter. Fabry, Pérot, Buisson, Benoit and Lummer extended the application range and characterised its spectroscopic abilities in the next years in a series of "brilliant papers"[68]. The physics of these days shared an interest in the novel instrument. For example, Robert John Strutt, later the 4th Baron Rayleigh, used it in his spectroscopic studies and has been credited to recognize the Fabry-Pérot Interferometer as a light resonance cavity. Fifty years later this cavity was proposed to be used in an optical maser[13, 54, 59], which is nowadays known as laser[40]. The laser, consisting of an active medium in a Fabry-Pérot cavity, led to vast new applications. A recent approach utilized a monolithic Fabry-Pérot cavity[51], or etalon, as its central element. A more detailed version of the history can be looked up in Hernandez [24] and Vaughan [68]. While the multiple scientific applications of the Fabry-Pérot are still being developed, the theoretical description of the apparatus even pre-dates its invention by sixty years, when George Biddell Airy developed the function which today bears his name.

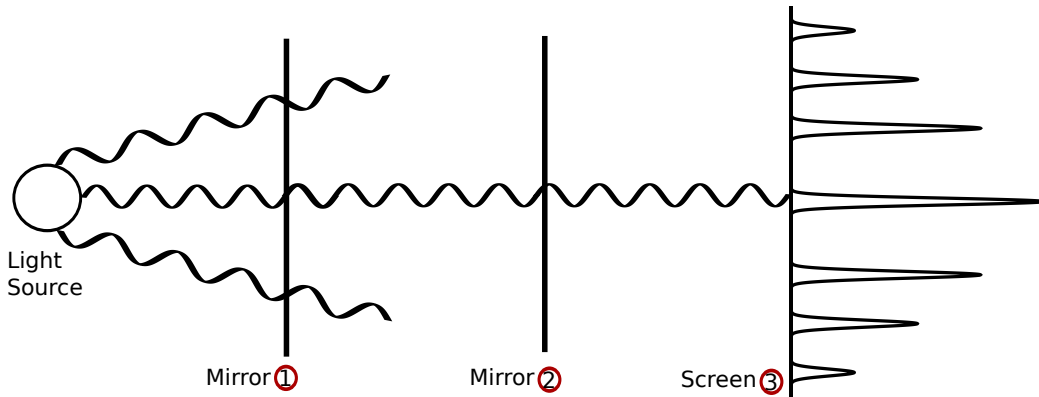


Figure 3.1.: Fabry Pérot Interferometer Principle. The light from a source is coupled into an etalon. The etalon consists out of the two mirrors ① and ②. The resonance condition in the etalon suppress some frequencies and enhances other. The interference pattern can be seen on screen ③. With the known distance between the two mirrors, the wavelength of the emission can be determined.

3.2. Ideal Fabry-Pérot Interferometer

3.2.1. Free Spectral Range

The central order of those maxima in figure 3.1 can be expressed through $n_0 = 2\mu d\sigma$, with the refractive index μ , the distance d between both mirrors and the wave number σ . Multiple orders of maxima are characteristic for interference patterns. The distance relative to the wave number between two neighbouring orders of a wave number is

$$\Delta\sigma = (2\mu d)^{-1} = \frac{\sigma}{n_0} .$$

This definition is called free spectral range since the times Fabry-Pérot interferometers were used to resolve fine structure components of spectra[24]. The definition is very common in the spectroscopic context. Here an equal definition is used instead, which contains the light velocity c and the frequency v by using $\sigma = \lambda^{-1} = \frac{v}{c}$:

$$\text{Free Spectral Range: } \Delta v = \frac{c}{2\mu d} \quad (3.1)$$

Figure 3.2 shows a schematic of a free spectral range (FSR).

The intensity of the reflected light in a Fabry-Pérot can be described through

$$Y_r(\delta) = [2R - 2R \cos \delta] \left[1 + R^2 - 2R \cos \delta \right]^{-1} \quad (3.2)$$

$$(3.3)$$

with the reflectivity R and the phase change δ . The derivation of this equation can be found in the appendix Derivation of the Ideal Fabry-Pérot Interferometer. With $F = \frac{4R}{(1-R)^2}$ and the trigonometric relation $\cos \delta = 1 - 2 \sin^2 \frac{\delta}{2}$ applied to function 3.2

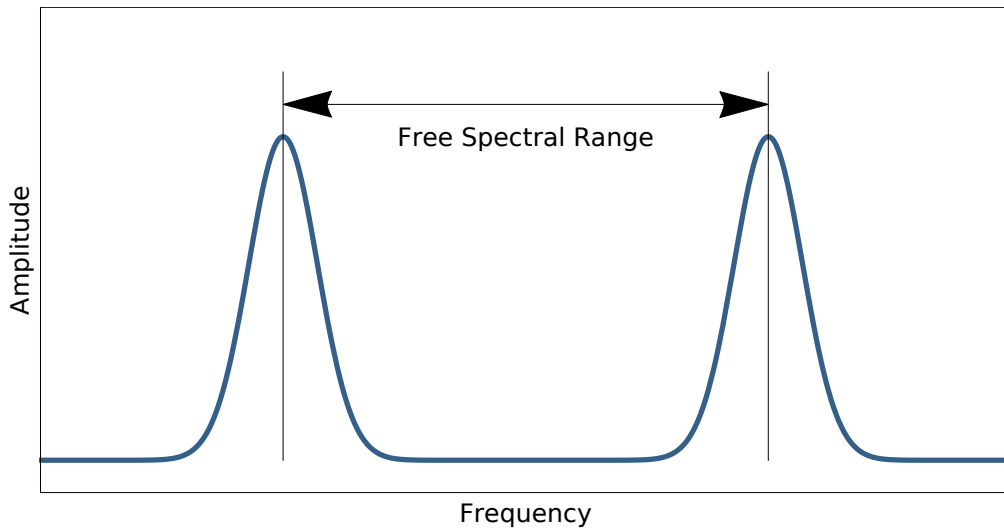


Figure 3.2.: Free Spectral Range Explanation. The free spectral range (FSR) is the distance between two neighbouring peaks.

the mentioned Airy function in its well known form results as:

$$\text{Airy Function: } Y_t(\delta) = \left[1 + F \sin^2 \frac{\delta}{2} \right]^{-1} \quad (3.4)$$

(3.5)

3.2.2. Full Width Half Maximum

Based on the behaviour of the \sin^2 the function 3.4 reaches it maximum,

$$F \sin^2 \frac{\delta_{1/2}}{2} = 1 \Rightarrow F^{-1} = \sin^2 \frac{\delta_{1/2}}{2} \quad (3.6)$$

when $\delta = 2\pi n$ with the integer n . Those maxima are the fringes of the interference and the distance between two neighbouring fringes is 2π . Having this in mind, the half width half intensity follows when the sine term equals 1, because this maximises the denominator of the Airy function. For sufficiently small $\frac{\delta_{1/2}}{2}$, that would be for sufficiently high reflectivity, the approximation

$$\begin{aligned} \sin^2 \frac{\delta_{1/2}}{2} &\approx \left(\frac{\delta_{1/2}}{2} \right)^2 \\ \Rightarrow \delta_{1/2} &= \frac{(1-R)}{\sqrt{R}} \end{aligned} \quad (3.7)$$

is valid and leads to the half width half maximum $\delta_{1/2}$. The full width half maximum (FWHM) expressed in terms of frequency is often used to compare different filters.

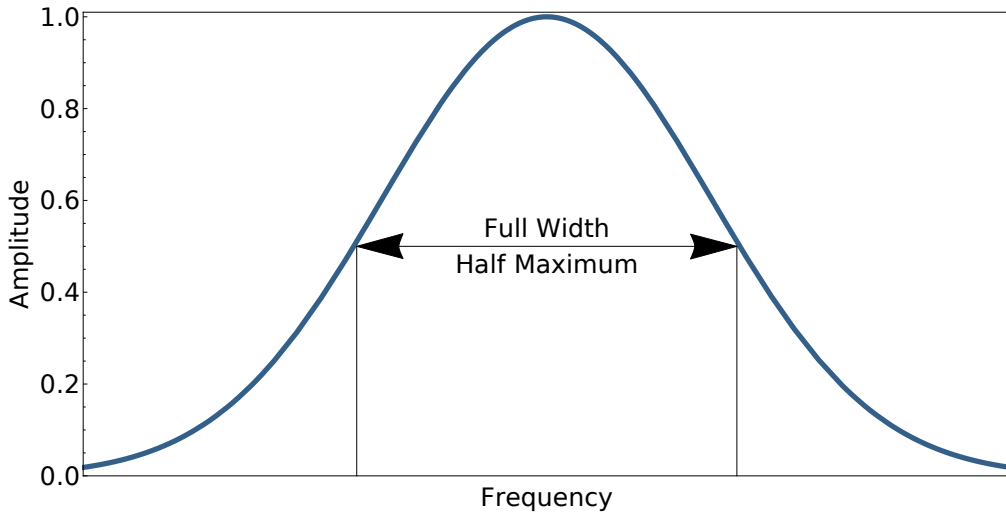


Figure 3.3.: Full Width Half Maximum Explanation. The full width half maximum (FWHM) is the width of a peak at half maximum

With the phase change

$$\delta = \Phi = 4\pi\mu d\sigma \cos \Theta , \quad (3.8)$$

see equation A.18 for details, the FWHM is

$$\text{Full Width Half Maximum: } \Delta v = \frac{(1-R)c}{2\pi\mu d\sqrt{R}} \quad (3.9)$$

An example of a full width at half maximum (FWHM) is outlined in figure 3.3.

3.2.3. Finesse

As mentioned before, the difference between two neighbouring orders is 2π and the finesse

$$\text{Finesse: } \mathcal{F} = 2\pi/2\delta_{1/2} = \pi \frac{\sqrt{R}}{(1-R)} = \frac{\text{FSR}}{\text{FWHM}} \quad (3.10)$$

is defined as the interval between two orders over the full width half intensity.

3.2.4. Suppression

The suppression of a filter is the ratio between the maximum Y_{max} and the minimum intensities Y_{min} passing the filter. An expression for the maximum and minimum intensities can be gained by considering equation 3.4 $Y_t(\delta) = \left[1 + F \sin^2 \frac{\delta}{2}\right]^{-1}$. The extrema

of Y_t are achieved, when the $\sin^2 \frac{\delta}{2}$ function is 0 and 1, therefore

$$\text{Maximum : } Y_{max}(\delta) = 1 \quad (3.11)$$

$$\text{Minimum : } Y_{min}(\delta) = [1 + F]^{-1} \quad (3.12)$$

The ratio is then

$$S = [1 + F] \quad (3.13)$$

$$(3.14)$$

With $F = \frac{4R}{(1-R)^2}$ and using $\frac{4R}{(1-R)^2} \gg 1$ for high reflectivities R the equation then can be simplified to

$$S = \left[\frac{4R}{(1-R)^2} \right]. \quad (3.15)$$

The simplification $4R = 4$ for high reflectivities could be used as well, but this does not reduce the number of terms or variables. Suppression is often expressed in dB and the conversion is $10 \log_{10}(S)$. The logarithm of the suppression is then

$$\text{Suppression: } S[\text{dB}] = 10 \log_{10} \left[\frac{4R}{(1-R)^2} \right] = 10 \log_{10} \left[\frac{2\mathcal{F}}{\pi} \right]^2 \quad (3.16)$$

$$\text{Suppression} = 10 \log_{10} \left[\frac{2\text{FSR}}{\pi\text{FWHM}} \right]^2. \quad (3.17)$$

Expressing the suppression through the finesse \mathcal{F} shows that the smallest FWHM, the highest FSR and the highest suppression can exist at the same time in the same filter. The demands must be balanced depending on the application, which will be discussed later on in chapter 4.1.

3.3. Etalon Stability

3.3.1. General ABCD Matrix Properties

Etalon stability means here that, for the number of round trips, light can be trapped in a cavity. Especially in the case of a plane-parallel etalon, this leads to a requirement of a very fine angle tunability. Historically, that challenge has been overcome, but regarding the stability some non plane-parallel etalons show a better conduct. The stability of a cavity can be deduced by geometric arguments like in Siegman [63], but the approach with ABCD matrices is more flexible. An ABCD matrix describes a linear displacement from the input plane to the output plane for an optical element. For the

path of the ray it uses, the input plane, the output plane, and the respective angles:

$$\begin{pmatrix} r_2 \\ \theta_2 \end{pmatrix} = \begin{vmatrix} A & B \\ C & D \end{vmatrix} \begin{pmatrix} r_1 \\ \theta_1 \end{pmatrix} \quad (3.18)$$

In some publications slopes are used in place of the angles. The determinant of an ABCD matrix is 1 and the eigenvalue equation

$$\text{Determinant: } \det \begin{vmatrix} A & B \\ C & D \end{vmatrix} = 1 \quad (3.19)$$

$$\text{Eigenvalue Equation: } \begin{vmatrix} A & B \\ C & D \end{vmatrix} \begin{pmatrix} r_i \\ \theta_i \end{pmatrix} = \lambda_{k,l} \begin{pmatrix} r_i \\ \theta_i \end{pmatrix} \quad (3.20)$$

is fulfilled. The vector $\begin{pmatrix} r_i \\ \theta_i \end{pmatrix}$ is the vector of the plane and physically important, but for convenience reasons often omitted. When the ABCD matrix respective its eigenvalues $\lambda_{k,l}$ describes the path of a ray through an etalon, a stable cavity requires certain eigenvalues. These eigenvalues are

$$-1 \leq \lambda_{k,l} \leq 1 . \quad (3.21)$$

Transposing the eigenvalue equation

$$\begin{vmatrix} A & B \\ C & D \end{vmatrix} \begin{pmatrix} r_i \\ \theta_i \end{pmatrix} = \lambda_{k,l} \begin{pmatrix} r_i \\ \theta_i \end{pmatrix} \Rightarrow \det \left(\begin{vmatrix} A & B \\ C & D \end{vmatrix} - \lambda \mathbb{1} \right) = 0 \quad (3.22)$$

leads to a quadratic equation

$$\lambda_{k,l}^2 - \text{tr} \begin{vmatrix} A & B \\ C & D \end{vmatrix} \lambda_{k,l} + \det \begin{vmatrix} A & B \\ C & D \end{vmatrix} = 0 . \quad (3.23)$$

The value of the determinant is known and the trace of the ABCD matrix is substituted with $2g$, so that the pq-equation can be used:

$$(A + D)/2 \equiv g \quad (3.24)$$

$$\lambda_{k,l}^2 - 2g\lambda + 1 = 0 \quad (3.25)$$

$$\Rightarrow \lambda_{k,l} = g \pm \sqrt{g^2 - 1} \quad (3.26)$$

In Burch and Gerrard [10] some substitutions are discussed, which would develop this equation further. For the unstable resonator it would be $g \equiv \pm \cosh \theta$ and for the stable resonator

$$g \equiv \cos \theta \quad (3.27)$$

$$\Rightarrow \lambda_{k,l} = \cos \theta \pm i\sqrt{1 - \cos^2 \theta} \quad (3.28)$$

With a trigonometric relation and the Euler formulas this leads to eigenvalues

$$\lambda_k = \exp(in\theta) \quad \lambda_l = \exp(-in\theta) \quad (3.29)$$

for n passes. As long as θ is real, these eigenvalues are between -1 and 1, like previously described. It is now known, that the stability factor g equals $\frac{A+D}{2}$, as introduced in equation 3.24. Therefore, the stability of a complex optical arrangement can quickly be determined, when its ABCD matrix has been computed. ABCD matrices for a lot of typical optical elements have already been derived and Duarte [15] shows an overview. The relevant matrices for the resonator stability are the curved mirror and the flat mirror matrices,

$$\text{Curved Mirror: } \begin{vmatrix} 1 & 0 \\ \frac{-2}{R} & 1 \end{vmatrix}; \text{ Flat Mirror: } \begin{vmatrix} 1 & 0 \\ 0 & 1 \end{vmatrix} \quad (3.30)$$

where the matrix for a flat mirror is the special case for a curvature radius R of infinity. Similarly, the distance L in vacuum is the special case for the distance L in a medium with a refractive index $\mu = 1$.

$$\text{Distance } L \text{ in Medium: } \begin{vmatrix} 1 & L/\mu \\ 0 & 1 \end{vmatrix}; \text{ Distance } L \text{ in Vacuum: } \begin{vmatrix} 1 & L \\ 0 & 1 \end{vmatrix} \quad (3.31)$$

3.3.2. Applied for a two curved mirrors etalon

For the etalon with two curved mirrors the round trip in the cavity begins arbitrarily at a mirror. Therefore are necessary a matrix for the mirror, a matrix for the distance between the two mirrors, another mirror matrix, and another distance matrix. In some cases the radii of both mirrors are different, which should be reflected here by using the distinguishable variables R_1 and R_2 .

$$\begin{vmatrix} 1 & 0 \\ \frac{-2}{R_1} & 1 \end{vmatrix} \begin{vmatrix} 1 & L/n \\ 0 & 1 \end{vmatrix} \begin{vmatrix} 1 & 0 \\ \frac{-2}{R_2} & 1 \end{vmatrix} \begin{vmatrix} 1 & L/n \\ 0 & 1 \end{vmatrix} = \\ \begin{vmatrix} 1 - \frac{2L}{nR_2} & \frac{2L}{n} - \frac{2L^2}{n^2R_2} \\ -\frac{2}{R_1} - \frac{4L}{nR_1R_2} - \frac{2}{R_2} & 1 - \frac{2L}{nR_2} - \frac{4L}{nR_1} + \frac{4L^2}{n^2R_1R_2} \end{vmatrix} \quad (3.32)$$

With $g \equiv (A + D)/2$ the stability factor computes here to

$$g = 1 - \frac{2L}{nR_2} - \frac{2L}{nR_1} + \frac{2L^2}{n^2R_1R_2} = \left(1 - \frac{L}{nR_1}\right) \left(1 - \frac{L}{nR_2}\right) * 2 - 1 \quad (3.33)$$

$$g_1 \equiv \left(1 - \frac{L}{nR_1}\right); \quad g_2 \equiv \left(1 - \frac{L}{nR_2}\right) \quad (3.34)$$

In the literature [63] the terms in parentheses of equation 3.33 are often identified as the g parameters g_1 and g_2 and they fulfil the stability condition

$$0 \leq g_1 g_2 \leq 1 . \quad (3.35)$$

The zones of stability can be visualised in the stability diagram of $g_2 = 1/g_1$, which consists of two hyperbolas in the second and the third quadrant as can be seen in figure 3.4. Some coordinates of significant etalons were derived from equation 3.33.

$$\text{Concentric: } g_1 = -1; \quad g_2 = -1 \quad \text{Confocal: } g_1 = 0; \quad g_2 = 0 \quad (3.36)$$

$$\text{Planar: } g_1 = 1; \quad g_2 = 1 \quad (3.37)$$

Those etalons are at the edge of stability. The arbitrarily selected configurations of a convex convex and a plano-convex etalon are better embedded in the stability zone and hence more favourable.

$$\text{Convex-Convex: } g_1 = 1/2; \quad g_2 = 1/2 \quad (3.38)$$

$$\text{Plano-Convex: } g_1 = 1; \quad g_2 = 1/2 \quad (3.39)$$

The Gaussian character of a real beam, which will be discussed in the next section, has not been accounted for yet.

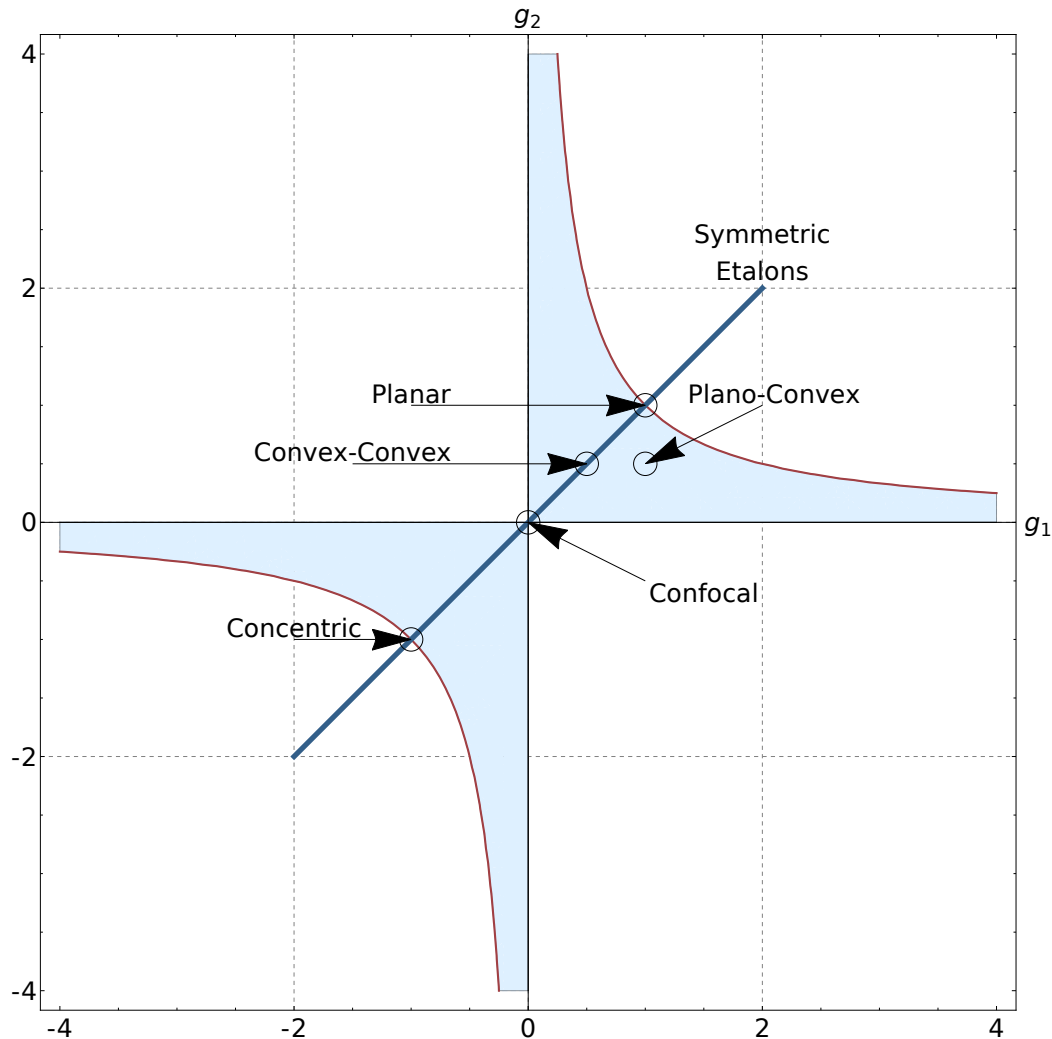


Figure 3.4: *Etalon Stability Diagram.* The g_1 and g_2 combinations of all stable resonator are inside the blue highlighted zone. For a better presentation the upper and lower limit of g_1 and g_2 have been arbitrarily chosen.

3.4. The Gaussian Beam in the Etalon

Until now, the shape of the beam has been implicitly assumed to be a well behaving paraxial type. The beam of a laser or an optical parametric oscillator, has a Gaussian character and only at infinite distance a Gaussian becomes a paraxial beam. The Gaussian beam can be described with the complex beam parameter q , which is defined by the curvature R , the beam spot size ω , the wavelength λ_0 and the refractive index n .

$$\frac{1}{q} = \frac{1}{R} - \frac{i\lambda_0}{n\pi\omega^2} \quad (3.40)$$

The imaginary term q is an additional phase shift of the Gaussian beam. The ABCD law

$$q_2 = \frac{Aq_1 + B}{Cq_1 + D} \quad (3.41)$$

combines the known ABCD matrices with the q parameter. As Bergmann, Schaefer, and Niedrig [5] note, this law is for near paraxial rays and ignores lens errors. Here q_1 would be the input parameter and q_2 the output parameter. A resonator, like many other optical systems, can be translated into an optical system with lenses. The ABCD matrices describe a resonator as being identical to a long chain of equal lenses. The latter setup though makes it easier to understand, that the input q_1 and output parameter q_2 must not differ for a stable resonators. It follows

$$\Rightarrow q^2 + \frac{(D - A)}{C}q + \frac{B}{C} = 0. \quad (3.42)$$

As before with equation 3.25 the pq-formula can be used.

$$q_{k,l} = \frac{D - A}{2C} \pm \sqrt{\frac{(D - A)^2}{4C^2} - \frac{B}{C}} \quad (3.43)$$

A rewriting and usage of the matrix determinant equals 1 (equation 3.19) leads us to

$$q_{k,l} = \frac{D - A}{2C} \pm \sqrt{\frac{1}{C^2} \frac{D^2 + A^2 - 2AD - 4BC}{4}} \quad (3.44)$$

$$q_{k,l} = \frac{1}{C} \left(\frac{D - A}{2} \pm \sqrt{\left(\frac{A + D}{2} \right)^2 - 1} \right). \quad (3.45)$$

A substitution would not, unlike before, isolate the stability condition clearer. As the definition of q in equation 3.40 consists of the curvature and an imaginary phase shift, the root must deliver the imaginary part. The stability condition for the gaussian

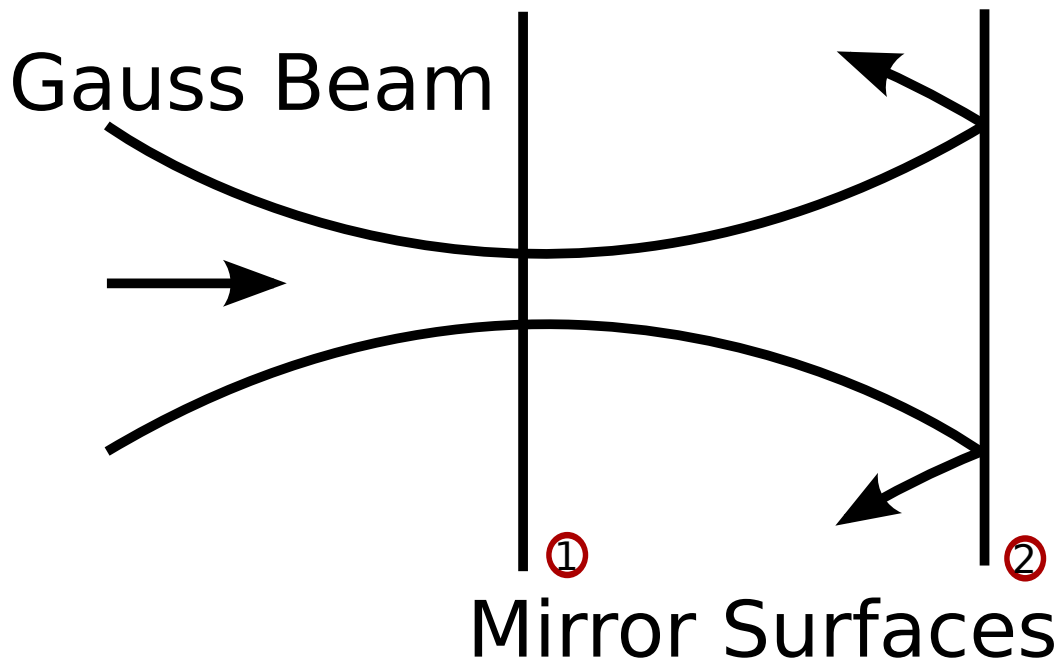


Figure 3.5.: Gaussian Beam in the Plan Parallel Cavity. The gaussian beam couples in at mirror surface ①. The beam reflexes at mirror surface ②. As the incidence angle is not 90° , the reflected beam waist is more wide than of the incoming beam. In the plan parallel etalon gaussian beam map not on each after one or many round trips and therefore this cavity is not stable for such beams.

resonator

$$\text{Gaussian Stability Condition: } -1 > \frac{A + D}{2} < 1 \quad (3.46)$$

is then similar to the paraxial beam condition (equation 3.21) one. The difference is that the limits are missing in the stability condition. As a consequence, the concentric and the planar etalon are no stable resonators for Gaussian beams. For the plane-parallel case, this has been visualised in figure 3.5. This reason and the high availability motivated to use plane-convex lenses. The setup will be discussed in the next chapter.

4. Monolithic Fabry-Pérot Filter Experiments

Spectra by single photon sources can have different characteristics. In general, a single narrow mode is desirable for further experiments such as entanglement swapping, and for uses in a quantum repeater. In the following chapter monolithic filters with coated lenses, as published by Palittapongarnpim, MacRae, and Lvovsky [51], are set up. These can be cascaded to enhance the suppression and the FSR. They are designed to be operated near a caesium absorption line. The caesium absorption will be used to scale measured frequencies. Temperature tuning of the filters is chosen for flexible tuning of the central filter frequency. The stability and repeatability of the central filter frequency will be determined.

4.1. Selection of Lenses, FSR and FWHM

The step from the traditional Fabry-Pérot setup with two silver-coated mirrors to a monolithic Fabry-Pérot filter entails several advantages. Commercial lenses are shaped with high perfection, with typical surface aberrations on the order of $\lambda/10$. The monolithic variant is intrinsically stable, while the two mirror version needs to be stabilized with respect to each other, and one mirror needs to be movable (e.g. using a piezo actuator) to adjust the FSR. Adjusting the FSR for the Fabry-Pérot lens filters is possible by heating the lens, thereby adjusting the optical path length of the etalon. This tuning method does not create much stress in the material. Two mirror Fabry-Pérot setups, even when steered by a piezo, are difficult to fabricate with small thickness. There are several few mm lenses commercially available, thus allowing a large FSR. These features made the monolithic Fabry-Pérot interesting for us. Various decisions were made in the design to suit the intended purpose.

In previous achievements of the working group, light sources near the caesium D1-line of 894.59 nm had been designed, hence this was the target wavelength for the experiments. Therefore a selection criterion of the lens material is the transparency at 894.59 nm. Birefringence in this material would have made optimisation challenging, therefore no or very low birefringence was another criteria. As mentioned above, the cavity should be tuned by temperature, which led to the requirement of a good thermic expansion. Commercially available borosilicate glass (BK7) is a material, that shares all these properties.

The shape of the lens should allow the stability of the Gaussian beam and the suppression of higher modes. As derived in the last chapter the Gaussian beam is unstable in the plane-parallel lens and the convex-convex lens is difficult to adapt to a heat el-

ement, hence the plane-convex shape, as shown in figure 4.1, was selected. The beam stability is fostered by a curvature as big as possible, which limits the minimum thickness of the lens. The thickness of the lens directly influences the

$$\text{FSR: } \left(\frac{c}{2\mu d} \right) \quad (4.1)$$

and the

$$\text{FWHM: } \left(\frac{(1-R)c}{2\pi\mu d\sqrt{R}} \right) . \quad (4.2)$$

The FWHM is a very important property of a filter and was selected for the meant application. A broad filter of about 500 MHz was needed, which should filter the OPO photons to match its comb lines FWHM of about 100 MHz. A 100 MHz filter was required for the QDs, as their signal is comparable very broad and unmodulated. Figure 4.2 shows the result of the FWHM over reflectivity calculation for some linewidths. As figure 4.3 shows the FSR is inversely proportional to thickness. Figure 4.4 presents, that suppression is enhanced by a high finesse, which is obtained by applying high reflectivity coatings. For obtaining a higher curvature and a small thickness, a 2.6 mm lens for the 100 MHz FWHM filter and 3.6 mm lens for the 500 MHz FWHM filter were chosen. The suppression of the filters were estimated around 40 dB and FSRs around 30 GHz. As the complete OPO comb was about 100 GHz wide, it was planned to improve the FSR of the filter system by cascading two filters. As reflectivities could not be applied with arbitrarily high accuracy, the Beschichtungslabor TU Berlin aimed at 99.1 % reflectivity for the 2.6 mm lens and 94.5 % reflectivity for the 3.6 mm lens.

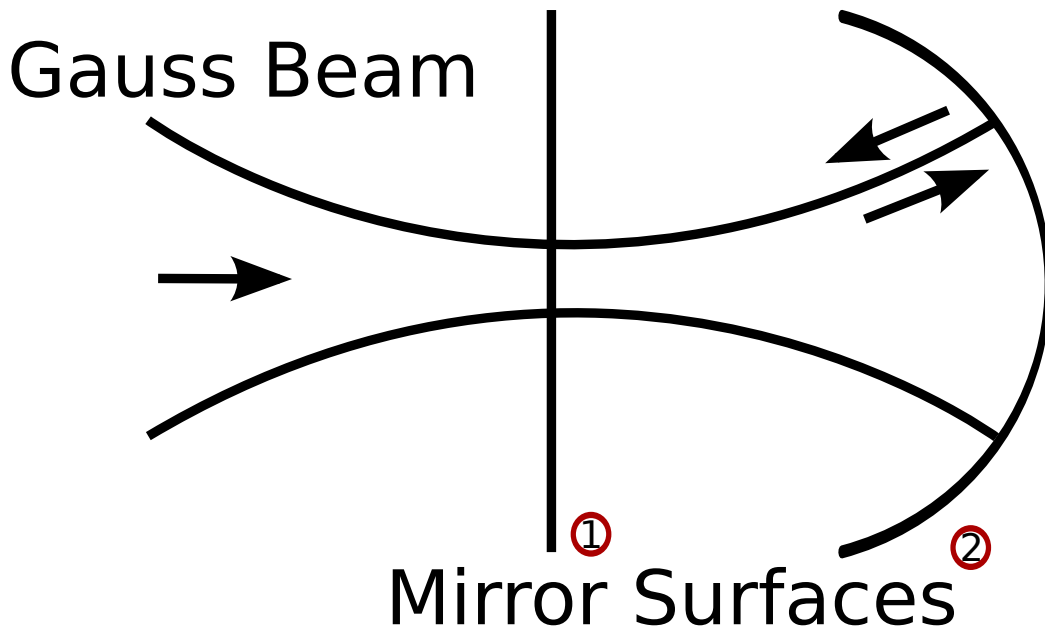


Figure 4.1: *The Plan-Convex Lens.* Optical imperfection aside, the light, coming from the left, reflects at the mirror surfaces (2). As the incidence angle is at least very near to 90°, the incoming and the outgoing beam map on each other. The plan-convex lens was selected as a basis for the filter, because on the one hand the Gaussian beam is stable in the cavity and on the other hand the plan side is adaptable to a Peltier element for heating.

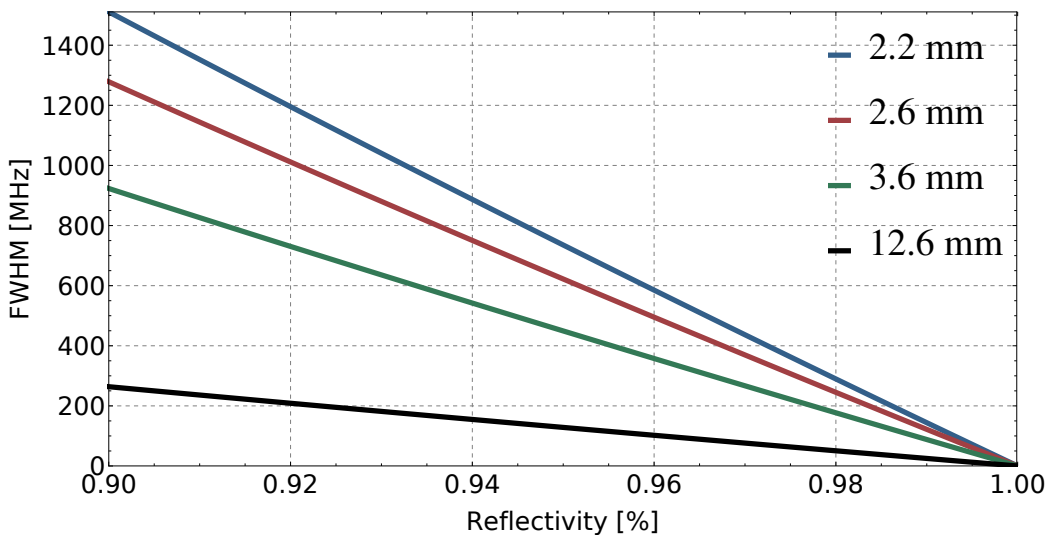


Figure 4.2: *Full Width Half Maximum over Reflectivity.* The FWHM was calculated with equation 3.9 for reflectivities between 90 % and 99.99 % of some commercial available plano-convex lens thicknesses. The smaller thicknesses have a higher dynamic range, while thicker lenses are less sensitive to the reflectivity deviation regarding the FWHM.

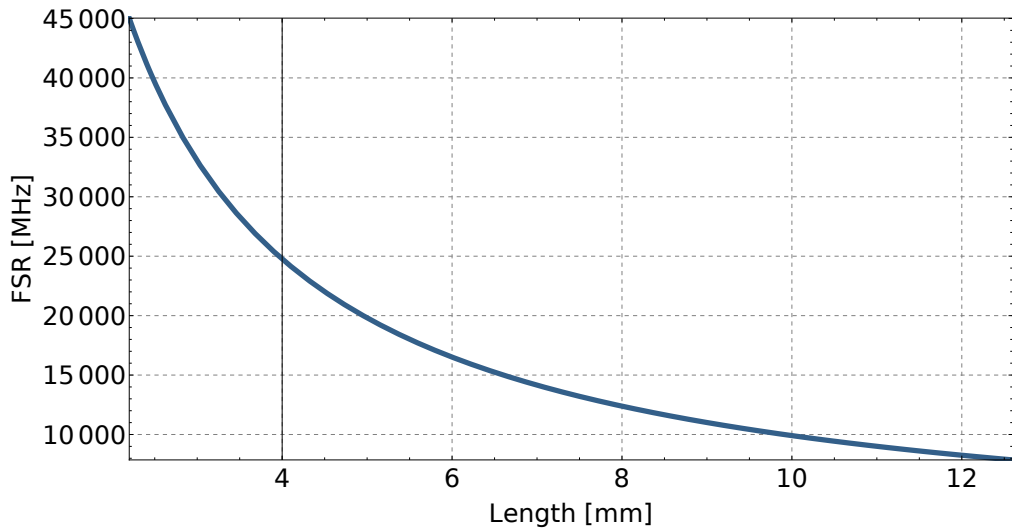


Figure 4.3.: Free Spectral Range over Thickness. The free spectral range was calculated for thicknesses between 2.2 mm and 12.6 mm. Equation 3.1 was used. The smaller thicknesses result in a higher FSR, which is appropriate for the experiments.

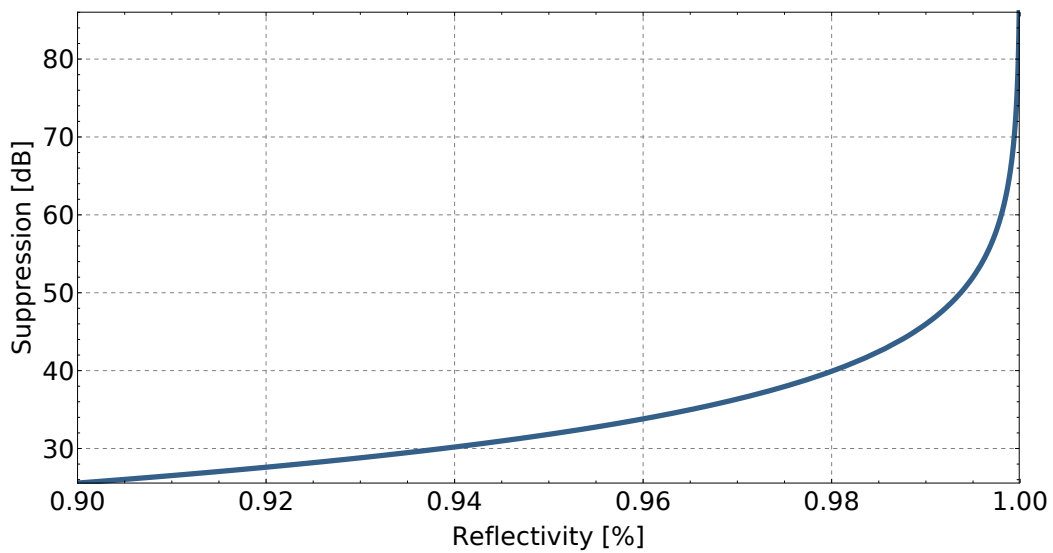


Figure 4.4.: Suppression over Reflectivity. The suppression was calculated with equation 3.17 for reflectivities between 90 % and 99 %. The steep curve towards the high reflectivities underlines the high sensitivity of the suppression against deviation in the applied reflectivities.

4.2. Characterisation of the Fabry-Pérot Filters

The following characterisations were conducted to measure the properties of the coated lenses and to characterise the filtering abilities. It be differentiated between the narrow filter, with a design goal of 100 MHz FWHM, and a broad filter, with a design goal of 500 MHz.

4.2.1. Setup

The general filter setup is presented in figure 4.5. The fibre coupler was used to flexibly collect light from a laser, an optical parametric oscillator (OPO) or quantum dots (QD) in the laboratory. The focus lens and the mirror pair were adjusted to optimise for maximum transmission in the TEM_{00} mode.

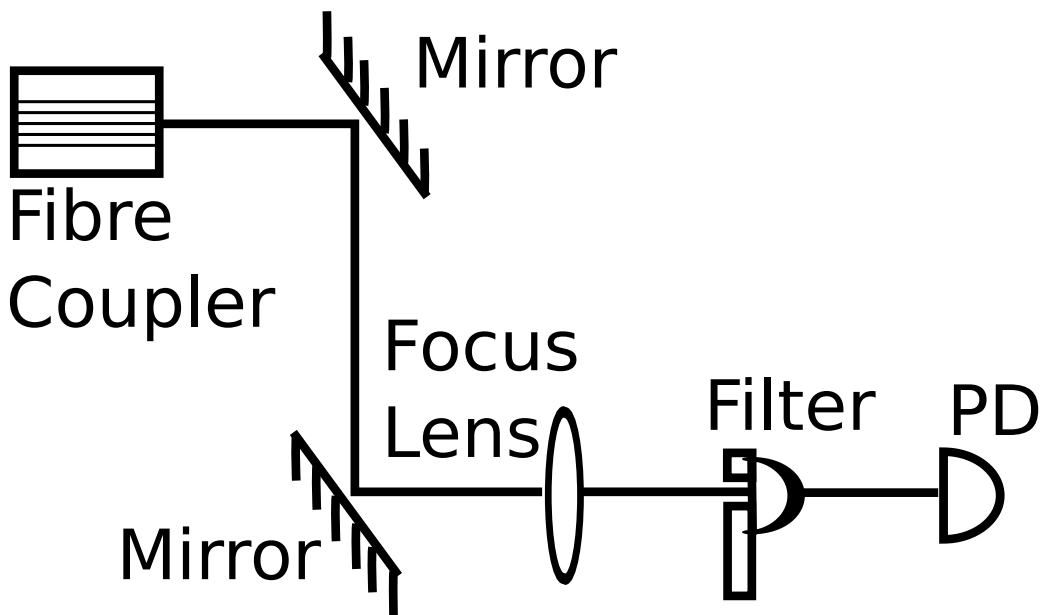


Figure 4.5.: Filter Setup. A beam out of a fibre coupler was coupled to the filters with a pair of mirror and a focus lens. Two mirrors were used to manipulate the angle towards the filter and the position on the filter. A photo diode measured the filter transmission.

4.2.2. Transmission and Line Width

A high transmission is an important property of a filter, as because it eases experiments with single photons. A very good single photon statistic is still favoured over a high output for the used sources. The transmission was measured by tuning the laser frequency to the central filter frequency for maximum transmission and detecting the throughput using a power meter. This resulted in 85 % to 90 % transmission for the broad filter and about 45 % for the narrow filter. The broad filter met the expectations, but the narrow filter transmission was lower than anticipated. The narrow filter might suffer from absorption.

The linewidth is the most important property, as the filters were selected upon their linewidths to filter the sources, the OPO and the QD. Figure 4.8 outlines the setup of the FWHM measurement. The laser was used in frequency scanning mode, which means that the central emission frequency of the laser was repeatedly shifted by some 10 GHz. An oscilloscope was used to acquire the data and a caesium vapour cell was used to scale the result. The scaling with the caesium worked with four distinct and known absorption lines, as presented in figure 4.9, in the caesium vapour, around the so called D1-line of 894.59 nm. As mentioned above, the FWHM is

$$\Delta v = \frac{(1 - R)c}{2\pi\mu d\sqrt{R}} . \quad (4.3)$$

The thicknesses were taken out of the vendor specifications and the reflectivities are one - transmissions. The transmissions were measured by the quality assurance of the

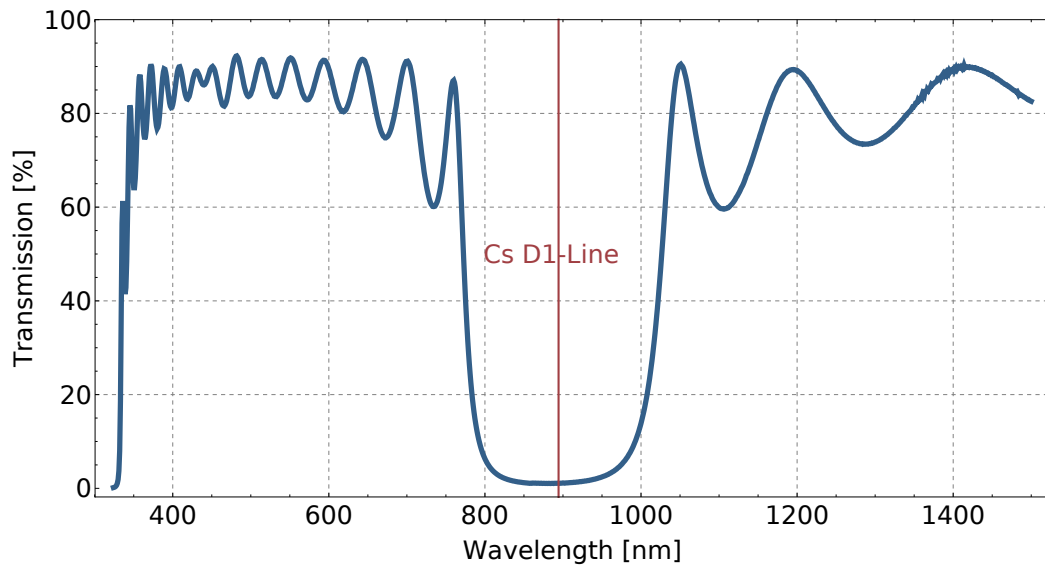


Figure 4.6.: Narrow Filter Transmission. The transmission of the narrow filter from the plan side was measured by the Beschichtungslabor TU Berlin. The transmission at the caesium D1-line equals a reflectivity of 98.89 %.

Beschichtungslabor TU Berlin, as shown in figure 4.6 and 4.7. The calculated ideal FWHMs were anticipated as 135.74 MHz for the narrow filter and as 698.2 MHz for the broad filter. The measured FWHMs, as shown in figure 4.10, were slightly higher as 192.81 ± 0.81 MHz for the narrow filter and as 883.7 ± 2.5 MHz for the broad filter. As the transmission of the narrow filter was quite low, it is reasonable to assume additional losses in the filter by absorption, thus broadening the linewidth. It might be counter intuitive, but the Fabry-Pérots are interference filters and absorption limits the number of round trips until the beam is damped. Less round trips mean less parts of the beam interfere at the output. This leads to less constructive interference for the central filter frequency and less destructive interference for off-central filter frequencies. The narrow filter has a higher reflectivity, therefore more round trips in the cavity, a greater optical path length and is finally greater impacted by absorption. Calculating the FWHM with only 99.95 % of the reflectivities as measured by the Beschichtungslabor results in 196.69 MHz for the narrow filter and 742.25 MHz for the broad filter. This brings at least the narrow filter measurements in accordance with the anticipated values. It should be notified, that the reflectivity measurement is always very challenging and reflectivity offsets have a high impact on the FWHM. The remaining error might result from absorption and scattering of dirt or scratches on the filters. Commercially available narrow-band filters, for example a fibre Bragg grating filter from Advanced Optical Solutions, have a minimum FWHM of 500 MHz, which is 2.5 times larger. In principle, the limits of this technique have not been reached by far, since reflectivity coatings exceeding $R=99.9\%$ are easy to manufacture, thereby allowing filter bandwidths below of 100 MHz.

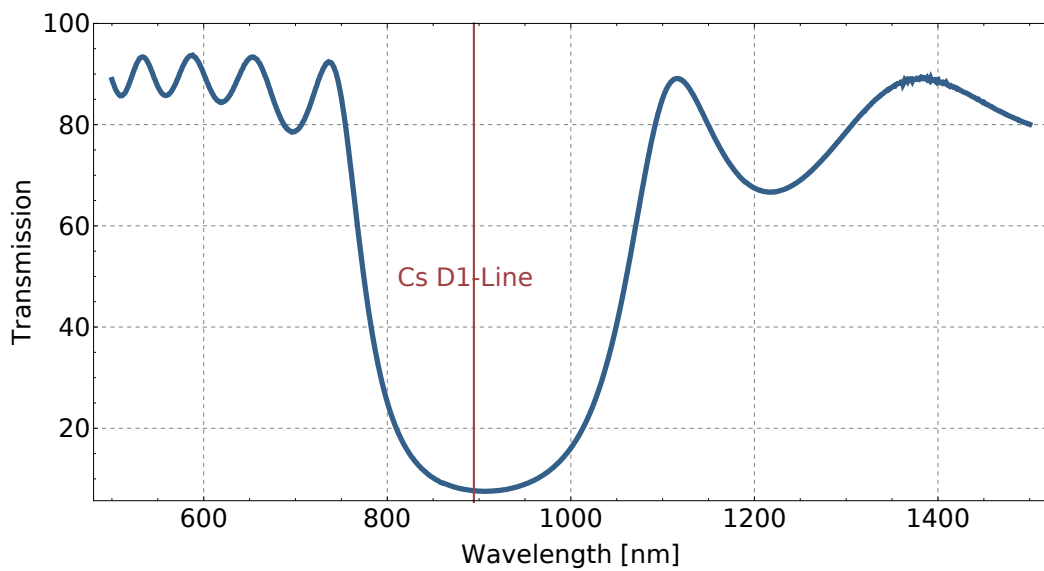


Figure 4.7.: Broad Filter Transmission. The quality assurance of the Beschichtungslabor measured the transmission of the broad filter. With 92.36 % reflectivity at the caesium D1-line the reflectivity is lower than that of the narrow filter.

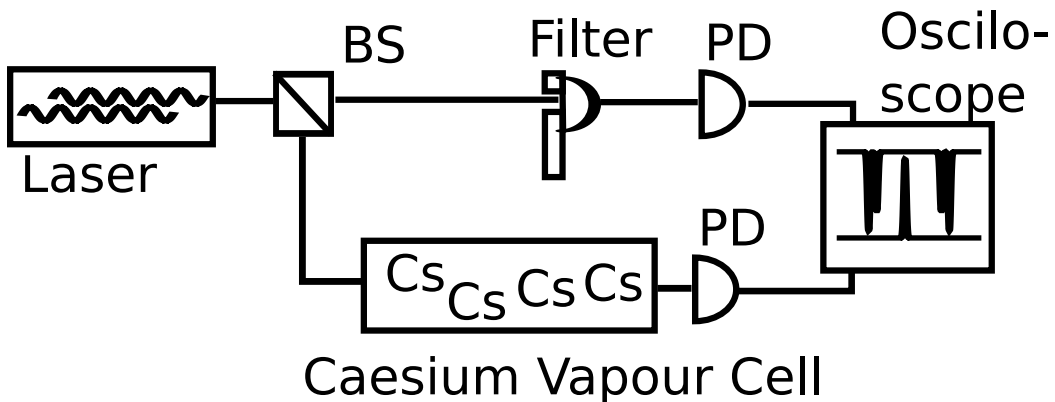


Figure 4.8.: Line Width Setup. A frequency scanning laser output with a scanning range of about 25 GHz was split into two beams. Part of it was send through the filter for FWHM measurement, and the other part was send through a caesium vapour cell to gauge the caesium absorption.

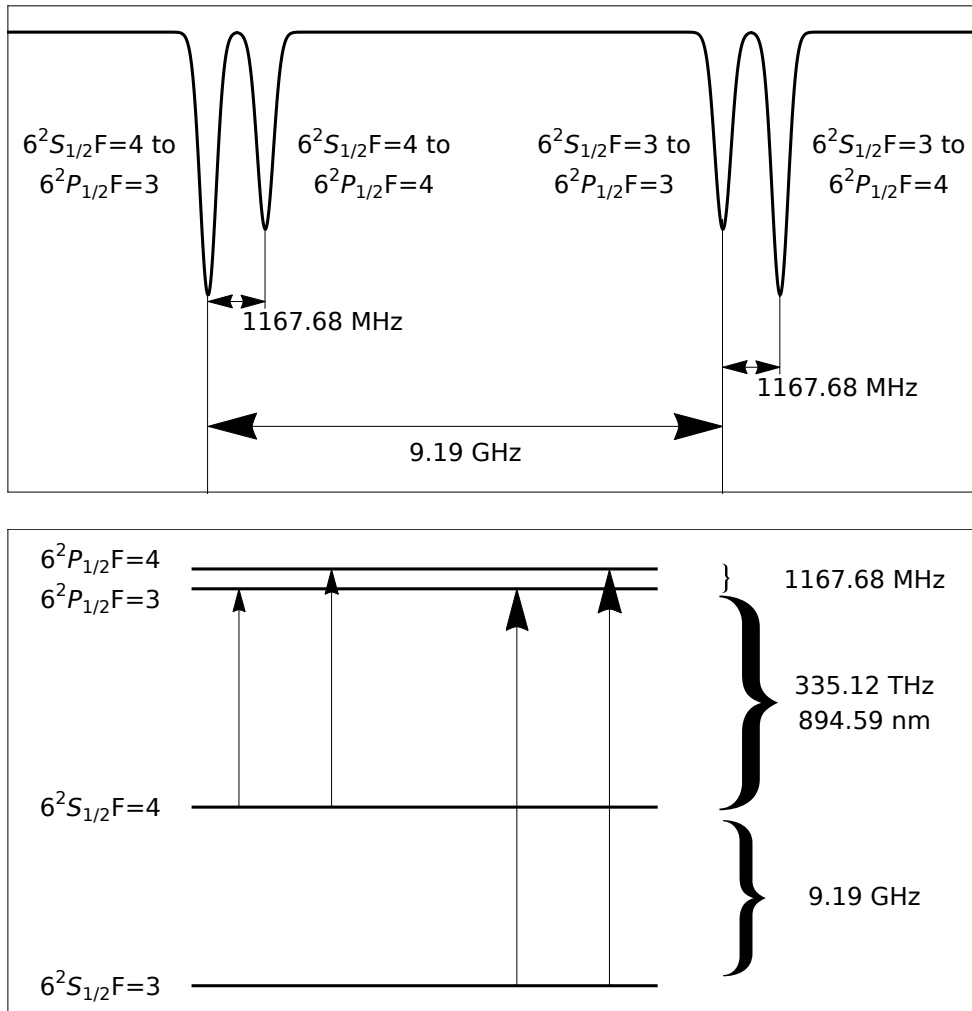


Figure 4.9: Caesium Absorption near D1-Line. The caesium absorption lines near 894.59295986(11) nm were used to scale the results. The difference between each pair on a side is 1167.680(78) MHz, and between the big peak on the left to small peak on the right is exactly 9.192 631770 GHz[65].

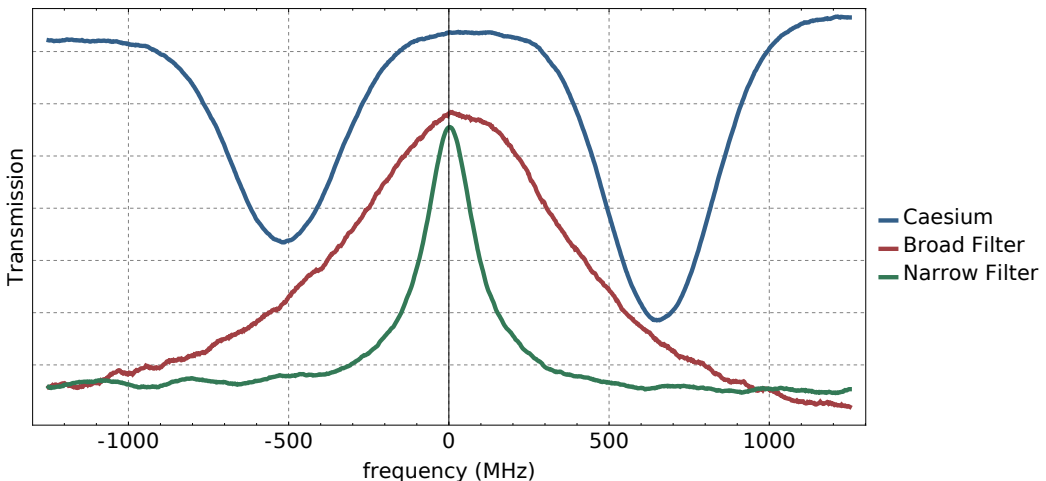


Figure 4.10.: Line Width Filter Scan. To determine the FWHMs a frequency scan with a laser was measured. The two caesium dips were used to scale the frequencies of the FWHMs.

4.2.3. Free Spectral Range

The free spectral range (FSR) of a Fabry-Perot filter defines the distance between successive transmitted peaks. It is an important consideration in a filtering setup, since the FSR needs to be larger than the bandwidth of the signal that is to be filtered. For the FSR determination a photo diode behind the filter detected a laser frequency scan. As figure 4.11 shows the electro-optical modulator was an important element of the measurement. The electro-optical modulator (EOM) was placed between the scanning laser and the filter. This EOM could phase modulate the laser signal with a frequency of up to 20 GHz. This transfers the original signal amplitude

$$A \exp(i\omega t) \quad (4.4)$$

into

$$A \exp(i\omega t + i\beta \sin(f_{EOM}t)) , \quad (4.5)$$

which adds sidebands with $\omega + f_{EOM}$ and $\omega - f_{EOM}$ to the signal. A and β are here amplitudes, while ω and f_{EOM} are frequencies. Higher order sidebands are negligible, since their amplitude was much lower. As the amplitude β is small, the frequency modulation did not change the signal before the filters. Neither does it change the signal after the filters, except in the case, when the laser frequency is $\pm f_{EOM}$ off the resonant frequency. The original signal then is suppressed by the filter, while the sidebands pass the filter. There are sideband peaks, relative to the zeroth order of the filter, at frequencies $\pm nFSR \pm f_{EOM}$, with n being the number of the order. As the FSR is the distance in the frequency domain between two neighbouring filter peaks, f_{EOM} equals half FSR, when a $-f_{EOM}$ side band of one order and a $+f_{EOM}$ side band of a neighbouring order overlap. The exact matching overlap is hard to fit, because two slightly overlapping Lorentzians are indistinguishable from a broader lorentzian

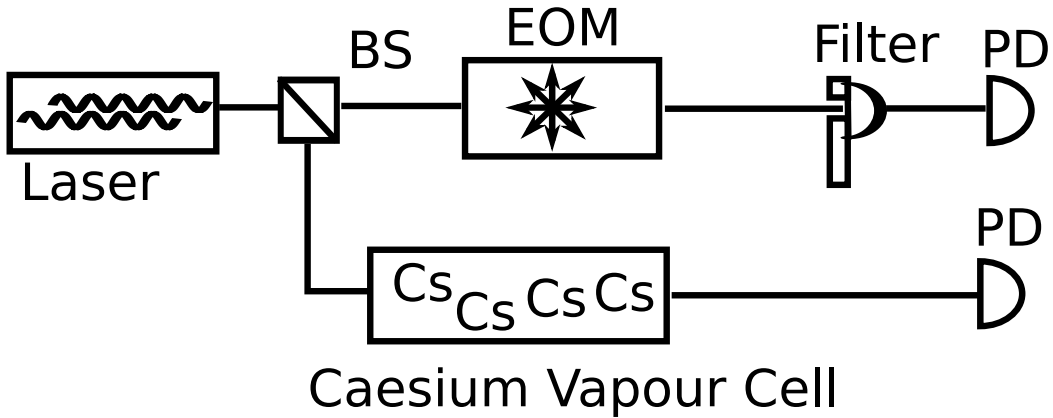


Figure 4.11.: *Free Spectral Range Setup.* For the determination of the free spectral range (FSR), a laser beam in frequency scanning mode was manipulated by a electrical optical manipulator (EOM), then sent through the filter and detected by a photo diode (PD). The distance between the peaks was scaled with the caesium absorption peaks out of the Cs vapour.

therefore, the gradual overlapping of the sideband peaks is measured successively with varying f_{EOM} .

The figures 4.12 and 4.13 show the measurement data. The FSR for the narrow filter can be determined to 37.79 ± 0.02 GHz and for the broad one of 28.83 ± 0.02 GHz. According to the thickness as specified by the vendor, the calculated FSRs $\Delta v = \frac{c}{2\mu d}$ are 38 ± 3 GHz for the narrow filter and 28.0 ± 1.5 GHz for the broad filter. The measurement confirms the predicted FSR, as it is in the range of the error. Compared with the QD signal broadness of 100 GHz, the FSR is wide enough. The complete OPO spectrum, on the other hand, is 100 GHz broad, therefore a cascaded filter system is required to suppress unwanted modes. Furthermore, a cascaded filter system suppresses further noise contributions from the QDs, that have a background of a few tens of GHz in width.

The FSR of the cascaded filters was calculated to about 500 GHz, which is very broad compared with the OPO and QD spectra. The FSR was too wide to be measured. It might be an interesting experiment for the future to measure this directly. With a different, more complex, setup, the accuracy could be improved, according to the literature[21, 50].

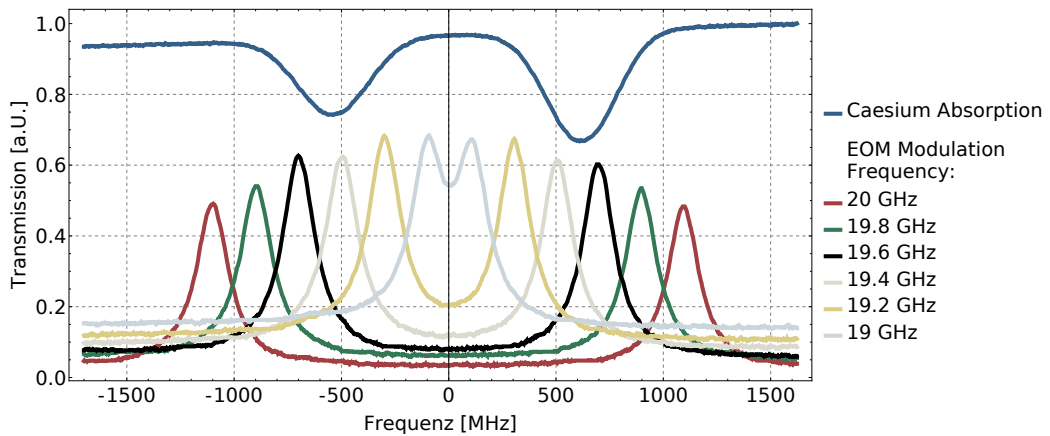


Figure 4.12.: Measured Free Spectral Range for the Narrow Filter. The measurement ignores the main peaks and focusses instead on the side band peaks. The side band peaks get closer with EOM frequencies nearer to $\frac{FSR}{2}$, until they meet and then depart in different directions. The frequencies around the peak overlap are not plotted, as they are useless for analysis. Only quarter of the narrow filter FSR measurements, namely every second with a $f_{EOM} > \frac{FSR}{2}$, are shown here to keep the plot neat. The measured FSR is 37.79 ± 0.02 GHz.

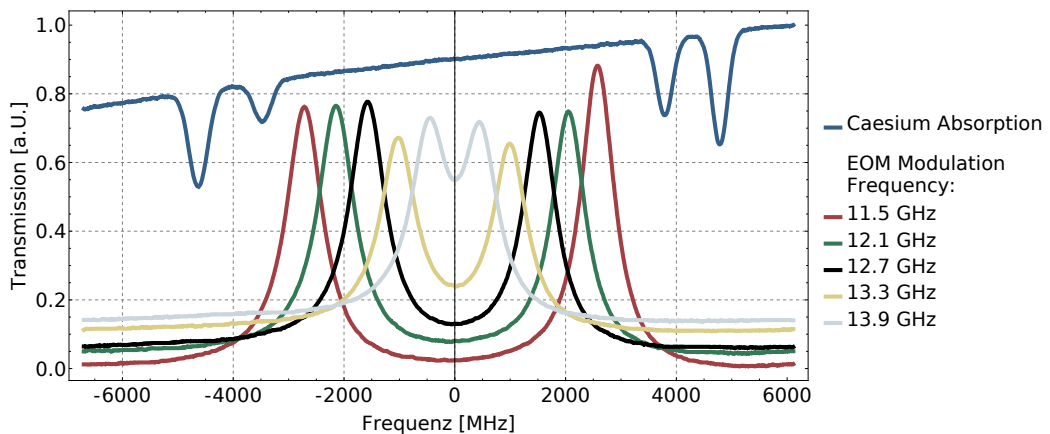


Figure 4.13.: Measured Free Spectral Range of the Broad Filter. Here are represented the EOM frequencies with $f_{EOM} < \frac{FSR}{2}$ for the broad filter. Like before, here are represented only a part of the measurements to keep the plot neat. The measured FSR is 28.83 ± 0.02 GHz.

4.2.4. Finesse

The finesse $\mathcal{F} = \pi \frac{\sqrt{R}}{(1-R)} = \frac{\text{FSR}}{\text{FWHM}}$ can be calculated through the reflectivities or through the measured FSR and FWHM. As shown in the discussion of the FWHM error, the inclusion of the absorption is necessary. The finesse calculated with the Beschichtungslabor reflectivities and the absorption results in 194.23 for the narrow filter and 37.17 for the broad filter. Using the measured results the finesse as 195.99 ± 2.64 for the narrow filter and 32.62 ± 0.12 for the broad. The finesse of the broad filter is slightly less than expected, which can be attributed to larger round trip losses or resulting from errors in the reflectivity measurement, dust or scratches on the filter.

4.2.5. Birefringence

Material with known high birefringence like calcite had been marked as unsuitable for interference filters, which should filter more than one polarisation at the same time. High birefringence could lead to resonant conditions that are only available to certain wavelength-polarisation combinations. But the filter should have a broad range of applications and should not be limited to some wavelength-polarisation combinations. Stress-induced birefringence can also be caused by pressure in amorphous materials. Using the setup as presented in figure 4.14, the birefringence was measured by filtering light at 45° , and splitting up the transmitted signal of the scanning laser into horizontal and vertical polarizations using a polarizing beam splitter, and detecting the signals on two photo diodes simultaneously.. The measured difference is 2 MHz and it is within the measurement error. Palittapongarnpim, MacRae, and Lvovsky [51] found for their filter a difference of about 181 MHz. As their filter is also made from BK7, it can only be speculated, why it showed such significant birefringence. It may be caused by the standard lens mount they are using. Carefully mounting the filters with even pressure on the face of the lens, as opposed to a stress-inducing side-screw, any such birefringence effects were suppressed. The mount was designed to withhold such strain and the design, judged by the birefringence in order of the measurement error, was a success.

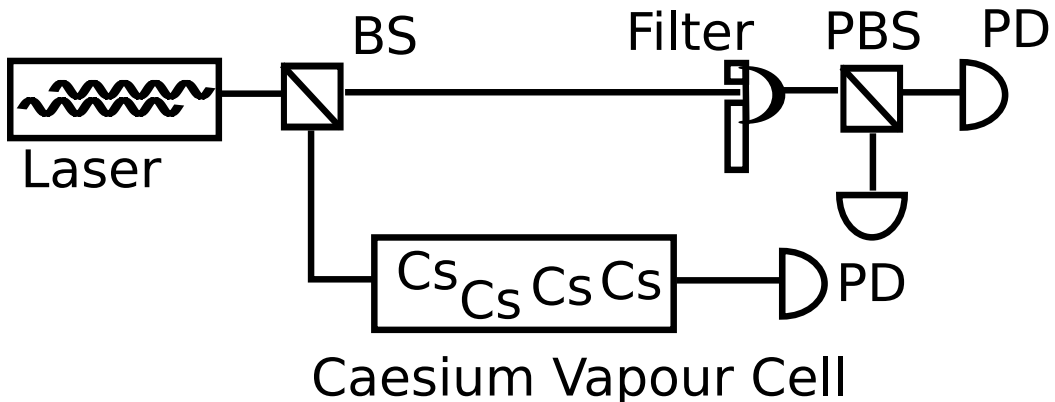


Figure 4.14.: Birefringence Setup. The birefringence setup used a PBS to send different polarized photons to different photo diodes. The caesium vapour was used to scale the differences between the transmissions of each polarisation.

4.3. Temperature Tuning

The previously described experiments could be conducted without stabilizing the filter, for the tuning of the filters a temperature controlling is necessary. The following section describes experiments that included temperature stabilisation and variation.

4.3.1. Setup

For achieving a flexible fine tuning of the central filter frequency the optical path length had to be changed. It was decided for temperature tuning with a Peltier element. Peltiers are compact, stable and easy to control, although they need a heat sink, which was the optical table in this case. For connecting the heat sink and the filter a aluminium spacer was designed. The first design can be seen in figure 4.15. Here the Peltier element was directly attached to the ground and the aluminium spacer connected to the filter. Although the temperature sensor of the Peltier was thermally glued into the lens holder, this feedback loop proofed to be slow.

As can be seen in figure 4.18 the delay was about two minutes for a temperature change of about $1.2\text{ }^{\circ}\text{C}$. A more reactive version, shown in figure 4.19, was designed and fabricated. As the major change the Peltier element directly connected to the filter. This reduced the delay for a temperature change of about $1\text{ }^{\circ}\text{C}$ to about 30 seconds. The first design was used in a portable sealed box, called filterbox, to minimize temperature fluctuations and air currents, which going to be described later on in chapter 5.3. This filterbox was very well thermal isolated and very compact, which made the mechanical tuning challenging.

As a consequence, a new setup, as can be seen in figure 4.20, with the second heater design was set up. The thermal isolations was done here with a PVC box. Some test showed, that this did not harm the filter performance. As the setup was more spacious and directly on an optical table, the important mechanical tuning elements were easily accessible, which facilitated adjustment and coupling of the incoming beam. For modularity the fibre coupling was kept.

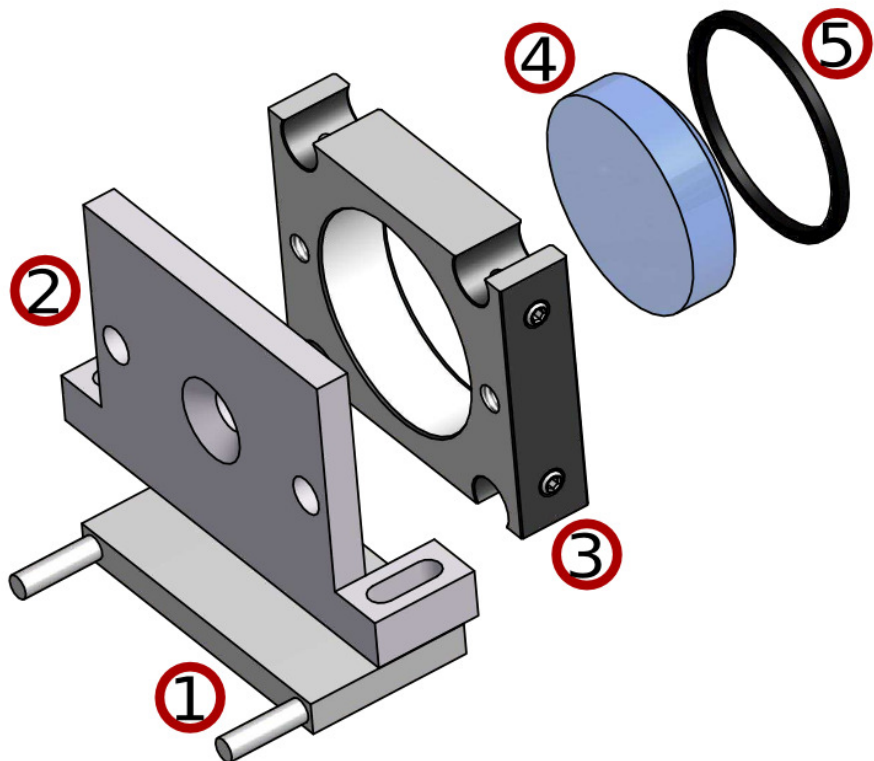


Figure 4.15.: Filterbox Heater. The filterbox heater is designed to use the filterbox ground as a heat sink. On top of the Peltier element (1), an aluminium spacer (2) connects to the lens holder (3) and (5). The temperature sensor for the temperature controller is integrated into the lens holder. The fixture pressure to keep the lens (4) at its place is spread gently over the whole lens. All parts except the aluminium spacer, which is custom made, are commercial available.

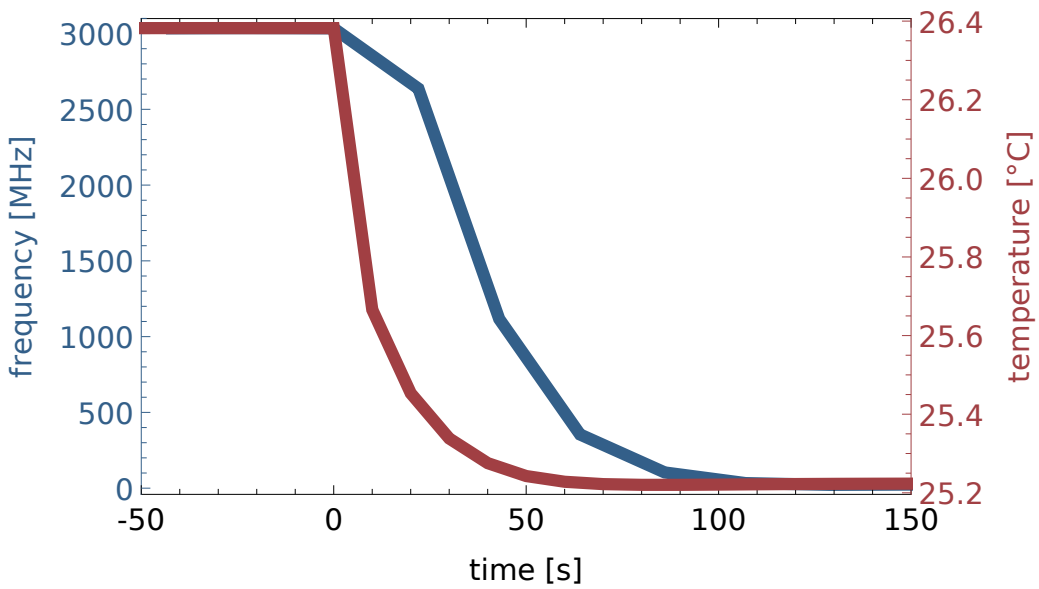


Figure 4.16.: The Reactivity of the Old Heater.

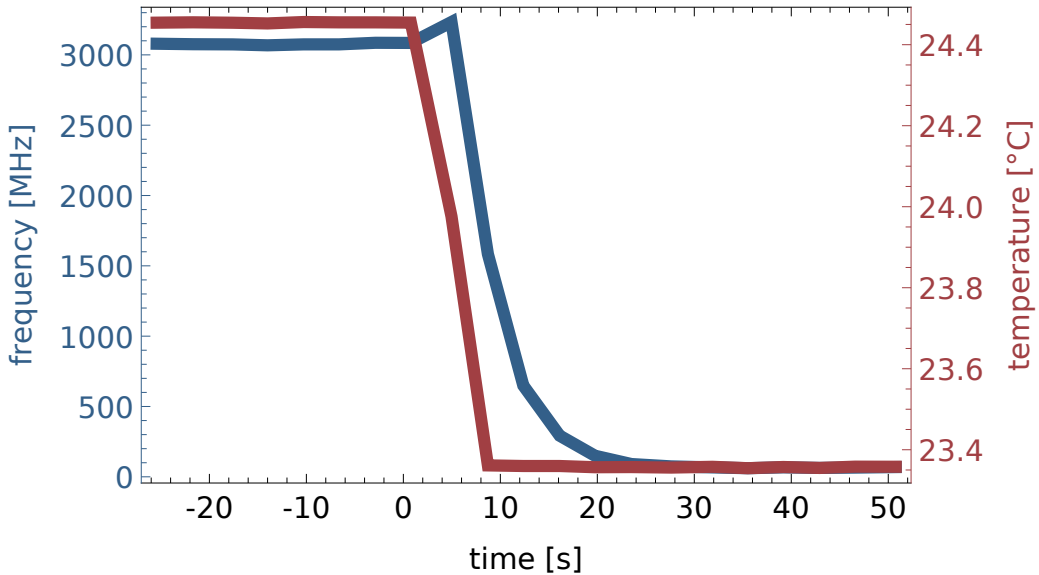


Figure 4.17.: The Reactivity of the new Heater.

Figure 4.18.: Heater Reactivity. The first design shows a delay of about 120 s for a temperature change of 1.2 °C in figure 4.16. In figure 4.17 a temperature delay of 1 °C was recorded for the second design, here the delay is 30 s. This meets the expectation, as the Peltier element in the second design is directly connected to the filter, while in the first design the Peltier connects to the filter over an aluminium spacer.

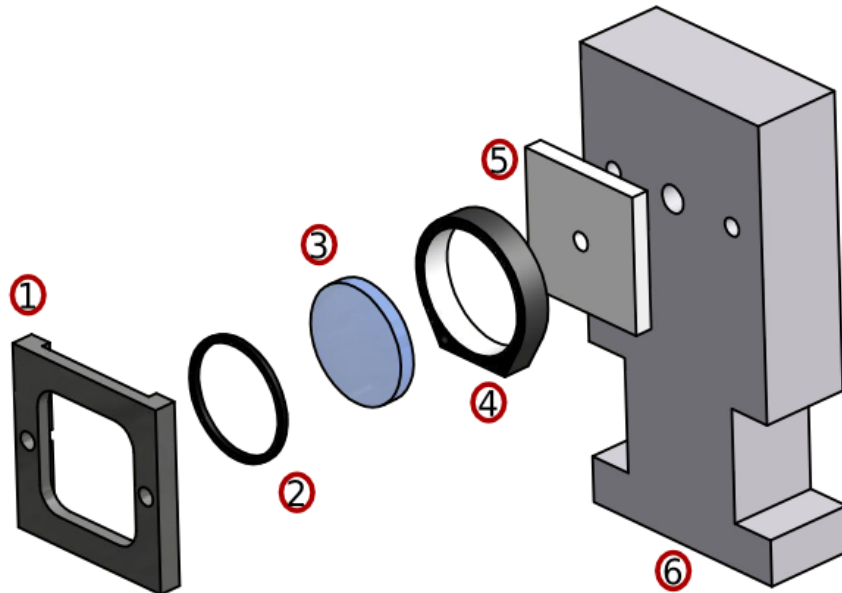


Figure 4.19.: Free Space Filter Heater. The latest advancement of the filter element couples the Peltier element (5) directly to the lens (3), while the heat sink and the Peltier are coupled via a custom made aluminium spacer (6). This Peltier element has a hole in the middle, to pass the beam. The lens holder (4) is a milled out of a commercial available one. The temperature sensor is implemented here. The parts (1) and (2) keep the lens gently in place.

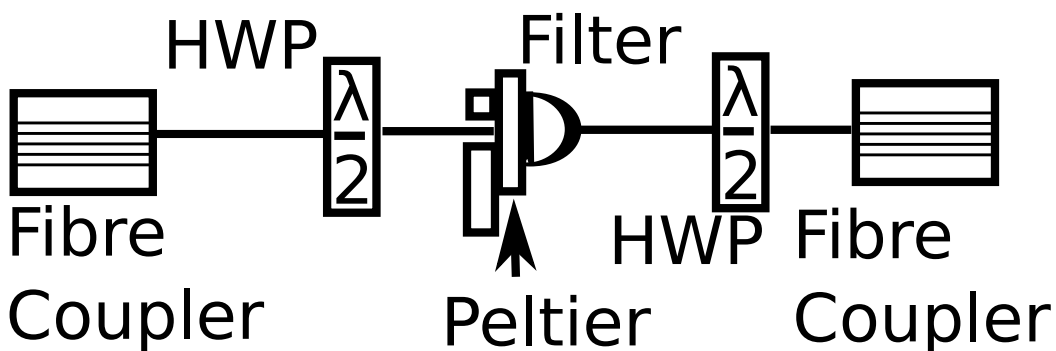


Figure 4.20.: Free Space Filter Schematic. The light out of the fibre coupler is coupled over an half wave plate (HWP) into the filter. The Peltier element is here directly attached to the filter. Before the outgoing fibre coupler the photons pass through a HWP.

4.3.2. Stability

The narrow and broad filter are tunable and the central filter frequency can be selected in a range of about 100 GHz. For single-photon experiments with entanglement swapping the selected frequency is very important. As the focus here is to do benchmark experiments with single photons instead of developing high count single photon sources, there is a demand for long term stability. Having the count rates in mind, the long term stability should be on the orders of hours. Would the optical path length change, the central filter frequency would drift as plotted in figure 4.21. Would the filter drift an order of FWHM, it would level the signal. It is also a question of reliability that the frequency drift is low.

Measurements of the absolute central filter frequency were conducted, after stabilizing the Peltier element, shown in figure 4.15, on the order of mK. The setup in figure 4.22 included a caesium vapour cell. Absorption lines in the caesium vapour cell were used to simultaneously record an absolute reference for the transmission peak through the filter. A photo diode detected the intensity of the laser frequency scan. The transmission through the filter and the caesium cell were recorded simultaneously as a tunable laser was filter scanned over the transmission peak and absorption line respectively. Such a measurement was recorded every 20 seconds for 24 hours. The results can be seen in figure 4.23 with a maximum offset of 10.15 MHz for the narrow filter and in figure 4.24 with a maximum offset of 15.4 MHz for the broad filter. Compared with the respective FWHMs, the drift is quite low and they are even in the same direction, which reduce the impact when the filter are cascaded.

Palittapongarnpim, MacRae, and Lvovsky [51] had a filter with 80 MHz FWHM and it had maximum offset of about 15 MHz in 25 min. So both results are comparable, while the here measured results have a slightly lower relative drift offset. The remaining amplitude of the selected central filter frequency after the 20 hours drift is 95.75 % for the narrow filter and 99.51 % for the broad filter. They measured for their filter[51] a root mean square (RMS) of 0.095 FWHM for data taken over 2 hours.

Here after the first two hours the narrow filter has a RMS of 0.0046 FWHM and the broad filter a RMS of 0.0044 FWHM. The results are about twenty times more stable than that by the other group. For the total measurement time the narrow filter's RMS is 0.024 FWHM with 0.0011 FWHM per hour and for the broad filter it is 0.0083 FWHM with 0.00039 FWHM per hour. That means, relative to the FWHM, the filters drifted in 20 hours less than their filter[51] in 2 hours.

It should be notified that the fit of the center filter frequency includes an error, which is not stable. This contributes to a pseudo-instability. With a perfect fitting of the peaks, the stability would be even better. An improvement of the temperature controller might be worth considering, if the need arises. The stabilisation of the filters were a significant success.

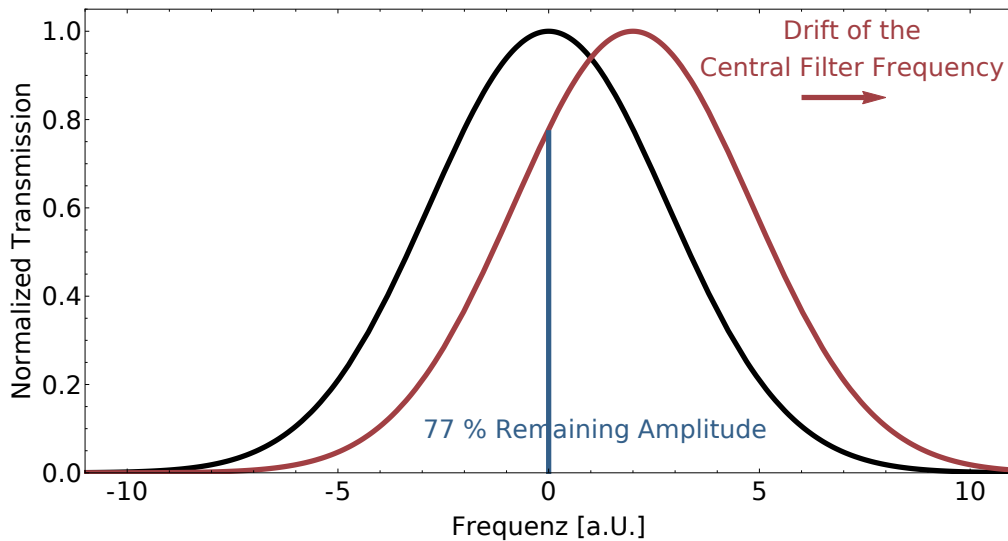


Figure 4.21.: Drift of the Central Filter Frequency. When the central filter frequency drifts, the amplitude of the previous transmission will be lowered. To have a constant amplitude for long term measurements, the stability is very important.

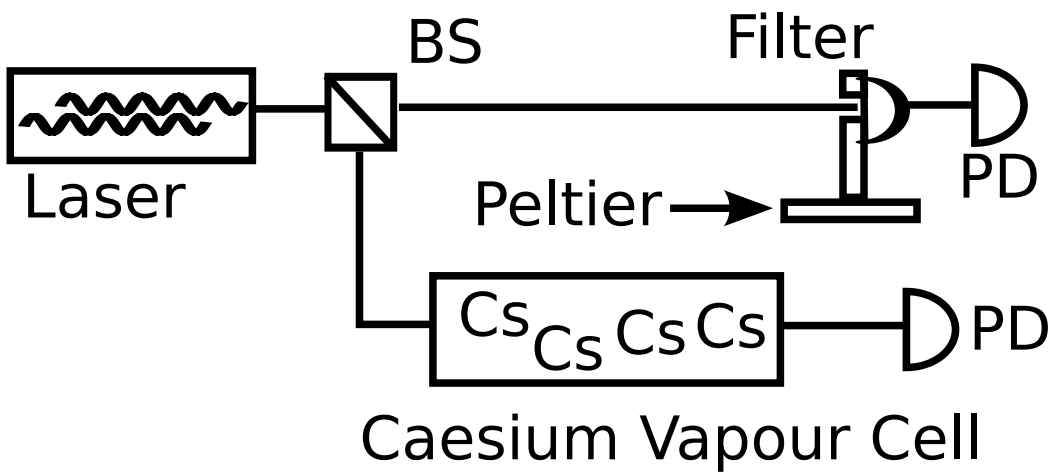


Figure 4.22.: Long Term Stability Setup. For the long term stability the scanning laser was send through the filter and measured by a photo diode (PD). Like before the absorption of the laser beam through a Cs vapour cell was used to scale.

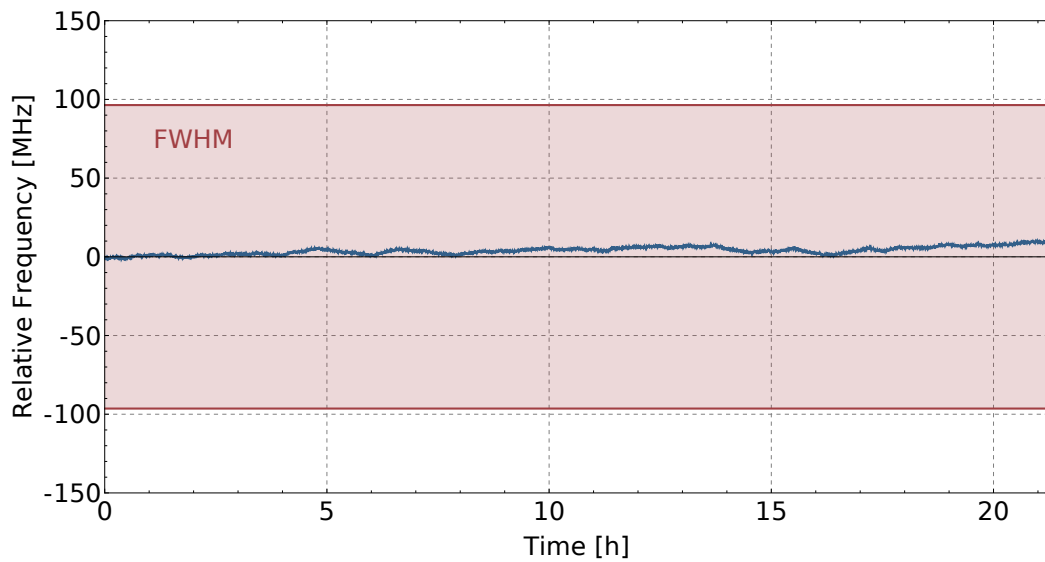


Figure 4.23.: Long Term Stability of the narrow Filter. The narrow filter drifts, relative to its central frequency, about 10 MHz in 20 hours. The red highlighted area is the width of the FWHM. The remaining amplitude of the central filter frequency after 20 h is at 95.75 %.

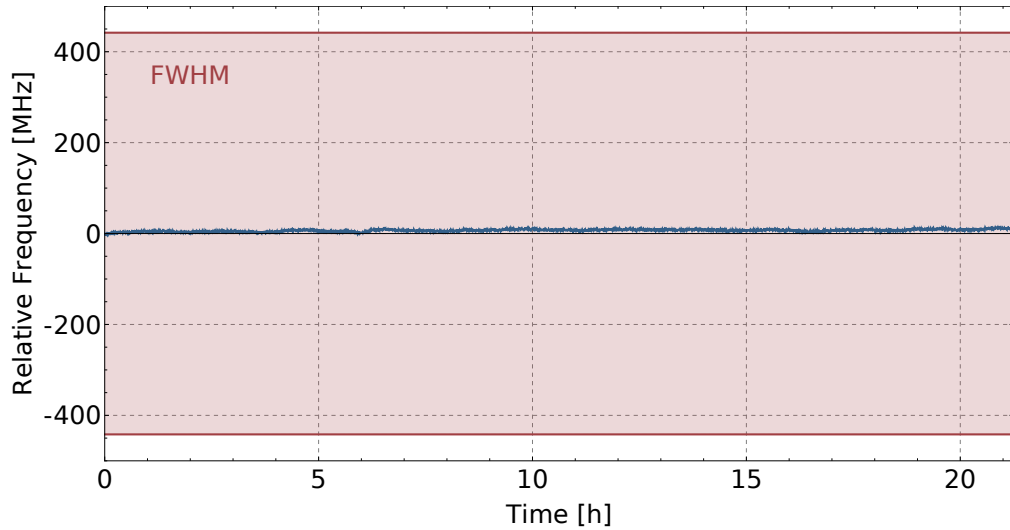


Figure 4.24.: Long Term Stability of the broad Filter. The broad filter drifts, relative to its central frequency, 15 MHz which comparable with the narrow filter. The red highlighted area is width of the FWHM. Due to wider line width, the percentage of the remaining amplitude is with 99.51 % higher than of the narrow filter.

4.3.3. Tunability

As mentioned before the selectivity of the central filter frequency is an important feature of the filter. In the last section the stability of the selected frequency was measured. Here will the stability of the selection itself be measured. To characterise the accuracy when temperature-tuning the filter over large gaps, 11 steps with a total width of 10 GHz were repeated over 80 hours. The filters were measured simultaneously. One filters started at its lowest frequency and the other at its highest frequency to add further stress to the system. The setup for this, can be seen in figure 4.25. The absolute frequency of the transmission peak was determined by simultaneously recording known absorption lines in caesium on another photo diode, as the laser frequency was scanned over both.

The results for the narrow filter can be seen in the figure 4.26. Over time, the same filter temperature did not lead back to the same central filter frequency. In absolute frequencies this meant an offset of about 110 MHz. This is very small compared with the total tuning width of 10 GHz. But the impact on the remaining amplitude of the selected filter frequency with an offset of 110 MHz is significant. With a FWHM of 192.81 ± 0.81 MHz for the narrow filter, the remaining amplitude after 80 hours is at 43.74 %. As plotted in figure 4.27 of an arbitrary selected frequency, 60 MHz to 70 MHz of this offset happens in the first third of the 80 hours measurement.

The behaviour of the broad filter is quite similar, as outlined in figure 4.28. Measurement has an offset of about 80 MHz, after more than 80 hours, as seen in figure 4.29. This is also very small compared with total tuning width of 10 GHz. The amplitude is less impacted, because the offset is small compared with FWHM of 883.7 ± 2.5 MHz for the broad filter. The amplitude still counts for 96.82 % of the original amplitude after 80 hours intensive measurement. Like the narrow filter, 60 MHz to 70 MHz of the offset are accumulated in the first third of the 80 hours measurement.

The offsets are similar and in the same direction, although one filter was tuned from higher frequencies to lower frequencies and the other filter from lower to lower. The temperature controllers seem to share an electrical problem. It might be worth improving the electrical devices, such as the temperature controllers, to obtain even better results.

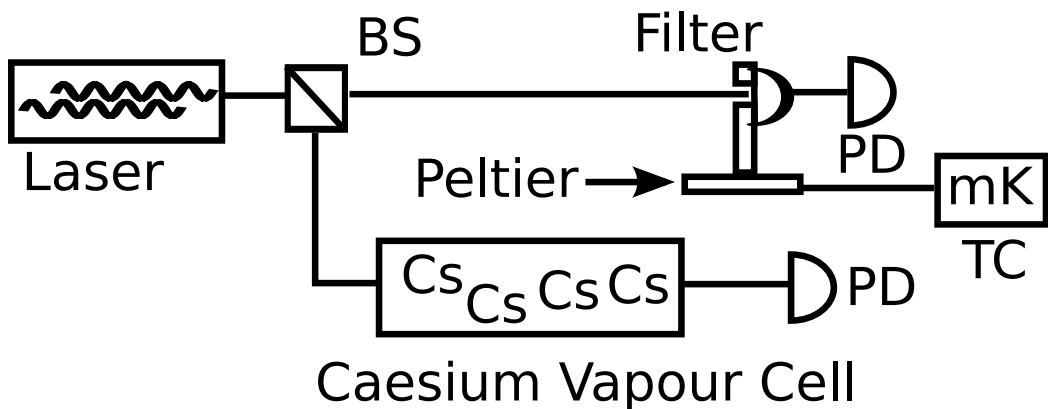


Figure 4.25.: Tunability Setup. The tunability of a filter was measured by detecting the intensity of a frequency scanning laser through the filter with a photo diode. The filter was tuned to different frequency by a temperature controller (TC) over hours. The intensity signal through a Cs vapour cell was used to scale the tunability results.

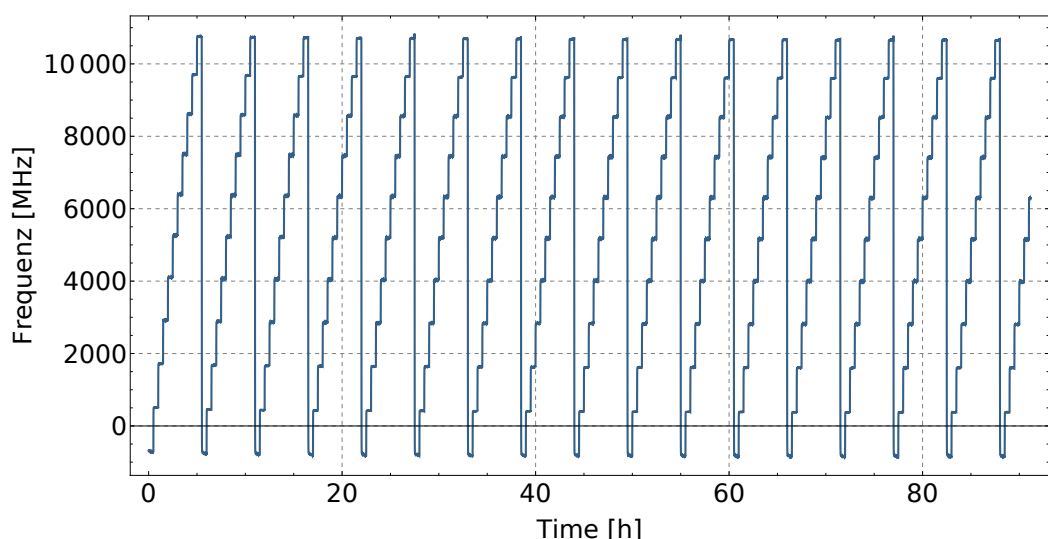


Figure 4.26.: Tunability of the Narrow Filter. The tunability of the narrow filter was measured for more than 80 h and shows, relative to the complete tuning bandwidth, a good retunability. To measure the system under stress, both filter were measured parallel in the same thermal isolation with contrary step directions.

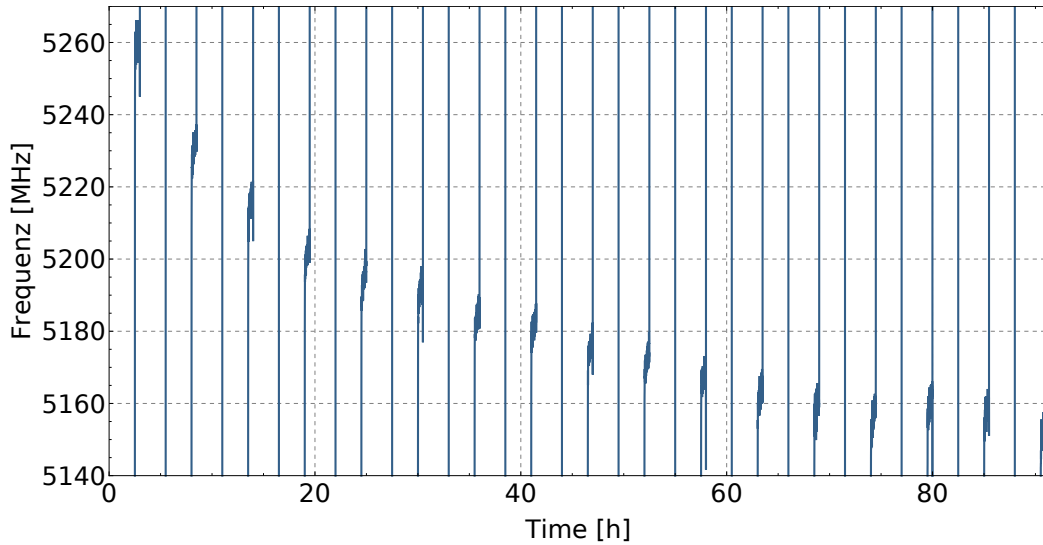


Figure 4.27.: Tunability Detail of the Narrow Filter. This is a detail of a single level of figure 4.26 and it shows, that the repeatability was off about 110 MHz after more than 80 hours of shifting the central filter frequency in a band width of about 10 GHz. The remaining amplitude was 43,74 % after 80 h. It should be notified, that typical single photon experiments do no need 80 h for completion. The first third of the measurement is mainly responsible for the total shift.

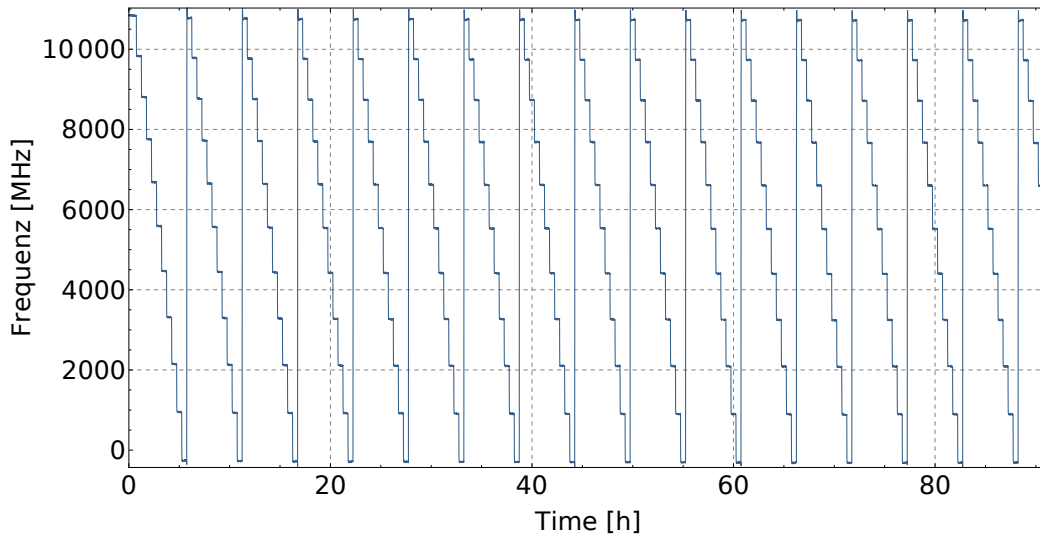


Figure 4.28.: Tunability of the Broad Filter. The tunability of the broad filter was also measured for more than 80 h and behaves very similar to the narrow filter.

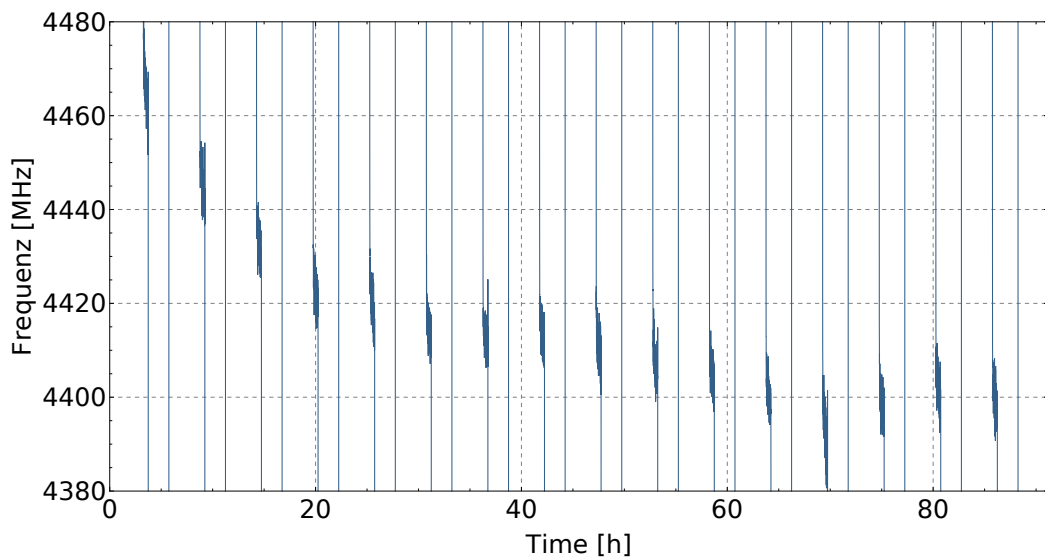


Figure 4.29.: Tunability Detail of the Broad Filter. The detail of figure 4.28 shows the degradation of the retunability as 80 MHz. Like the narrow filter, this filter's central frequency was shifted for more than 80 h in a band width of about 10 GHz. The 96.82 % amplitude after 80 h would be still enough for most experiments.

4.3.4. Suppression

To a filter it is important to suppress anything but the transmission peak to a high degree. Hence the level of suppression needs to be determined. The theoretical suppression of a Fabry-Perot resonator can be calculated as a function of the reflectivity of the end-mirrors using equation 3.17:

$$S[\text{dB}] = 10 \log_{10} \left[\frac{4R}{(1-R)^2} \right] \quad (4.6)$$

It calculates to 47 dB for the narrow filter and 31 dB for the broad filter. To measure the actual suppression the setup in figure 4.30 as used. By slowly varying the temperature of the filter using the Peltier element and scanning it over a fixed frequency laser, which was locked to a caesium absorption line, the transmission could be recorded. A lock-in amplifier was used to measure a wider dynamic range. The filters were measured separately though, as the dynamic range of the lock-in amplifier was too small for the cascaded filter system. The narrow filter suppresses with 40.2 dB and the broad one with 25.6 dB. The difference between the calculated values and the measured values can be explained by the inaccuracy of the transmission measurement, as presented in figures 4.6 and 4.7, or by degeneration of the reflectivity after measurement through dust and scratches.

By adding the suppressions of each filter, the suppression of the cascaded filter will be about 60 dB. Compared with the AOS fibre bragg grating suppression of 55 dB the separate filter are less suppressive but have a similar suppression when they are cascaded. A lock-in amplifier with a higher dynamic range would be necessary to measure the high suppression of the cascaded filters.

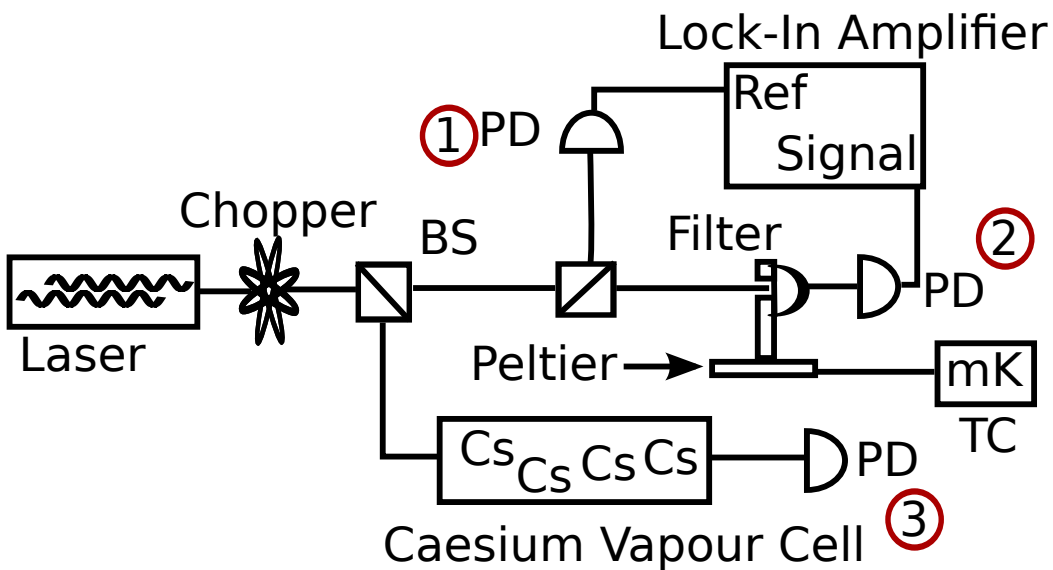


Figure 4.30.: Suppression Setup. The results were determined by sending a fixed frequency laser beam through a filter and obtaining the intensity with photodiode (PD) (2). A lock-in amplifier was used for a better signal-to-noise ratio (SNR), therefore the laser beam was chopped and the chopping frequency measured with PD (1). The caesium absorption was registered by photodiode (3) for scaling the results.

4.4. Monolithic Fabry-Pérot Filter Conclusion

The 192.81 MHz FWHM filter was stabilised up to 0.024 FWHM for more than 20 hours. In the same time period the 883.7 MHz FWHM filter was stabilised for 0.0083 FWHM. The high stability make the filters suitable for rigorous long lasting single photons experiments. The filters can be cascaded and then the FSR will be about 500 GHz with a suppression of 60 dB. This recommends them for filtering OPO or QD photons. The experiments determined the properties of the filter and their results show they are applicable for further experiments. Especially the stability measurement has surpassed the expectations.

The principle of the monolithic Fabry-Pérot filter has proven it worth. For applications beyond single photon optics, filter can be designed for a broad range of wavelengths, with a small FWHM, a high FSR and a high suppression. In tests the filters were tuned in a range of 50 GHz. This was limited by the power of the Peltier element. Filters, that shares these properties, often lack the flexibility or are not cost effective. The monolithic Fabry-Pérot filter can be designed very compact, which is important for integrated or space applications.

5. Filtering Optical Parametric Oscillator Photons

Filtering the output of an optical parametric oscillator (OPO) is an interesting test case for future filtering of dissimilar sources for indistinguishability. An experiment is set up to scan the spectrum of an OPO with a high frequency resolution. The OPO spectrum is calculated with a simplified model, to compare it with the result of the spectroscopy. Important parts of an OPO, such as the non-linear crystal or the cavity are investigated. Beside OPOs, the properties of quantum dots (QD) will be discussed. In the discussion, the focus will be on the frequencies, not the wavelength. Working towards indistinguishability in the order of some hundred MHz, a difference of about 1 pm, the frequency is more appropriate property to be discussed. As 894 nm equals 335 THz, the differences in terms of wavelengths are very small.

5.1. Quantum Dots

Semiconductors are defined by their band gap between valence and conducting band. Spatial confined semiconductor are widely-used for lasers and photon sources. Spatial confined semiconductor are quantum wells, quantum wires and quantum dots (QD). The different structures confined the electrons in one, two and three dimensions, as they shape a potential well and thereby the possible frequencies in the potential well. In a vacuum, the spatial limit to effect the potential well would be around 10 Å, but in the semiconductor the effective mass of the electron influences the frequencies significantly. The necessary spatial dimension becomes then roughly 100 Å, depending on the used materials. In conclusion, the size of the spatial dimension determine the emitting frequencies of the quantum structure.

Quantum dots are grown inter alias with molecular beam epitaxy or metallorganic vapor phase epitaxy. The confinement is then a result of an auto-organisation process, which minimizes the strain in the crystal. The intended strain is an outcome of an lattice mismatch between the used semiconductors. Quantum dots are simply to integrate in fibre or circuit boards and can be mass assembled in a production line of the semiconductor industry. They are built in different geometrical shapes, like microdisks, micropillars or microcavities[44]. For the least one the spontaneous emission rate in the cavity is enhanced by the Purcell factor[55, 70]

$$f = 3Q\lambda^3/4\pi^2V \quad (5.1)$$

with quality Q , cavity volume V and in medium wave length λ of the emission. By

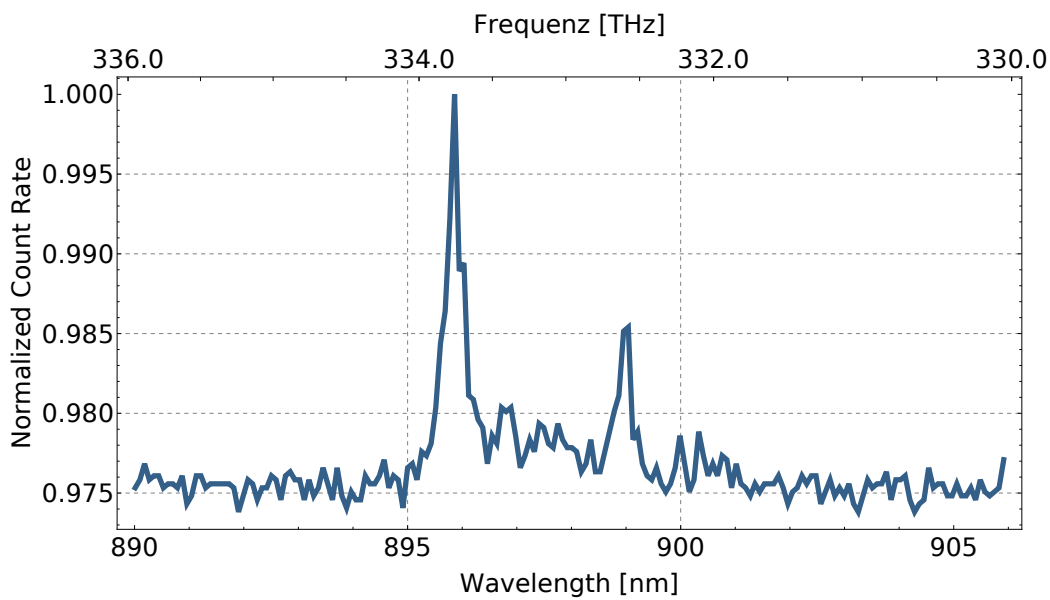


Figure 5.1.: Quantum Dot Spectrum. The emission of an example quantum dot is some nm wide. Near 896 nm the biggest peak can be seen. The spectrum had been measured in the work group by Kroh [38]. The samples were grown by the working group Dr. Armando Rastelli at the Institut für Integrative Nanowissenschaften of the Leibniz-Institut für Festkörper- und Werkstoffforschung Dresden and the working group Prof. Dr. Martin Kamp of the Julius-Maximilians-Universität Würzburg.

equation can be seen, that cavity volumes of nm order are necessary for an effective enhancement. For quantum dots as single photon sources $InGaAs/GaAs$ are ideal candidates as their quantum efficiency is near one. The quantum efficiency is important as low driven quantum dots ensure a good single photon statistic. An other material system for a single photon source is $GaAs/Al_xGa_{1-x}As$. An example of a QD frequency spectrum, that has been characterized by Kroh [38], can be seen in figure 5.1. The inherent bandwidth of such QDs is on the order of GHz. They were examined and had emission lines between 895 and 900 nm. After selecting an appropriately close QD, further fine-tuning can be done using temperature, a magnetic field, an electric potential with the Stark effect, or strain-tuning using a piezo.

5.2. Optical Parametric Oscillator

The optical parametric oscillator (OPO) can be used for a wide field of applications like spectroscopy[37], and for experiments in quantum optics. First of all the OPO is tunable, which are attenuated lasers also, but they are considered to be unsuitable for single-photon generation. An OPO far below threshold generates a single photon pair, of which one photon could be used for heralding without disturbing the other. It uses a second order nonlinear $\chi^{(2)}$ effect, namely spontaneous parametric down-conversion (SPDC), as seen in figure 5.2. The effect describes that a photon of higher frequency is converted into two photons of lower frequency or frequencies. The $\chi^{(2)}$ effect got its

name by the Taylor expansion of the dielectric polarisation density

$$P(t) = \epsilon_0 \left[\chi^{(1)} E(t) + \chi^{(2)} E^2(t) + \chi^{(3)} E^3(t) + \dots \right], \quad (5.2)$$

where $E(t)$ is an applied optical field and $\chi^{(n)}$ the n-th order tensor of susceptibility. The $\chi^{(1)}$ and other higher order uneven terms do not require certain materials, while the $\chi^{(2)}$ effect and the even higher orders require a crystal as a medium. Out of available crystals the second-order effect is only possible in crystals without inversion symmetry, because in centrosymmetric media the electric fields cancel each other out. As of the intensity of the effects the $\chi^{(1)}$ term is the linear term and about unity for condensed matter. According to Boyd [8] it is the product of the atomic number density and the non-resonant polarizability. The $\chi^{(2)}$ and the $\chi^{(3)}$ are in crystals of the order pm (10^{-12}) and ym (10^{-24}) respectively. Therefore an intense applied optical field, like intense laser light, is necessary to achieve any significant higher order signal.

A non-linear crystal with a fairly high second order non-linearity, transparency at the wavelengths of interest, and adequate phase-matching possibilities is potassium titanyl phosphate (KTP). The crystal was pumped with a beam of 447 nm, which was frequency doubled from a 894 nm laser using second harmonic generation in a bowtie cavity. Depending on the phase-matching conditions the SPDC process can result in photon pairs that are degenerate or non-degenerate. For the following experiments, the phase-matching was optimised for degenerate photons, which could be locked to the caesium D1 line. Type-II phase-matching was chosen, which results in orthogonally polarised photons, to facilitate separation of the two photons in one pair. Following energy conservation the photon pair frequencies are $\omega_{\text{pump}} = \omega_s + \omega_i$. Due to the dependence on the refractive index μ to the wavelength λ , there is a phase mismatch[60]

$$\Delta k = \frac{2\omega}{c} (\mu_{2\omega} - \mu_\omega) \quad (5.3)$$

in the crystal between the pump light and the converted light. The phase mismatch Δk then limits the efficient conversion. Having the properties of the sinc in mind a coherence length

$$l_c = \frac{\pi}{\Delta k} = \frac{\lambda}{4(\mu_{2\omega} - \mu_\omega)} \quad (5.4)$$

can be defined. At crystal length between l_c and $2l_c$ the harmonic power decreases due to reconversion into the fundamental wave, as Scholz [60] mentions. Typical coherence wavelengths are in the 100 μm regime. Normal phase matching by birefringence works by phase angle adoption. This approach does not work for co-linear photon pairs with orthogonal polarisation and a tunable wavelength. Therefore the potassium titanyl phosphate crystal (KTP) was periodic poled. Periodic poling induces quasi-phase matching of the beam in the crystal and leads to a higher conversion efficiency, as can be seen in figure 5.3. The period of the poling[60] with the n-th order can

derived from

$$\Lambda_m = \frac{2\pi}{\Delta k} (2m - 1) . \quad (5.5)$$

There are various period poling techniques[31] for reversing the crystal axis orientation. By periodically inverting the orientation the first derivation of the power function $\propto \text{sinc}^2$ switches its sign[8]. With a matching period it leads to the slight modulated curve of quasi-phase matching in figure 5.3. For stabilization and phase matching adjustment the periodically poled potassium titanyl phosphate (PPKTP) was temperature tuned by a Peltier element. According to Boyd [8] the spectral power density of the down-conversion has the relation

$$S_{Down}(\omega) \propto \text{sinc}^2 \left(\frac{\Delta k L}{2} \right) \quad (5.6)$$

with crystal length L . The calculated spectrum in figure 5.4 is the result of such a down-conversion process. As Scholz [60] notes the harmonic power output of a planar wave is then

$$P_{2\omega} \propto \text{sinc}^2 \left(\frac{\Delta k L}{2} \right) P_\omega^2 . \quad (5.7)$$

For the planned application this spectrum has a low spectral brilliance, count rate per MHz bandwidth, and therefore a low count rate.

As Ahlrichs et al. [1] published, the non-linear crystal was put into a cavity to shape the spectrum. Figure 5.5 shows the principle of the setup. This setup is often called optical parametric oscillator (OPO). As mentioned previously cavities have a frequency selection function, because they amplify frequency resonant in itself and dampen the other. The OPO was pumped far below the conversion threshold to assure that only one photon pair with single photon characteristic at a time is generated. The enhancement factor

$$B = \frac{\mathcal{F}^3}{2\mathcal{F}_0} \quad (5.8)$$

for a parametric down-conversion source in a cavity far below threshold has been found by Ou and Lu [48]. \mathcal{F} is the finesse of the cavity, \mathcal{F}_0 is the finesse of the cavity without loss, and B describes the enhancement of the signal rate by the cavity. The cavity, which consisted out of two high reflective mirrors, was stabilized with a piezo feedback loop, which allowed locking to the D1 line. Due to the optical path length mismatch of orthogonally polarized photons resulting from the inherent birefringence of the conversion crystal, a further KTP crystal rotated at 90° was inserted into the cavity. The workgroup Herzog, Scholz, and Benson [25] developed a theory for a signal-resonant optical parametric oscillator and later on Scholz [60] derived an equation for the spectral power density. Here a less sophisticated model will be used, as it is appropriate for the applied case. The down-conversion spectrum of equation

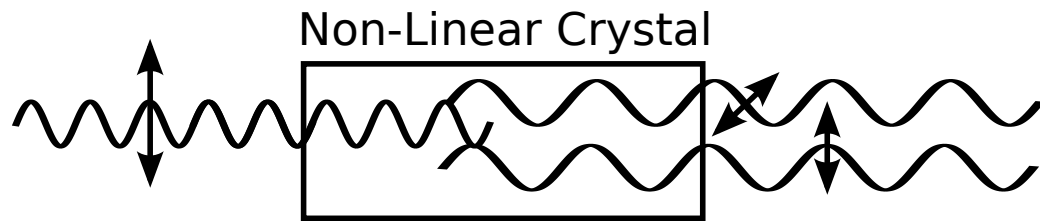


Figure 5.2.: *Down-Conversion.* The principle of Down-Conversion can be seen here. A pump laser photon enters the crystal from the left and towards the right side two photons leave. Due to energy and impulse conservation the pump laser photon energy and impulse must at least match the sum of the energy respective the impulse of the two photons. In this case are used a type II process and the output photons are orthogonal polarized.

5.6 is then modulated by the Airy-function, equation 3.4, to a spectral power density of

$$S_{OPO}(\omega) \propto \text{sinc}^2\left(\frac{\Delta k L}{2}\right) * \left[1 + \frac{4}{\pi^2} \text{Finesse}^2 \sin^2 \frac{\pi}{\text{FSR}}\right]^{-1}. \quad (5.9)$$

The calculated OPO spectrum around 894 nm can be seen in figure 5.6. There are about 40 comb lines within the spectrum spaced 1.9 GHz apart, each with a width of 100 MHz as defined with the cavity finesse. The count rate is more than 100 kilocounts per second of detected photon pairs at approximately 10 mW.

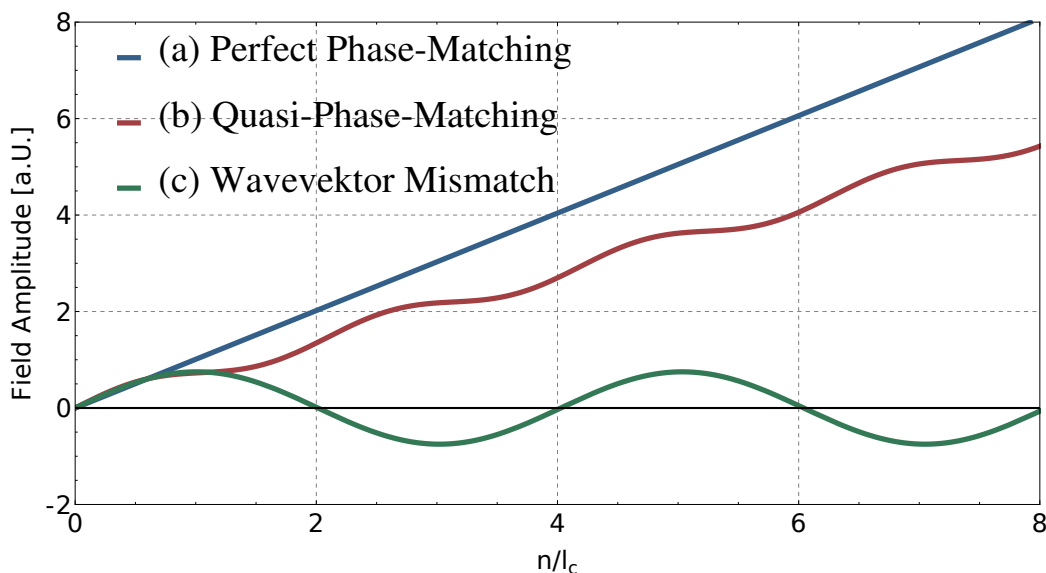


Figure 5.3.: Quasi Phase Matching. Here the development of the field amplitude over units of coherence length can be seen. Curve a) show the ideal perfect phase-matching, curve b) the quasi-phase-matching and c) the wavevector mismatch case. When phase matching cannot be implemented, quasi phase matching is an approximation to it and generates a significant higher amplitude than down-conversion with a wave vector mismatch for crystal length larger than the coherence length.

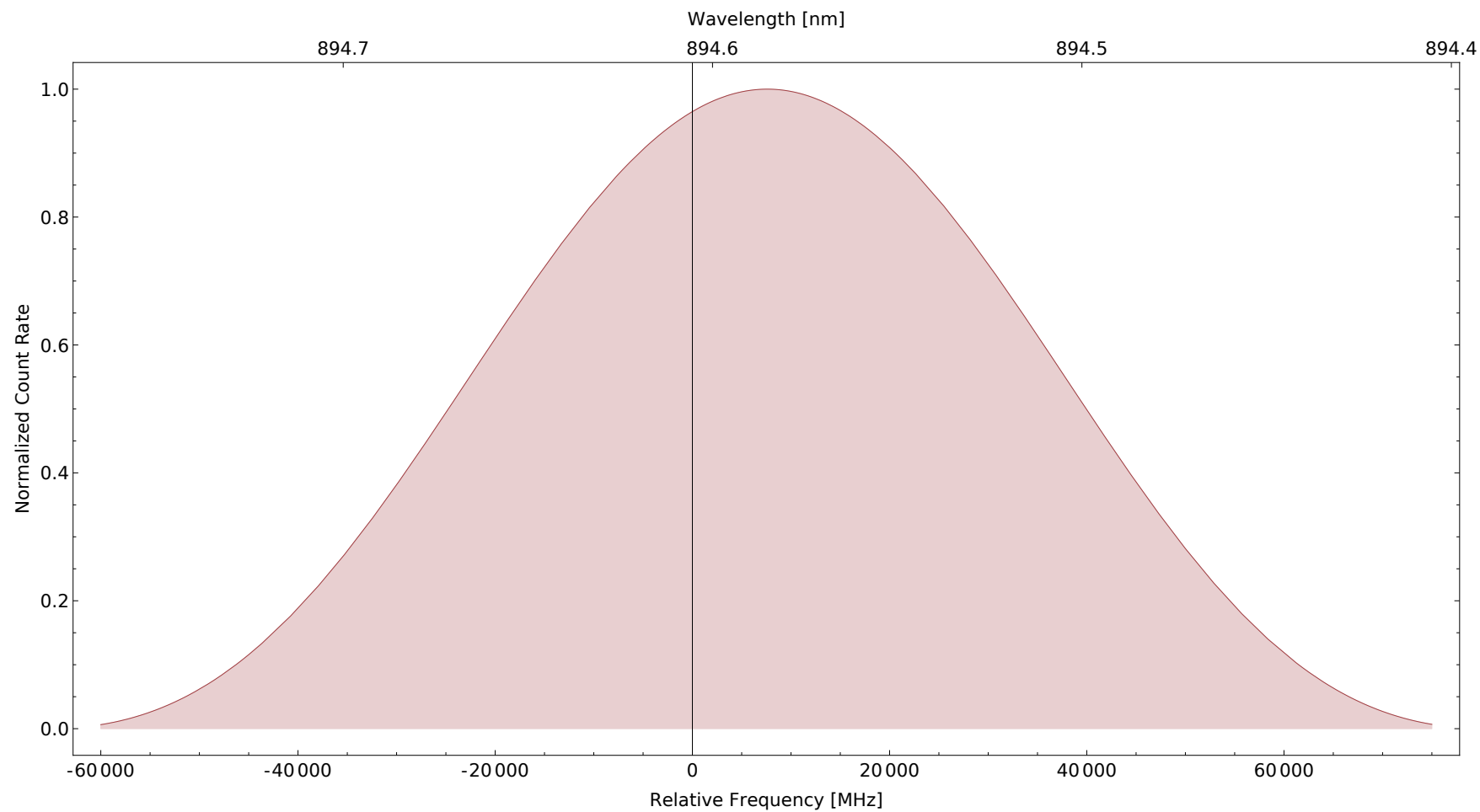


Figure 5.4.: Calculated Down-Conversion Spectrum. This spectrum is emitted by a non-linear crystal without a cavity, when a laser beam is focused into it. The process is called spontaneous parametric down-conversion.

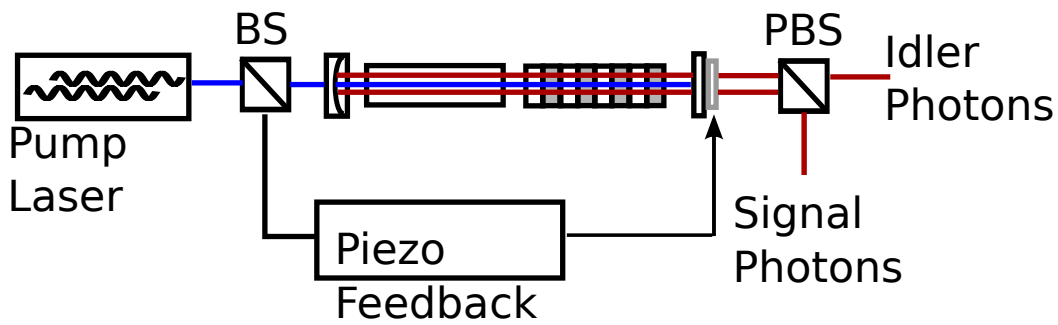


Figure 5.5: Optical Parametric Oscillator Principal. For the generation of an orthogonal polarised photon pair, two crystals are enclosed in a cavity of high reflective mirrors. A periodic polarised potassium titanyl phosphate (PPKTP) for the conversion process, and a compensation crystal, which is rotated 90° relative to the PPKTP, to adjust the optical path length for both polarisations. The cavity is pumped by a laser, which emits at a wavelength of 447 nm. A part of the pump laser beam is send into a piezo feedback, which stabilises the cavity. Behind the OPO a PBS splits signal and idler photons, which are then coupled into fibres.

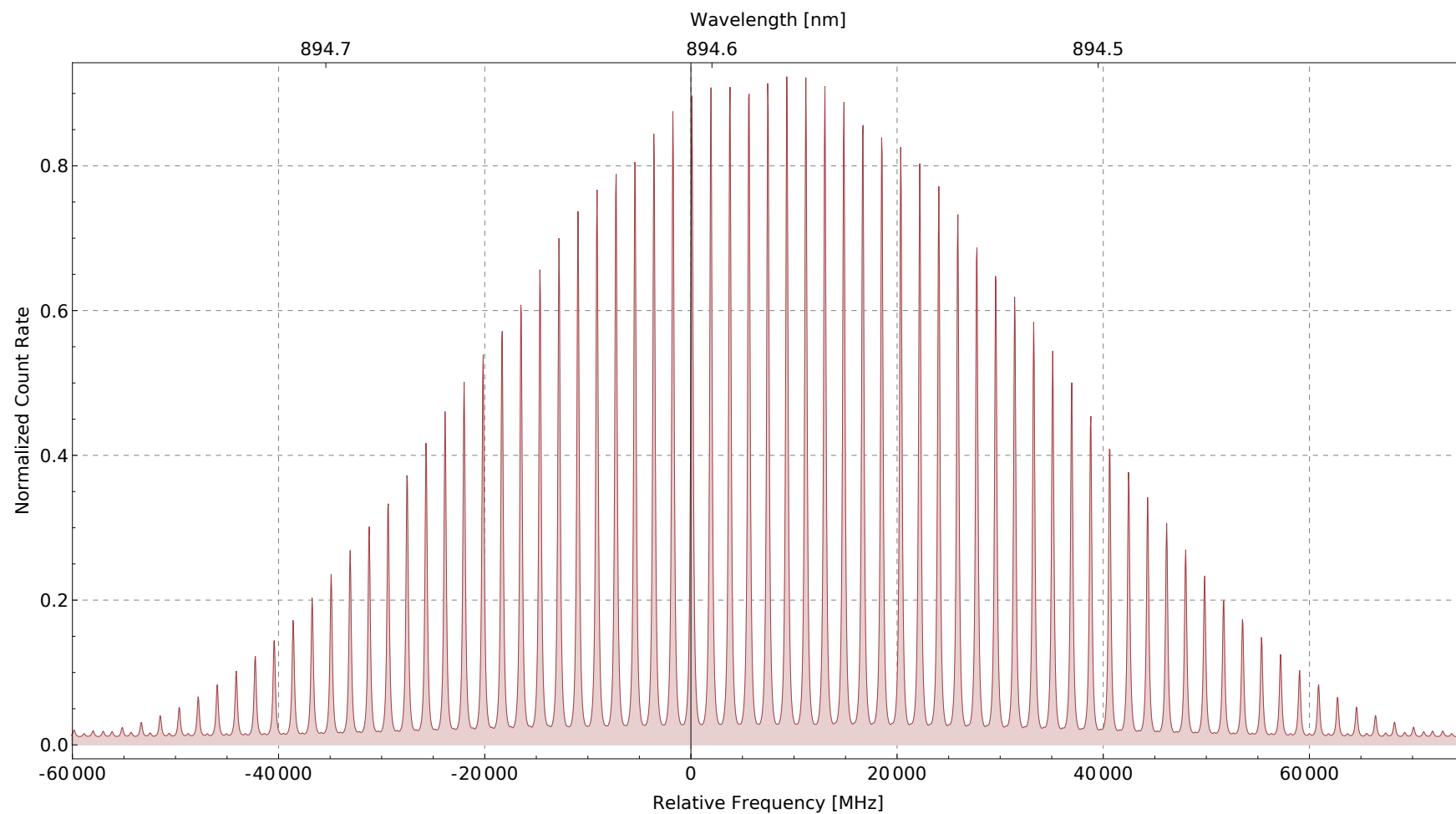


Figure 5.6.: Calculated OPO Spectrum. When the parametric down-conversion of figure 5.4 is fostered which a cavity, this spectrum results. In a simplified model the down-conversion spectrum is modulated by an Airy-Function. The used equation is 5.9.

5.3. Optical Parametric Oscillator Experiment

Out of 40 comb lines of the OPO spectrum, the challenge is to filter a single comb line, which requires a narrowband filter, below the 1.8 GHz FSR of the OPO, and a very high FSR to suppress the other comb lines. To accomplish this filtering with a single monolithic fabry perot cavity, a lens thickness of around 250 μm would be required. Such a small thickness and a high curvature are contradicting for standard sized lenses. The high curvature is needed for a good beam stability. Instead a cascaded filter system was designed and set up with two filters. While maintaining the FWHM of the more narrow filter, the combined FSR is much larger, since the overall transmitted signal is the product of the separate transmission airy functions as can be seen in figure 5.7.

To tune the filters by temperature, the heat spreader was designed as seen in figure 5.8. Although Peltier elements stabilized the filters in preliminary tests, it was learned that they are sensitive to thermal perturbation. A compact and portable box was designed for thermal sealing from environmental effects. A schematic of the box is shown in figure 5.9, and a photograph of the box is shown in figure 5.10. Fibre coupled input and output ports made the box portable, and allowed various photon sources to be attached. The base plate of the box, which was used as a heat sink for the filter Peltier elements, was stabilised with an additional set of Peltiers. Precisely tunable compact mirror holders were used for the most critical elements - namely the mirrors before the filters for precise coupling.

For scanning the OPO spectrum, as seen in figure 5.11, the OPO photons were coupled into the fibre coupler on the top left in figure 5.9. Behind the two filters and the fibre coupler in the left middle a photo diode measured the intensity of the incoming light. The scan was done with slowly temperature tuning both filters in parallel for hours. The scan step size was 40 MHz and at each step the count rate was integrated for 1 s. The temperature tuning for each frequency shift lasted about 4 s. Beforehand, the filter tuning was calibrated to keep the two filters overlapping during the measurement. The result of the measurement will be discussed in the next section.

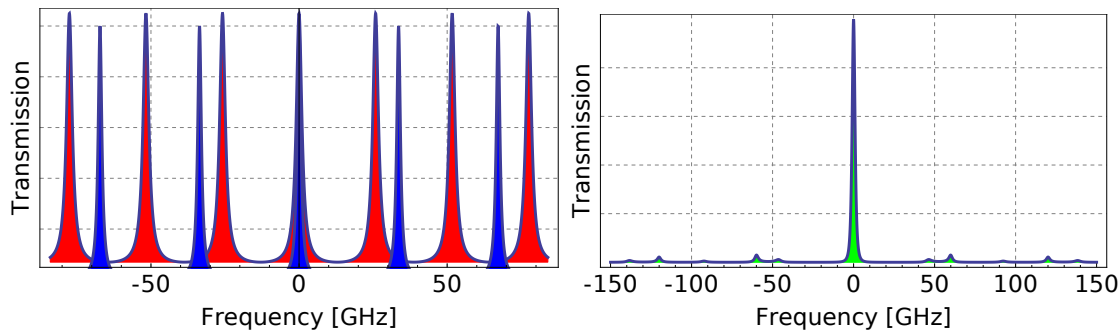


Figure 5.7.: Cascaded Filter Free Spectral Range. On the left hand side can be seen the transmission peaks of the separated filter, which are separated by the free spectral ranges (FSR). When both filter are cascaded the effective FSR is far wider than of the single filters. The cascaded system has a FSR of 500GHz.

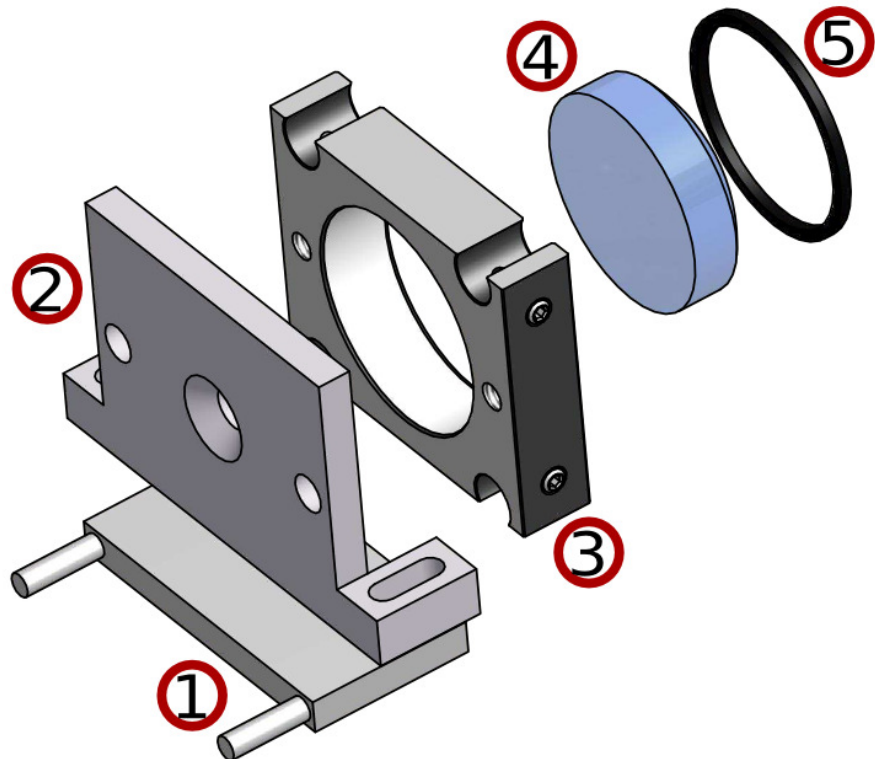


Figure 5.8.: Filterbox Heater. The filterbox heater was designed to use the filterbox ground as a heat. On top of the Peltier element (1), an aluminium spacer (2) connected to the lens holder (3) and (5). The fixture pressure to keep the lens (4) at its place was spread gently over the whole lens. All parts except the aluminium spacer, which was custom made, are commercial available.

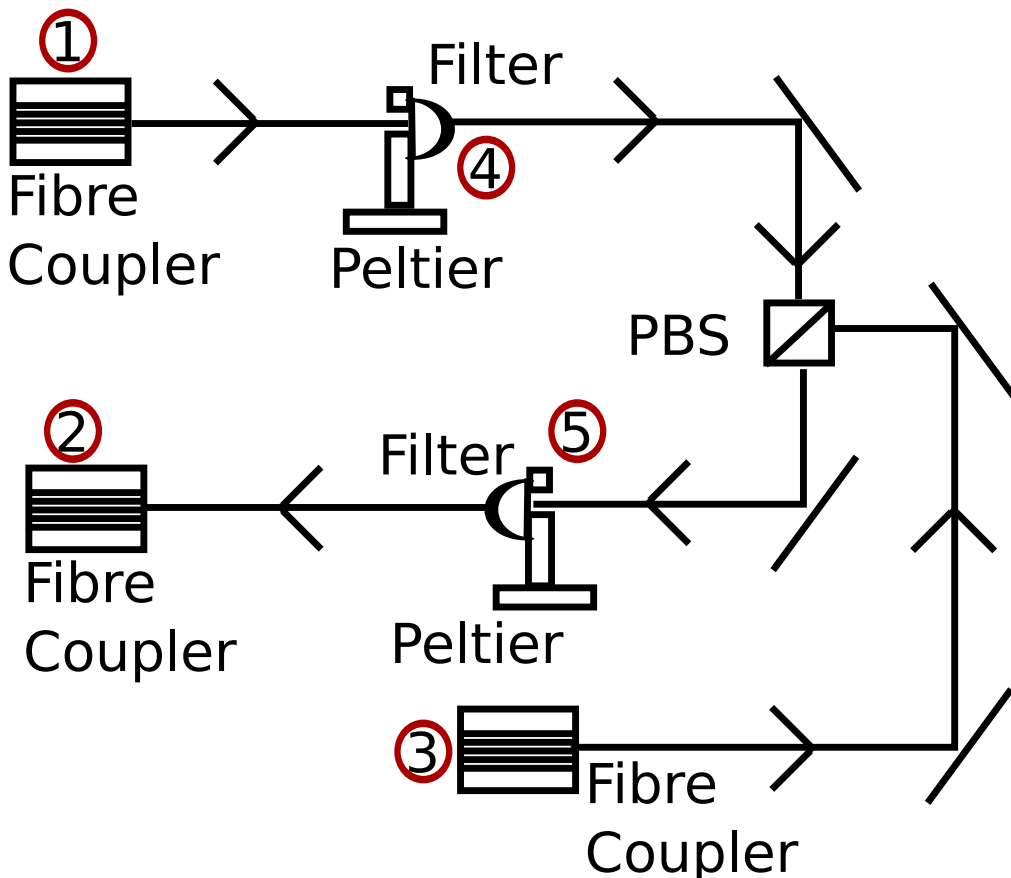


Figure 5.9.: Filterbox Schematic. This is the schematic of the filterbox, which shows the fibre couplers (FC), the filters (F), the mirrors (M) and the polarizing beam splitter (PBS). The Setup was designed to filter two beams in parallel. The beam coupled in at the FC ① will be filtered at the F ④, the narrow filter, and the F ⑤, the broad filter. The photons from the FC ③ will be filtered only with the broad filter ⑤. At the PBS both beams are brought to overlap. The combined output fibre coupler is ②.

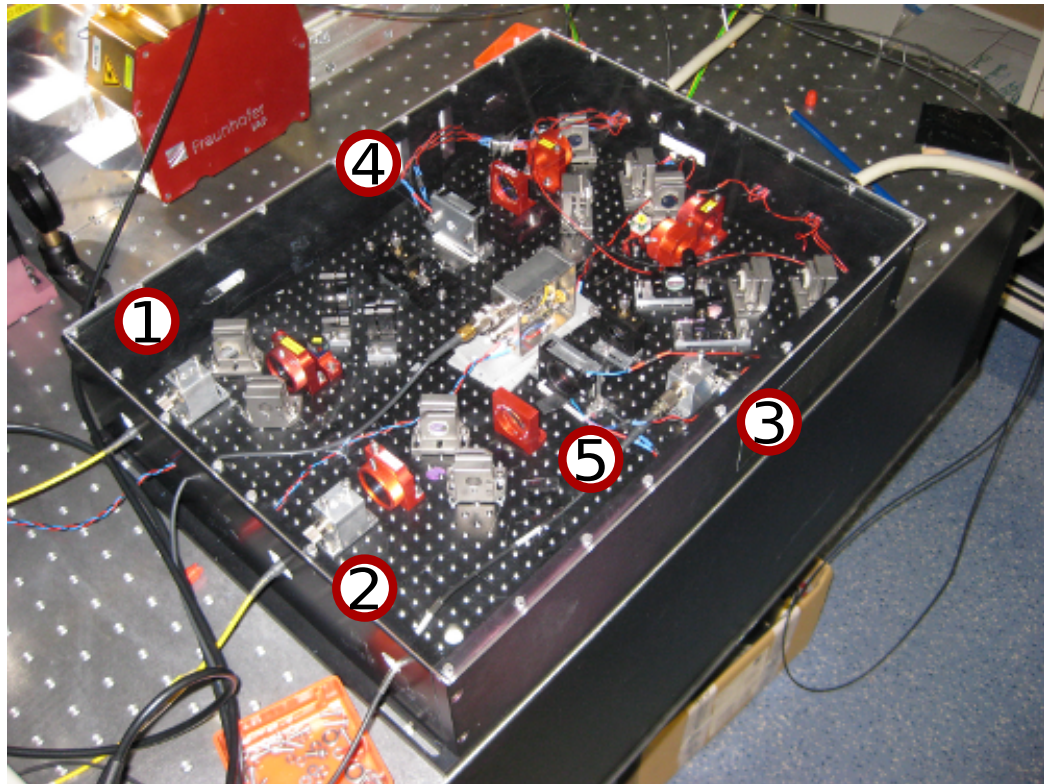


Figure 5.10.: Filterbox. The filterbox setup seals the filter from thermal fluctuations and other environmental effects. The beam coupled in at the FC ① will be filtered at the F ④, the narrow filter, and the F ⑤, the broad filter. The photons from the FC ③ will be filtered only with the broad filter ⑤. At the PBS both beams are brought to overlap. The combined output fibre coupler is ②.

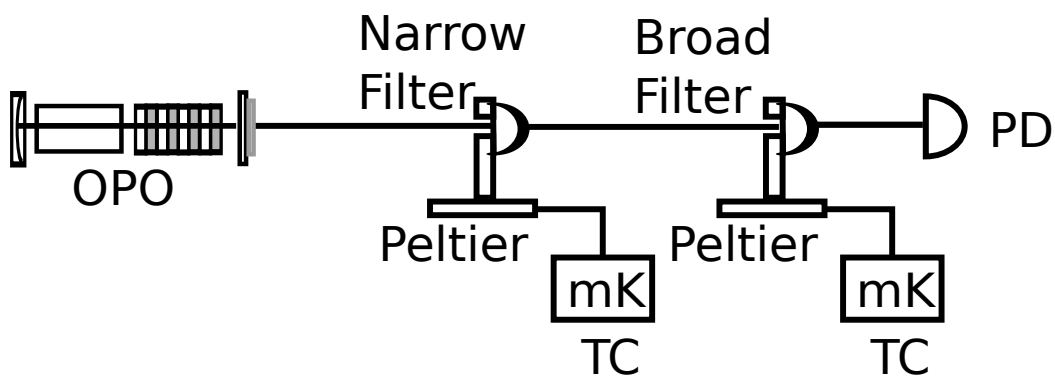


Figure 5.11.: Optical Parametric Oscillator Scanning Setup. The narrow and the broad filter cascaded have a high free spectral range and a high suppression, therefore they were used for optical parametric oscillator (OPO) scanning experiment. The filters were tuned each by a temperature controller (TC). For the scan the central filter frequencies were shifted in parallel. The photo diode (PD) detected the intensity of the scan.

5.4. Optical Parametric Oscillator Conclusion

The measurement of the OPO spectrum was very valuable because it was an interesting benchmark for narrow-band filtering. The result can be seen in figure 5.12, with a zoom in figure 5.13. The measurement data was fitted with the convolution of the filter airy function with the spectrum of the OPO. As it can be seen, slightly more than half of the spectrum was measured. The theoretic spectrum and the measured results are in good accordance.

For future experiments the stabilization of the laser is a key element to improved the scan of the OPO spectrum. A scan of the QD spectrum will be an interesting perspective.

The cascaded Fabry-Pérot filters demonstrated their capabilities in the spectroscopy of the OPO. The spectral resolving power is

$$R = \frac{v}{\delta v} \quad (5.10)$$

with v as the central filter frequency and δv as the FWHM. With a FWHM of 192.81 MHz at 335 THz the spectral resolution is about 1,700,000. For comparison, the cryogenic high-resolution pre-dispersed infrared echelle spectrograph (CRIRES) developed by the European Space Organization has a resolving power of 100,000, operating at wavelength from 0.95 to 5.2 μ m.

In previous high demand stress test, described in chapter 4.3.3, the filter steering seemed to be problematic. As it turned out, the impact on a real experiment is low, if the calibration has been done systematically. The setup can be used for spectroscopy in general. Here near infrared frequencies have been filtered, but the filter principle should be applicable for other wavelength ranges. It might be interesting for thermal emission spectroscopy or astronomy.

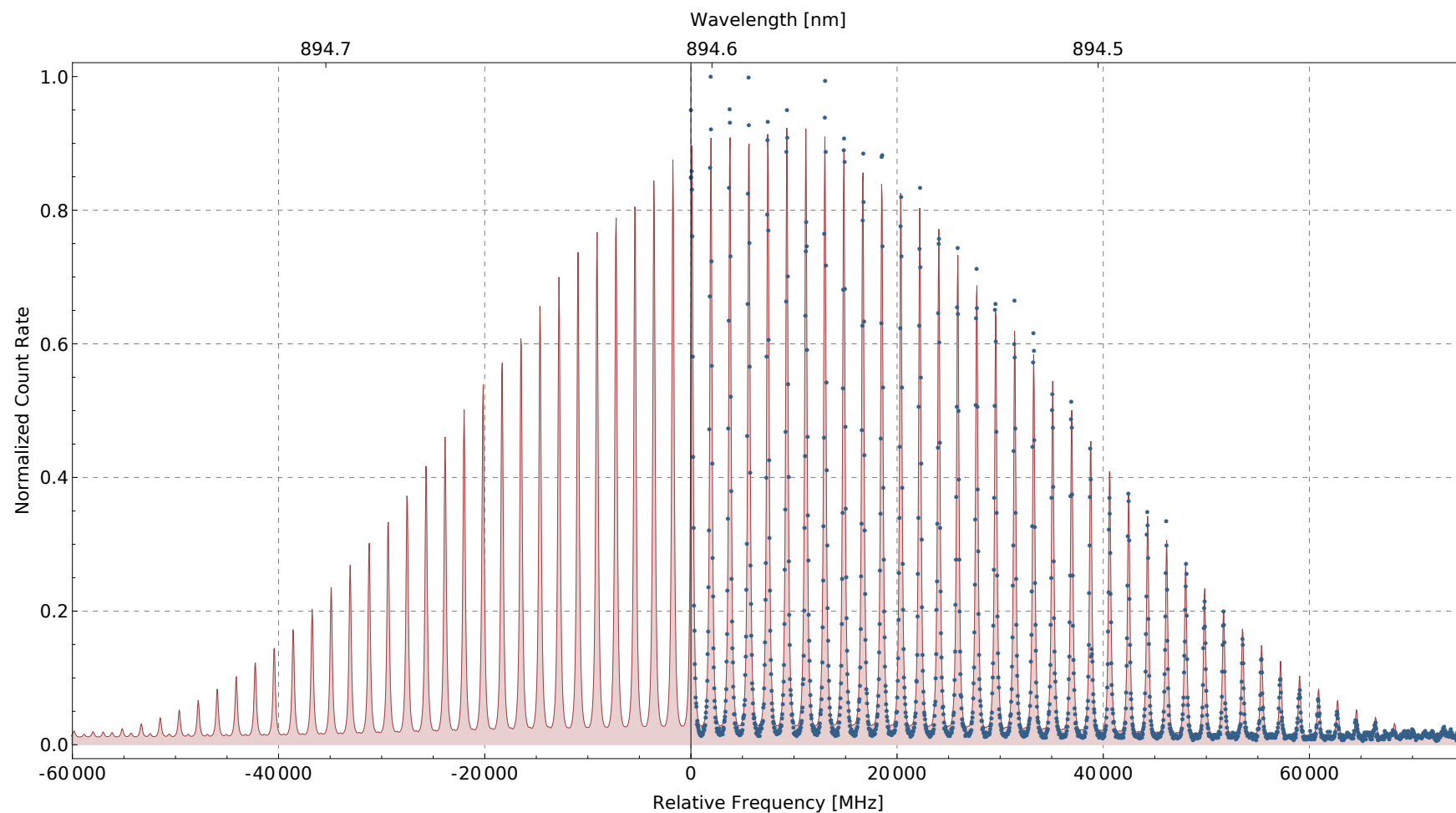


Figure 5.12.: Measured OPO Spectrum. The measured data, the blue dots, overlap very well with the calculated OPO spectrum. The relative frequencies below zero were not measured, as it is expected to mirror the data on the other side.

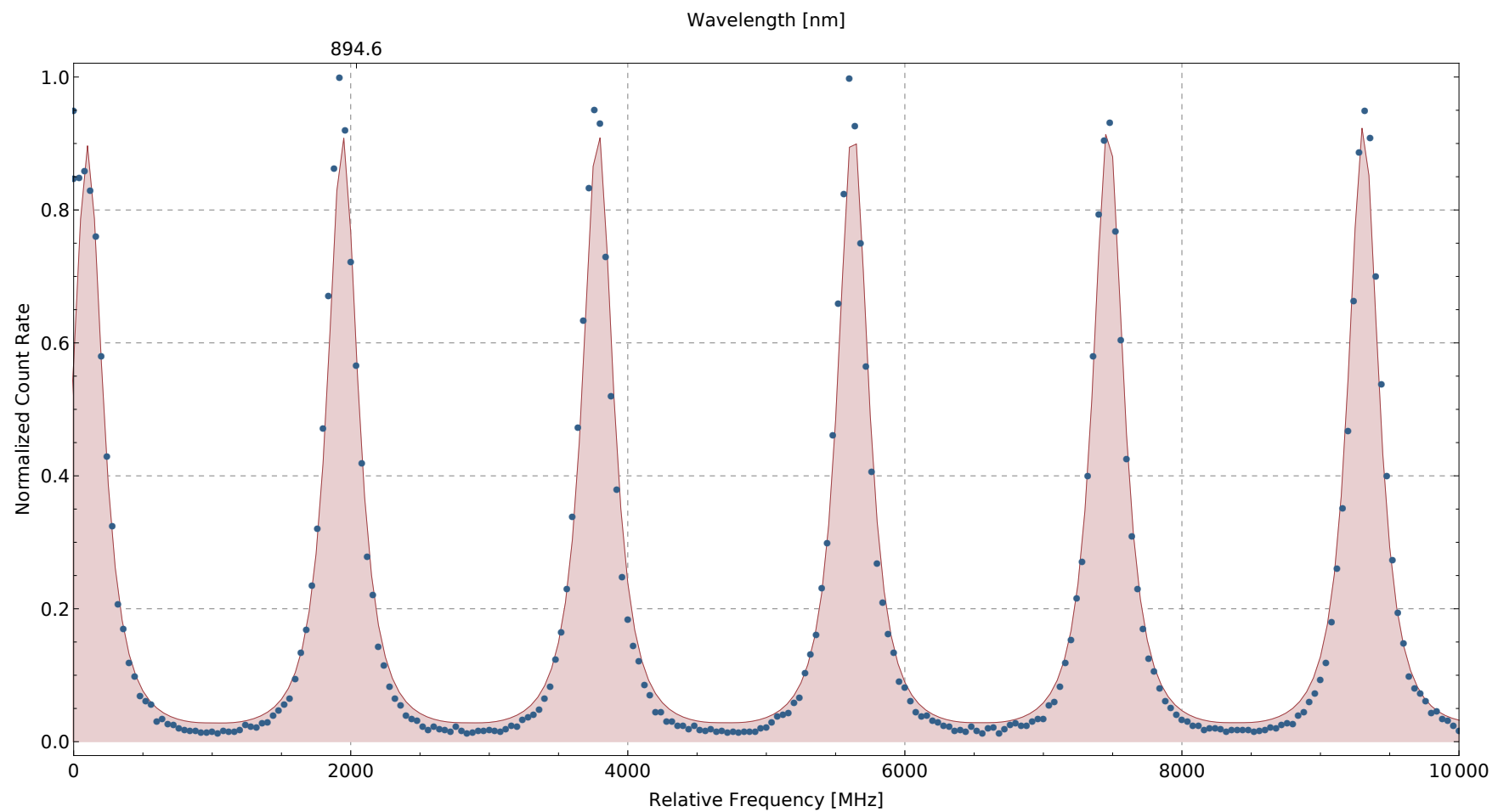


Figure 5.13.: Measured OPO Spectrum Detail. Here a detail of figure 5.12 can be seen. The blue dots are the measured values, while the red curve is the calculated OPO spectrum.

6. Hong-Ou-Mandel Effect with Filtered Photon Pairs

In this chapter the Hong-Ou-Mandel effect is explored to inspect the indistinguishability of OPO photon pairs. The OPO type-II photon pairs are filtered with the cascaded monolithic Fabry-Pérot to a very narrow frequency range. The indistinguishability is then switched based on the polarisation. A short theory for this kind of Hong-Ou-Mandel is outlined.

6.1. Introduction to the Hong-Ou-Mandel Effect

When two distinguishable photons are send to a polarizing beam splitter (PBS), four results may be detected by the photo diodes (PD) behind, as presented in figure 6.1. If the photons are indistinguishable only the two cases of figure 6.2 are allowed by quantum physics. This effect is called the Hong-Ou-Mandel effect, which is, compared with quantum mechanics itself, a recently discovered effect. In the year 1987 Hong, Ou, and Mandel [29] published their paper "Measurement of subpicosecond time intervals between two photons by interference", which showed the so called Hong-Ou-Mandel dip when indistinguishable photons bunch at a beam splitter. Therefore this two-photon interference is a method to probe the indistinguishability of photons.

In the quantum repeater concept of Briegel et al. [9] entanglement swapping is one of the key concepts. As photon indistinguishability is a premise for entanglement swapping, further entanglement swapping experiments can only be conducted, if a Hong-Ou-Mandel effect of high fidelity can be demonstrated.

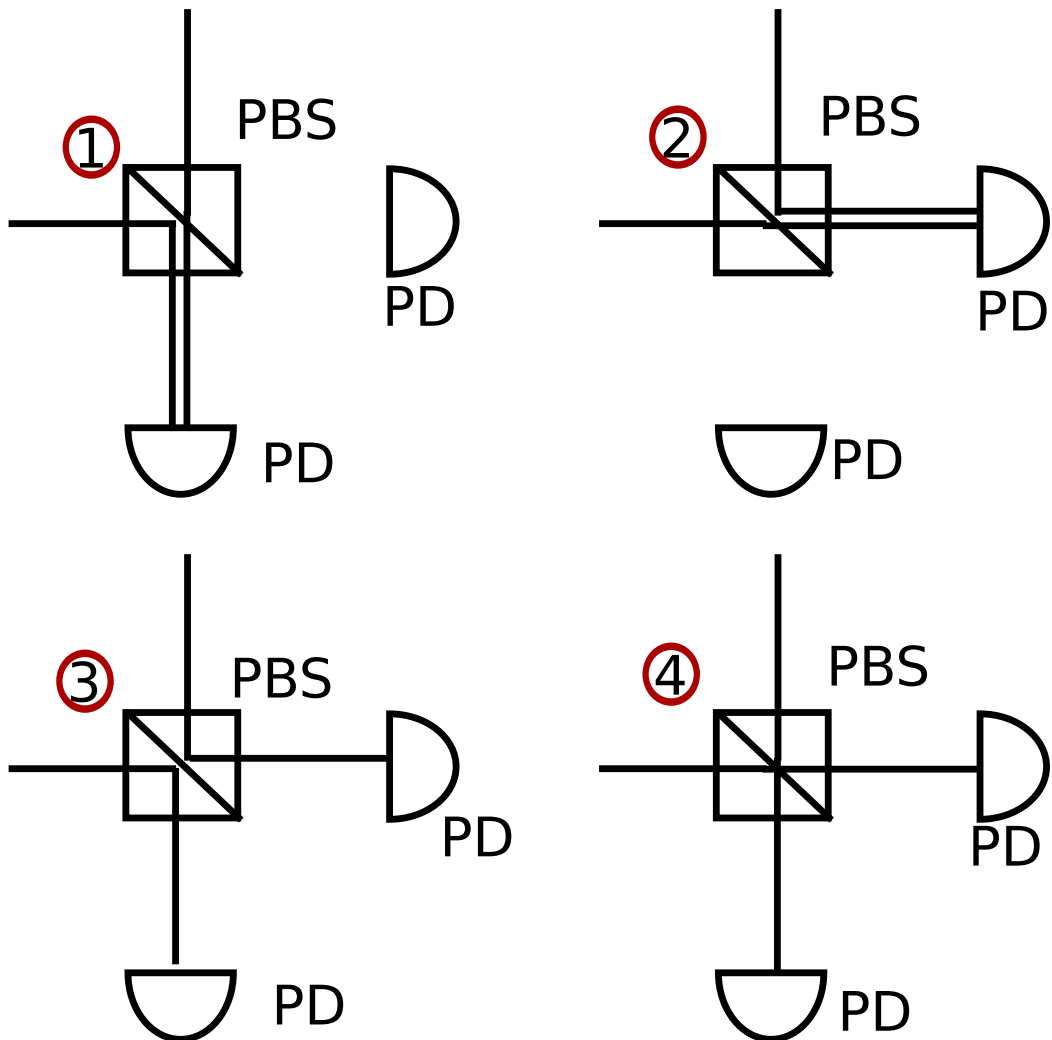


Figure 6.1.: Distinguishable Photons Measurement. If the photons are distinguishable and at the same time at the polarizing beam splitter (PBS), there are, from left to right, four cases the photo diodes (PD) may detect. In the cases ① and ② one photon reflects at and the other one transmits through the beam splitter. In case ③ both photons reflects at the PBS and end up at different detectors. In the case ④ both photons transmit and end up also at different detectors.

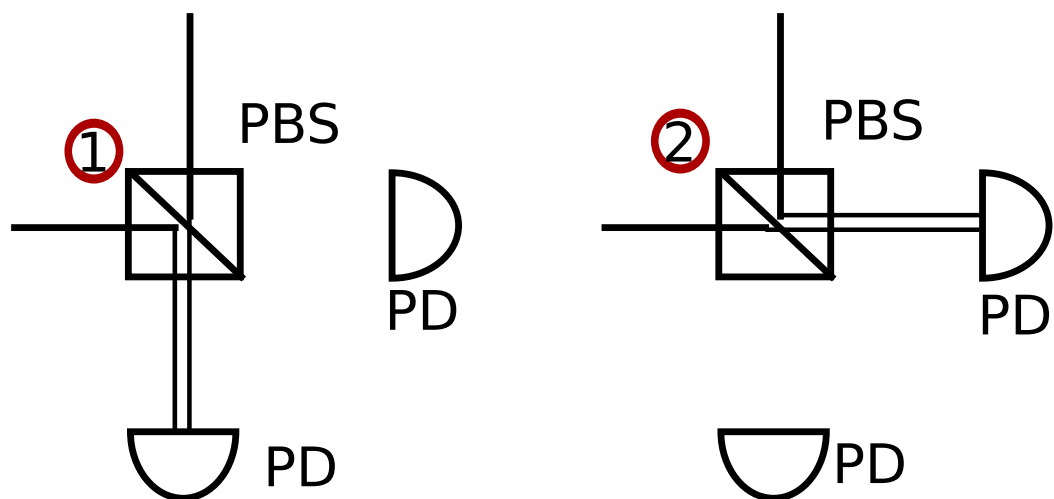


Figure 6.2.: Indistinguishable Photons Measurement. If the photons are indistinguishable and at the same time at the PBS, only the cases (1) and (2) are allowed and the photons always end up at the same photo diode (PD).

6.2. Hong-Ou-Mandel Setup

The setup can be seen in figure 6.3. For a path length based Hong-Ou-Mandel interferometer, a tunable path delay bigger than the correlation length would have to be set up. The correlation length, according to Hong and Mandel [28], is

$$l_{cor} = \frac{c}{b_\omega} \quad (6.1)$$

with bandwidth b_ω . For a bandwidth of 100 MHz it is about 3 m. This experiment could be realised with fibres of different length. Instead of a complex fibre coupled setup, the decision was made to a polarisation based Hong-Ou-Mandel interferometer, which can be build much more compact. The OPO produced degenerate, orthogonal photon pairs at 894 nm, the caesium D1 line, and the cascaded filters were each temperature-tuned to maximise the transmission of the central comb line of the OPO output spectrum. Here the indistinguishability of filtered OPO photon pairs was measured. The results of the birefringence experiment in chapter 4.2.5 could be verified also, as a strong birefringence makes the photon pair more distinguishable or even worse would transmit only one photon of the photon pair and suppress the other.

For the measurement the half-wave plate (HWP) was turned, which shifted the polarisation of the photons. When the fast axis of the HWP has an angle of 22.5° with the polarisations of the photons, the orthogonal polarisations of the photons are projected onto the same polarization plane. The photons are then indistinguishable and bunch at a polarizing beam splitter (PBS). Behind the PBS the coincidence count rate was measured with avalanche photo diodes behind each arm of it.

The creation operators \hat{a}^\dagger for photons in the input mode are defined for vertical and horizontal polarisation[41, 49], as it can be seen in figure 6.4. With the a perfect PBS the following relations

$$\begin{aligned} \hat{b}_H^\dagger &= \hat{a}_H^\dagger \\ \hat{b}_V^\dagger &= -\hat{a}_V^\dagger \end{aligned} \quad (6.2)$$

for the output modes are valid. The sign in front of \hat{a}_V^\dagger is caused by the phase shift of the reflection. Without the HWP, or with an polarisation angle $\theta = 0$, the input state is

$$|\psi(\theta = 0)\rangle = |1_H, 1_V\rangle \equiv |1,1\rangle \quad (6.3)$$

$$= \hat{a}_H^\dagger \hat{a}_V^\dagger |0,0\rangle . \quad (6.4)$$

If $\theta \neq 0$ the polarisations of the input state are rotated:

$$|\psi(\theta)\rangle = \left[(\hat{a}_H^\dagger \cos \theta + \hat{a}_V^\dagger \sin \theta) (-\hat{a}_H^\dagger \sin \theta + \hat{a}_V^\dagger \cos \theta) \right] |0,0\rangle . \quad (6.5)$$

If both detectors measure a coincidence, the state is projected into

$$|\psi_{coinc}\rangle = |1,1\rangle = \hat{b}_H^\dagger \hat{b}_V^\dagger |0,0\rangle , \quad (6.6)$$

the expectation value then can be calculated as

$$P(\theta) = \langle \psi(0) | \psi_{coinc} \rangle \langle \psi_{coinc} | \psi(0) \rangle = |\langle \psi(0) | \psi_{coinc} \rangle|^2 . \quad (6.7)$$

Using the bosonic commutator relation $[\hat{a}^\dagger, \hat{a}^\dagger] = 1$ and the definition of the equations 6.2, 6.5, and 6.6, it leads to

$$P(\theta) = \cos^2(2\theta) = \cos^2(4\alpha) . \quad (6.8)$$

The angle of the HWP is $\alpha = 2\theta$.

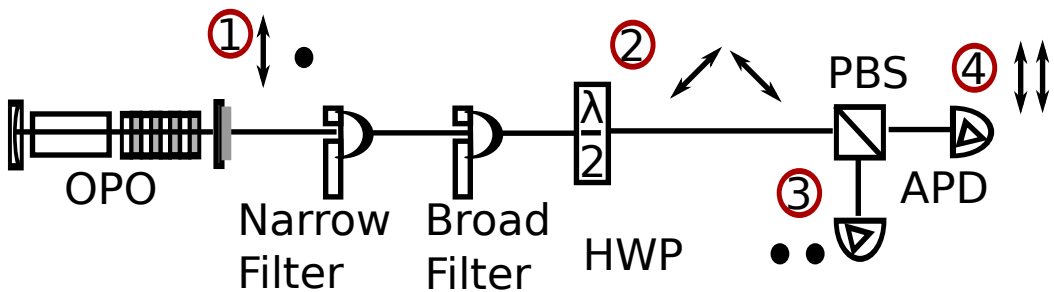


Figure 6.3.: Hong-Ou-Mandel Experiment Setup. Light from the optical parametric oscillator is coupled into the filters through a half-wave plate onto a polarizing beam splitter (PBS). After the PBS a avalanche photo diode on each arm measures the arrival of the photons. A coincidence counter derived from those two signals a gauge. Directly behind the OPO at position ① the photons have orthogonal polarisations. When the HWP is turned to an angle of 22.5° , the photons are polarized in the 45° direction with respect to the PBS at position ②. The photons then are indistinguishable and bunch. They are either measured at the avalanche photo diode at position ③ or ④.

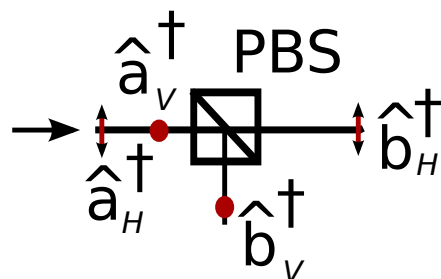


Figure 6.4.: Hong-Ou-Mandel Theory. The creation operators before the PBS are on the left side.

6.3. Results and Discussion

The results can be seen in figure 6.5. By rotating the HWP in steps of 5° over multiple maxima and minima of indistinguishability, a visibility was measured,

$$\text{Visibility} = \frac{\text{Count-Rate}_{\max} - \text{Count-Rate}_{\min}}{\text{Count-Rate}_{\max} + \text{Count-Rate}_{\min}} \quad (6.9)$$

of $96 \pm 1.5\%$ and with the background subtracted $97 \pm 1.5\%$. There was a noise level of 3 % which is a result of detector dark counts and imperfections of the optical elements. Optical imperfections are for example a non unity ratio between reflectivity and transmission in the beam splitter. It was tried to compare the result with a measurement of the same Hong-Ou-Mandel setup except the filter, but this turned out to be very difficult.

In 2002 Santori et al. [57] measured the Hong-Ou-Mandel effect by varying the path length of one of the photons, and hence the relative arrival time at the beam splitter to observe the well-known Hong-Ou-Mandel dip and achieved a visibility of 69 %. They measured their optical imperfections separately and when taken into account the visibility was 81 %. They used quantum dots as their single photon sources and in their paper[57], they mention photon pair generation is more difficult with such sources.

Wolfgramm et al. [72] used a type-II degenerate OPO like in their experiment. They varied the path length of the photons like Santori et al. [57]. Without spectral filtering they measured a visibility of 90 %.

The measured visibilities of the other groups are slightly lower than the visibility measured in this experiment. The next step will be measuring the Hong-Ou-Mandel effect with quantum dot and OPO photons.

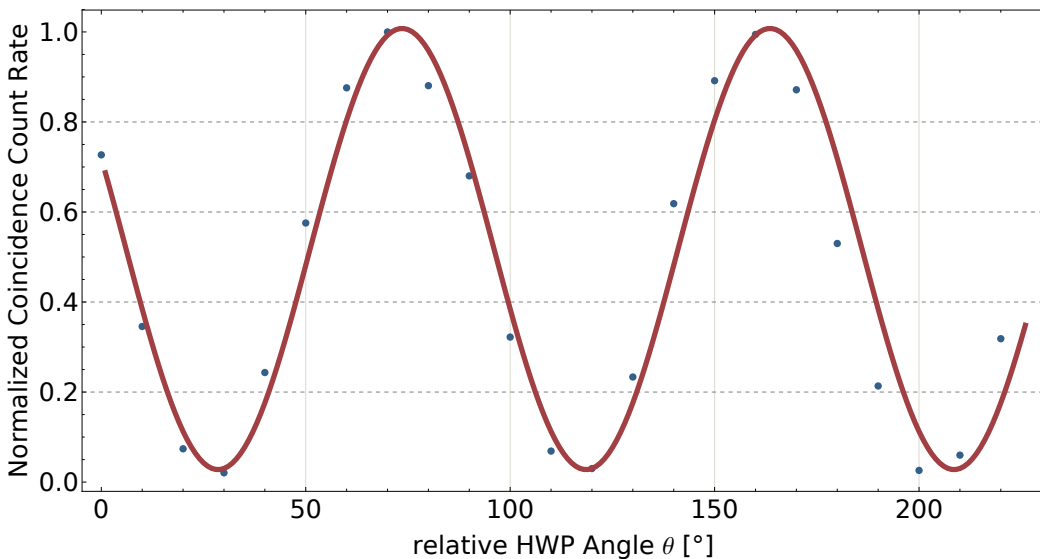


Figure 6.5.: Hong-Ou-Mandel Visibility. This figure shows the result of the Hong-Ou-Mandel experiment. The visibility is 96 %, with a coincidence window of 30 ns

6.4. Hong-Ou-Mandel Effect Conclusion

The Hong-Ou-Mandel effect was shown with a visibility of 97 %. It is an achievement compared with already published results of other groups[57, 72]. The cascaded filters have got a high photons selectivity.

Indistinguishability is a precondition to entangle photons and entanglement is precondition for many applications beyond quantum cryptography, such as superdense coding[4] or entangled photon interferometry[6]. Indistinguishable photons are an important research tool, to advance the understanding of this concepts.

The filters can projected all photons towards indistinguishability in the frequency domain. These might be useful for channel testing in quantum communication or as perimeter security in yet to be developed quantum devices. At least the filters will stop distinguishable photons, before they enter a quantum channel and would be cached in quantum memories.

7. Conclusion and Outlook

Before outlining future experiments, will follow a short summary of the achieved results, which were described in the previous chapters. The monolithic Fabry-Pérot filter system was successfully designed, set up, and characterised. The central filter frequency was stable over hours of measurement. The stability was three times better than other groups[51] have published. The cascaded monolithic Fabry-Pérot filter system has a free spectral range of about 500 GHz and a suppression up to 60 dB. These properties and the tunability of the central filter frequency allow experiments such as spectroscopic studies of the OPO to be conducted. The measurement showed a very good overlap between theory and measurement. The polarisation based Hong-Ou-Mandel experiment was a vital first step towards entanglement swapping with photons from dissimilar sources. Here a visibility of 97 % was shown, which is higher than comparable experiments in other groups[57, 72].

7.1. Filtering Quantum Dot Photons

After filtering the OPO, the QDs will be filtered next. The challenge at hand is to find a QD with an emission wavelength near the caesium D1-line and a high Signal-to-Noise ratio. Typically the maximum emission of the QDs is not exactly at the caesium D1-line, but slightly off. There are several techniques to tune the emission of QDs. Kroh [38] mentions temperature tuning, the electrostatic Stark-effect and mechanical deformation of the semiconductor crystal with the piezo-electrical effect. Then the central filter frequency of the cascaded filter system and QD emission need to be brought into overlap. A frequency spectroscopy of the QD emission will be measured. The interesting QD range around the peak is about 200 GHz, which is of the same order as the measured OPO spectrum. The high tunability of the cascaded filters will allow to cover the wide range. The high resolution of 40 MHz might reveal structures in the emission, that until now could only be calculated.

The filtering is important, because for further experiments, the QD photons should be limited to a small frequency range. Since the current setup is fibre-coupled, no further changes need to be made. The new light source simply needs to be connected for a measurement to be performed.

7.2. Indistinguishability

Having filtered the QD photons, the indistinguishability of OPO photons and QD photons will be verified. The challenge will be to keep the QD emission stable over

hours. A locking mechanism using one of the previously mentioned techniques can take care of this problem. The emission frequency and the count rate tend to drift when the measurement lasts hours. The above mentioned QD tuning mechanism will apply here, too. To achieve a high visibility the QD photons must be polarisation selected. One half of the selection can be used for feedback. It is similar to the OPO, when it is used in heralded mode. In the heralded mode one polarisation is measured and the other is used for the experiment. Both sources will thus be linearly polarised.

The single photons will be sent through the same filter system to minimise drift effects of the central filter frequency. The indistinguishability of QD photons and OPO photons will be measured by demonstrating the Hong-Ou-Mandel effect. The setup will be comparable to that setup for the experiment in chapter 6.

7.3. Entanglement Swapping

Following the indistinguishability experiments, the entanglement swapping will be the next step. Entanglement swapping is a core element of the quantum repeater. A fully functional quantum repeater is a precondition for long distance quantum communication.

A QD spin photon entanglement, like here[20, 12] for polarisation, has been achieved. OPO photons are entangled by default. Connecting the dots, the next step will be to measure the Bell-state of one entangled OPO photon and the QD photon. Their indistinguishability will be prepared with the cascaded filters, that are evaluated in this thesis. The second OPO will be measured to verify the entanglement swapping.

In this thesis a cascaded monolithic Fabry-Pérot filter system has been set up. The filter properties were measured and exceeded the expectations, especially regarding the long term stability. The fast and flexible tuning by the temperature controller permitted to scan the OPO spectrum with a high resolution. The OPO photon pairs were filtered indistinguishable and a high visibility of the Hong-Ou-Mandel effect could be achieved. A single frequency mode was filtered from the OPO spectrum, and photons within this mode were shown to be indistinguishable, as demonstrated by the high visibility of the Hong-Ou-Mandel effect. A new scientific tool has been set up and applied, which will be used for future quantum repeater experiments, especially regarding the entanglement swapping with photons from dissimilar sources.

A. Derivation of the Ideal Fabry-Pérot Interferometer

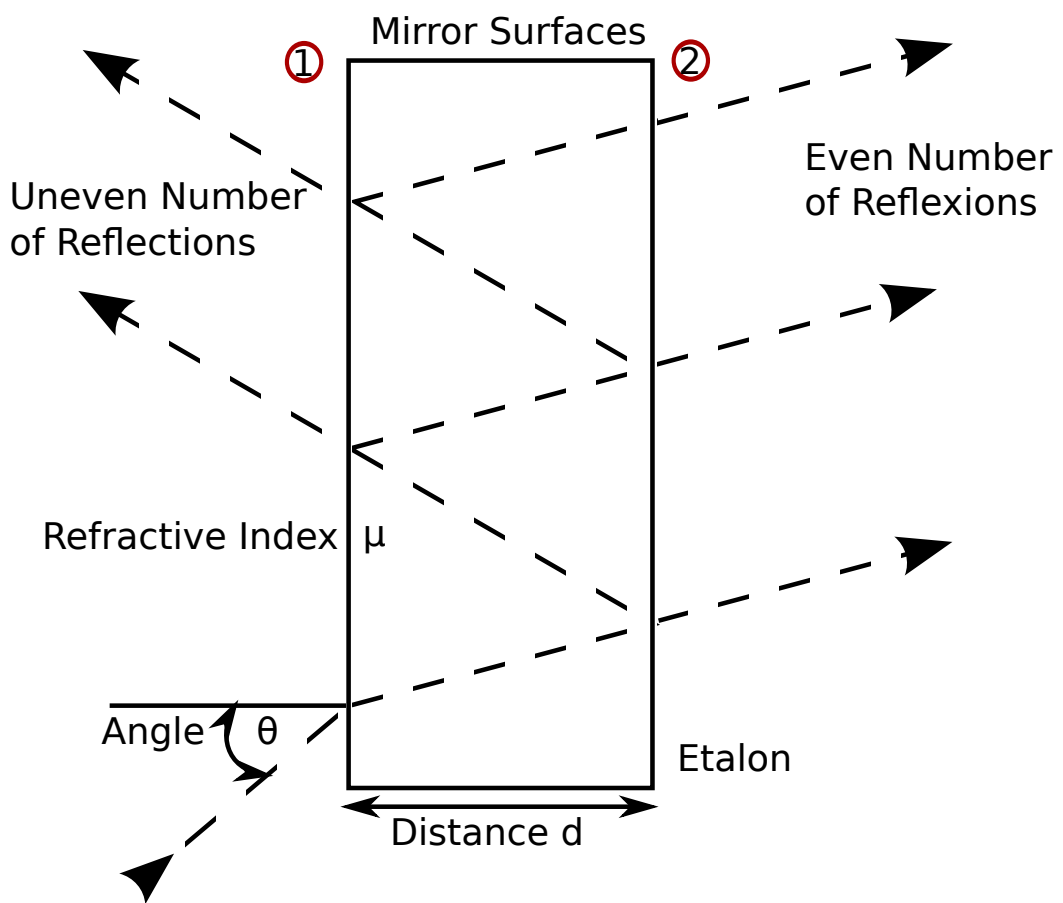


Figure A.1.: Fabry-Pérot Interferometer. Light with wave number σ coming from the left is coupled under angle θ into etalon with distance d , mirrors ① and ②, where a part is reflected and a part is transmitted. After an even number of reflections the light is transmitted back to the left or after an uneven number of reflections light is transmitted to the right. The parallel emittances on one side meet in a point far off, where they interfere.

The heart of a Fabry-Pérot Interferometer is the etalon, which consists of two parallel mirrors, namely mirror ① and mirror ②, separated by distance d . These mirrors may be at the edge of a glass slab. A light beam with wave number σ under angle θ is sent onto one of the mirrors. As it can be seen in figure A.1, one part of the beam is reflected and the rest is transmitted and impinges on the surface of the next mirror,

where it is partly reflected and partly transmitted. Those parts of the beam leaving to the left experience an uneven number of reflections, those leaving on the right side experience an even number. For ease of reading, the former is from now on called the uneven way, the latter the even way. A practical etalon may be a glass slab with the refractive index μ and coated, high reflective thin films on the surfaces as mirrors. On both sides of the glass slab lenses collect the light and concentrate it in a focal point, where it interferes. The following notation is used for a theoretical description of the etalon:

$$\begin{aligned}
 r_x &:= \text{complex reflection amplitude coefficient} \\
 t_x &:= \text{complex transmission amplitude coefficient} \\
 &\quad "x" \text{ indicates direction of the ray, towards medium 1} \\
 &\quad \text{or towards the glass slab as medium 2} \\
 \Phi &:= 4\pi\mu d\sigma \cos \Theta \quad (\text{A.1}) \\
 &\quad \text{phase lag due to additional path in the cavity}
 \end{aligned}$$

The intensity of the uneven path is made up of the terms

$$r_1 t_1^2 r_2 \exp(i\Phi), t_1^2 r_2^3 \exp(2i\Phi), \dots . \quad (\text{A.2})$$

The first term represents light being reflected on the interface of mirror 1. The second term stands for light transmitted through mirror 1, reflected on interface of mirror 2 and finally transmitted through mirror 1 again. The other terms follow the same scheme. Analogous these are

$$t_1 t_2, t_1 t_2 r_2^2 \exp(i\Phi), t_1 t_2 r_2^4 \exp(2i\Phi) \quad (\text{A.3})$$

the terms of the even way. The amplitude summation for the uneven path can then be written as

$$A_r(\Phi) = r_1 + t_1^2 r_2 \exp(i\Phi) + \dots .$$

When the light finally transmits through the slab on the even way, the sum of amplitudes can be described by

$$A_t(\Phi) = t_1 t_2 + t_1 t_2 r_2^2 \exp(i\Phi) + \dots .$$

When the reflectivity of both mirrors is the same, the complex reflection amplitude coefficients r_x are equal except for a factor of -1. This could also apply for the complex transmission amplitude coefficients t_x , but this variant will not be examined any

further. The relations

$$\begin{aligned} r_1 &= -r_2 \\ r_1^2 &= r_2^2 = R \\ t_1 t_2 &= T \end{aligned} \tag{A.4}$$

are valid here. The phase change of additional rays compared to the zeroth order ray by the additional path has already been included in equations. Still missing is the amount of phase change by the reflection, referred to as χ and leading to an combined phase change of

$$\delta = \Phi + 2\chi . \tag{A.5}$$

If one applies these enhancements to the equations, the sums of the amplitudes are

$$A_r(\delta) = \left[(1 - \exp(i\delta)(R + T)) R^{\frac{1}{2}} \right] (1 - R \exp(i\delta))^{-1} \tag{A.6}$$

$$A_t(\delta) = T (1 - R \exp(i\delta))^{-1} . \tag{A.7}$$

As these complex amplitudes cannot be measured, the calculated intensities are of interest. The intensities Y_r and Y_t are given by the product of the amplitude and its complex conjugate:

$$\begin{aligned} Y_r(\delta) &= A_r(\delta) A_r^*(\delta) \\ \Rightarrow Y_r(\delta) &= R \left[1 - 2(R + T) \cos \delta + (R + T)^2 \right] \left[1 + R^2 - 2R \cos \delta \right]^{-1} \end{aligned} \tag{A.8}$$

$$\begin{aligned} Y_t(\delta) &= A_t(\delta) A_t^*(\delta) \\ \Rightarrow Y_t(\delta) &= T^2 \left[1 + R^2 - 2R \cos \delta \right]^{-1} \end{aligned} \tag{A.9}$$

The equations A.8 and A.9 give the measurable intensities. To calculate these intensities, the phase change δ , the reflectivity coefficient R , and the transmission coefficient T need to be known. Only the transmission coefficient T or the reflectivity coefficient R are mandatory tough, as every photon interacting with the etalon gets either reflected, transmitted, or absorbed. Therefore with absorption E , it leads to

$$1 = R + T + E \Rightarrow R + T = 1 - E . \tag{A.10}$$

Applying this to the upper equations leads to:

$$Y_r(\delta) = R [1 - 2(1 - E) \cos \delta + (1 - E)^2] \left[1 + R^2 - 2R \cos \delta \right]^{-1} \tag{A.11}$$

$$Y_t(\delta) = \left[1 - E(1 - R)^{-1} \right]^2 (1 - R)^2 \left[1 + R^2 - 2R \cos \delta \right]^{-1} \tag{A.12}$$

In an ideal interferometer the absorption $E = 0$, so that $Y_r(\delta) + Y_t(\delta) = 1$ and every photon of the incoming light is finally either reflected or transmitted. Using the refined intensities are

$$Y_r(\delta) = [2R - 2R \cos \delta] \left[1 + R^2 - 2R \cos \delta \right]^{-1} \quad (\text{A.13})$$

$$Y_t(\delta) = (1 - R)^2 \left[1 + R^2 - 2R \cos \delta \right]^{-1} \quad (\text{A.14})$$

$$\Rightarrow Y_r(\delta) + Y_t(\delta) = \frac{[2R - 2R \cos \delta] + (1 - R)^2}{[1 + R^2 - 2R \cos \delta]} = \frac{1 + R^2 - 2R \cos \delta}{1 + R^2 - 2R \cos \delta} = 1. \quad (\text{A.15})$$

A closer inspection of equation A.13 reveals that the maximum exists for

$$\delta = 0 \Rightarrow \delta = 2 \left(n + \frac{1}{2} \right) \pi \quad (\text{A.16})$$

with n being a positive integer. Complimentary to that, the maximum for equation A.14 is

$$\delta = 1 \Rightarrow \delta = n2\pi. \quad (\text{A.17})$$

Following now the even path of the transmitted light and remembering the definitions for δ (A.5) and Φ (A.1), it should be notified that for the even path

$$\delta = \Phi = 4\pi\mu d\sigma \cos \Theta, \quad (\text{A.18})$$

as the phase changes caused by an even number of reflections cancel each other out. The positive integer n depends on the refractive index μ , the wave number σ and the incidence angle Θ .

$$n = \frac{\delta}{2\pi} = 2\mu d\sigma \cos \Theta \quad (\text{A.19})$$

B. Filter Properties Overview

Table B.1.: Filter Properties Overview.

Name:	Narrow	Broad
Thickness [mm]:	2.6 ± 0.2	3.6 ± 0.2
Curvature [mm]:	64.4	38.6
Surface Quality:	5/4 x 0.025 according to ISO 10110	
Material:	BK7	
Refractive Index:	1.50909	
Reflectivity [%]:	98.89 ± 2	92.36 ± 2
Vendor:	Laser Components	
FWHM [MHz]:	192.81 ± 0.81	883.7 ± 2.5
Suppression [dB]:	40.2	25.6
Free Spectral Range [MHz] :	37788 ± 19	28826 ± 24
Finesse:	149.5 ± 0.8	42.8 ± 0.1
Tunability Offset after 80 h [MHz]:	110	80
Tunability Amplitude after 80 h [%]:	43.74	96.82
Stability Offset after 10 h [MHz]:	10.15 ± 0.51	15.4 ± 2.3
Stability Amplitude after 20 h [%]:	95.75	99.51
Stability Root Mean Square:	0.024 FWHM	0.0083 FWHM
Internal Name:	QD6	OPO1

List of Abbreviations

APD	Avalanche Photo Diode
BS	Beam Splitter
CFS	Cascaded Monolithic Fabry-Pérot Filter System
CSV	Comma Separated Values
EOM	Electrial Optical Modulator
FWHM	Full Width Half Maximum
FSR	Free Spectral Range
HWHM	Half Width Half Maximum
HWP	Half Wave Plate
KTP	Potassium Titanyl Phosphate ($KTiOPO_4$)
OPO	Optical Parametric Oscillator
PBS	Polarizing Beam Splitter
PD	Photo Diode
PPKTP	Periodic Poled Potassium Titanyl Phosphate
QD	Quantum Dots
RMS	Root Mean Square
SNR	Signal-to-Noise-Ratio
SPDC	Spontaneous Parametric Down-Conversion

List of Figures

2.1. Photon Arrival Times Schematic	11
2.2. Coincidence Count Rates of Different Sources	12
2.3. BB84 Protocol	14
2.4. Quantum Repeater Implementation	15
2.5. Long Distance Quantum Communication	16
3.1. Fabry Pérot Interferometer Principle	18
3.2. Free Spectral Range Explanation	19
3.3. Full Width Half Maximum Explanation	20
3.4. Etalon Stability Diagram	25
3.5. Gaussian Beam in the Plan Parallel Cavity	27
4.1. The Plan-Convex Lens	30
4.2. Full Width Half Maximum over Reflectivity	30
4.3. Free Spectral Range over Thickness	31
4.4. Suppression over Reflectivity	31
4.5. Filter Setup	33
4.6. Narrow Filter Transmission	34
4.7. Broad Filter Transmission	35
4.8. Line Width Setup	35
4.9. Caesium Absorption near D1-Line	36
4.10. Line Width Filter Scan	37
4.11. Free Spectral Range Setup	38
4.12. Measured Free Spectral Range for the Narrow Filter	39
4.13. Measured Free Spectral Range of the Broad Filter	39
4.14. Birefringence Setup	41
4.15. Filterbox Heater	42
4.16. The Reactivity of the Old Heater	43
4.17. The Reactivity of the new Heater	43
4.18. Heater Reactivity	43
4.19. Free Space Filter Heater	44
4.20. Free Space Filter Schematic	44
4.21. Drift of the Central Filter Frequency	46
4.22. Long Term Stability Setup	46
4.23. Long Term Stability of the narrow Filter	47
4.24. Long Term Stability of the broad Filter	47
4.25. Tunability Setup	49
4.26. Tunability of the Narrow Filter	49

4.27. Tunability Detail of the Narrow Filter	50
4.28. Tunability of the Broad Filter	50
4.29. Tunability Detail of the Broad Filter	51
4.30. Suppression Setup	52
5.1. Quantum Dot Spectrum	54
5.2. Down-Conversion	57
5.3. Quasi Phase Matching	58
5.4. Calculated Down-Conversion Spectrum	59
5.5. Optical Parametric Oscillator Principal	60
5.6. Calculated OPO Spectrum	61
5.7. Cascaded Filter Free Spectral Range	63
5.8. Filterbox Heater	63
5.9. Filterbox Schematic	64
5.10. Filterbox	65
5.11. Optical Parametric Oscillator Scanning Setup	65
5.12. Measured OPO Spectrum	67
5.13. Measured OPO Spectrum Detail	68
6.1. Distinguishable Photons Measurement	70
6.2. Indistinguishable Photons Measurement	71
6.3. Hong-Ou-Mandel Experiment Setup	73
6.4. Hong-Ou-Mandel Theory	73
6.5. Hong-Ou-Mandel Visibility	74
A.1. Fabry-Pérot Interferometer	78

Publications and Talks

- C. Berkemeier, A. Ahlrichs, A. W. Schell, O. Dietz, T. Kroh, B. Sprenger, and O. Benson: *Towards indistinguishability of photons from dissimilar sources*, Talk, DPG Tagung, 18. - 22. March 2013, Hannover

Abstract:

Long-distance quantum key distribution will require quantum repeater nodes, which are necessary for entanglement swapping between entangled photon pairs. A first step towards this goal is tailoring photons from dissimilar sources, in this case quantum dots and a photon pair source, to be indistinguishable in all degrees of freedom [1]. To increase the distance between nodes, single photon conversion into the telecommunications bands as shown in [2] could interconnect the different units with a low damped wavelength for long distance transmission in fiber.

The sources we use are single photons from quantum dots, and those from a parametric downconversion source in a cavity. We present a cascaded Fabry-Pérot filtering system, based on [3], which is simultaneously applied on photons from both sources. The quantum dot photons are filtered to 100 MHz width, and the system is optimized for long-term stability.

[1] Solomon et al., J. Opt. Soc. Am. B, 29, 319 (2012)

[2] Zaske et al., Opt. Express, 19, 12825 (2011)

[3] Palittapongarnpim et al., Rev. Sci. Instrum. 83, 066101 (2012)

- A. Ahlrichs, C. Berkemeier, B. Sprenger, and O. Benson: *A monolithic polarization-independent frequency-filter system for filtering of photon pairs*, Applied Physics Letters 103, 241110 (2013);

URL: <http://dx.doi.org/10.1063/1.4846316>

Acknowledgement

Ich möchte mich bei den Menschen bedanken, die einen Anteil hatten an dem Gelingen der Diplomarbeit:

Zuerst bei Professor Oliver Benson, der mir die Gelegenheit geben hat, interessante Experimente in der Quantenoptik durch zu führen.

Professor Axel Hoffmann, vom Institut für Festkörperphysik an der Technischen Universität Berlin, der sich bereit erklärt diese externe Diplomarbeit an der Humboldt Universität als Erstgutachter zu betreuen.

Dr. Benjamin Sprenger und Andreas Ahlrichs, mit denen ich lange und interessante Stunden im und ums Labor verbracht habe.

Dipl.-Ing Klaus Palis konnte mir mit seinem Sachverstand immer einen Rat geben, wenn ich ihn brauchte.

Bei Regina Rheinländer konnte ich fast alle meine Rechnung lassen und sie war immer meine erste Ansprechpartnerin, wenn ich Orientierung in der Humboldt Verwaltung brauchte.

Bei der Elektrowerkstatt der Humboldt Universität habe ich mehrmals Tipps abgeholt, als um den Aufbau eines Netzteils ging. Die mechanische Werkstatt hat unsere Wärmeleitungelemente passgenau gefräst.

Das Beschichtungslabor der Technischen Universität hat netterweise die Linsen, die hier so erfolgreich vermessen und benutzt wurden, kostenlos beschichtet.

Meine Korrekturlesern Bene, Daniela, Dave, Einar, Jan, Stefan und Sven haben die Arbeit als ganzes oder in Teilen gelesen.

Meinen Eltern und meinen Geschwistern haben mich während meines Studiums immer unterstützt.

Bibliography

- [1] Andreas Ahlrichs et al. "Photon Pairs from Cavity-Enhanced Parametric Down-Conversion with Tunable Bandwidth for Quantum Interfaces". In: *Research in Optical Sciences*. Optical Society of America, 2012, QT3A.3. doi: 10.1364/QIM.2012.QT3A.3.
- [2] C. H. Bennett and G. Brassard. "Quantum Cryptography: Public key distribution and coin tossing". In: *Proceedings of the IEEE International Conference on Computers, Systems, and Signal Processing*. (Dec. 10–12, 1984). IEEE. Bangalore, 1984.
- [3] Charles H. Bennett. "Quantum cryptography using any two nonorthogonal states". In: *Phys. Rev. Lett.* 68 (21 May 1992), pp. 3121–3124. doi: 10.1103/PhysRevLett.68.3121.
- [4] Charles H. Bennett and Stephen J. Wiesner. "Communication via one- and two-particle operators on Einstein-Podolsky-Rosen states". In: *Phys. Rev. Lett.* 69 (20 Nov. 1992), pp. 2881–2884. doi: 10.1103/PhysRevLett.69.2881.
- [5] Ludwig Bergmann, Clemens Schaefer, and Heinz Niedrig. *Lehrbuch der Experimentalphysik, Bd.3, Optik*. Gruyter, 1993. ISBN: 3110129736.
- [6] Agedi N. Boto et al. "Quantum Interferometric Optical Lithography: Exploiting Entanglement to Beat the Diffraction Limit". In: *Phys. Rev. Lett.* 85 (13 Sept. 2000), pp. 2733–2736. doi: 10.1103/PhysRevLett.85.2733.
- [7] Dirk Bouwmeester, Artur Ekert, and Anton Zeilinger, eds. *The Physics of Quantum Information: Quantum Cryptography, Quantum Teleportation, Quantum Computation*. Springer, 2000. ISBN: 3540667784.
- [8] Robert W. Boyd. *Nonlinear Optics, Third Edition*. Academic Press, 2008. ISBN: 0123694701.
- [9] H.-J. Briegel et al. "Quantum Repeaters: The Role of Imperfect Local Operations in Quantum Communication". In: *Phys. Rev. Lett.* 81 (26 Dec. 1998), pp. 5932–5935. doi: 10.1103/PhysRevLett.81.5932.
- [10] A. Burch and James M. Gerrard. *Introduction to Matrix Methods in Optics*. John Wiley & Sons, London, New, 1975. ISBN: 0471296856.
- [11] S Castelletto et al. "On the measurement of two-photon single-mode coupling efficiency in parametric down-conversion photon sources". In: *New Journal of Physics* 6.1 (2004), p. 87.
- [12] Kristiaan De Greve et al. "Quantum-dot spin-photon entanglement via frequency downconversion to telecom wavelength". In: *Nature* 491.7424 (Nov. 2012), pp. 421–425. ISSN: 0028-0836.

- [13] R.H. Dicke. "Molecular amplification and generation systems and methods". US Patent 2 851 652. Sept. 9, 1958.
- [14] L.-M. Duan et al. "Long-distance quantum communication with atomic ensembles and linear optics". In: *Nature* 414.6862 (Nov. 2001), pp. 413–418. doi: 10.1038/35106500.
- [15] Frank J. Duarte. *Tunable Laser Optics*. Academic Press, 2003. ISBN: 0122226968.
- [16] M. D. Eisaman et al. "Invited Review Article: Single-photon sources and detectors". In: *Review of Scientific Instruments* 82.7 (2011), p. 071101. doi: 10.1063/1.3610677.
- [17] Artur K. Ekert. "Quantum cryptography based on Bell's theorem". In: *Phys. Rev. Lett.* 67 (6 Aug. 1991), pp. 661–663. doi: 10.1103/PhysRevLett.67.661.
- [18] Lance Fortnow. "The status of the P versus NP problem". In: *Commun. ACM* 52.9 (Sept. 2009), pp. 78–86. ISSN: 0001-0782. doi: 10.1145/1562164.1562186.
- [19] T Gaebel et al. "Stable single-photon source in the near infrared". In: *New Journal of Physics* 6 (Jan. 2004), pp. 98–98. doi: 10.1088/1367-2630/6/1/098.
- [20] W. B. Gao et al. "Observation of entanglement between a quantum dot spin and a single photon". In: *Nature* 491.7424 (Nov. 2012), pp. 426–430. ISSN: 0028-0836.
- [21] S. Gee et al. "High-precision measurement of free spectral range of etalon". In: *Electronics Letters* 42.12 (June 8, 2006), pp. 715–716. doi: 10.1049/el:20060652.
- [22] Goldreich. *P, NP, and NP-Completeness*. Cambridge University Press, 2010. ISBN: 9781139490092.
- [23] Philippe Grangier, Barry Sanders, and Jelena Vuckovic. "Focus on Single Photons on Demand". In: *New Journal of Physics* 6 (Jan. 2004). doi: 10.1088/1367-2630/6/1/E04.
- [24] G. Hernandez. *Fabry-Perot Interferometers (Cambridge Studies in Modern Optics)*. Cambridge University Press, 1988. ISBN: 9780521368124.
- [25] Ulrike Herzog, Matthias Scholz, and Oliver Benson. "Theory of biphoton generation in a single-resonant optical parametric oscillator far below threshold". In: *Phys. Rev. A* 77 (2 Feb. 2008), p. 023826. doi: 10.1103/PhysRevA.77.023826.
- [26] David Höckel. "Narrow-Band Single Photons as Carriers of Quantum Information". PhD thesis. Humboldt-Universität zu Berlin, Oct. 1, 2010.
- [27] David Höckel and Oliver Benson. "Electromagnetically Induced Transparency in Cesium Vapor with Probe Pulses on the Single-Photon Level". In: *Phys. Rev. Lett.* 105 (15 Oct. 2010), p. 153605. doi: 10.1103/PhysRevLett.105.153605.
- [28] C. K. Hong and L. Mandel. "Theory of parametric frequency down conversion of light". In: *Phys. Rev. A* 31 (4 Apr. 1985), pp. 2409–2418. doi: 10.1103/PhysRevA.31.2409.
- [29] C. K. Hong, Z. Y. Ou, and L. Mandel. "Measurement of subpicosecond time intervals between two photons by interference". In: *Phys. Rev. Lett.* 59 (18 Nov. 1987), pp. 2044–2046. doi: 10.1103/PhysRevLett.59.2044.

- [30] Satoshi Horie and Osamu Watanabe. "Hard instance generation for SAT". In: *Algorithms and Computation. Algorithms and Computation: 8th International Symposium, ISAAC'97, Singapore, December 17-19, 1997, Proceedings. (Lecture Notes in Computer Science)*. Ed. by Hon Wai Leong, Hiroshi Imai, and Sanjay Jain. 1350 vols. Lecture Notes in Computer Science. Springer, 1997, pp. 22–31. ISBN: 9783540638902.
- [31] M Houe and P D Townsend. "An introduction to methods of periodic poling for second-harmonic generation". In: *Journal of Physics D: Applied Physics* 28.9 (Sept. 1995), pp. 1747–1763. doi: 10.1088/0022-3727/28/9/001.
- [32] Bruno Huttner and Asher Peres. "Quantum Cryptography with Photon Pairs". In: *Journal of Modern Optics* 41.12 (Dec. 1994), pp. 2397–2403. doi: 10.1080/09500349414552241.
- [33] Kyo Inoue, Edo Waks, and Yoshihisa Yamamoto. "Differential Phase Shift Quantum Key Distribution". In: *Phys. Rev. Lett.* 89 (3 June 2002), p. 037902. doi: 10.1103/PhysRevLett.89.037902.
- [34] David Kahn. *The Codebreakers: The Comprehensive History of Secret Communication from Ancient Times to the Internet*. Scribner, 1996. ISBN: 0684831309.
- [35] Auguste Kerkhoffs. "La cryptographie ilitaire". In: *Journal des sciences militaires* (1883).
- [36] Lars Koch. "Doppelresonanter Optisch Parametrischer Oszillatator zur Erzeugung schmalbandiger Einzelphotonen". Diplomarbeit. Humboldt-Universität zu Berlin, 2009.
- [37] Evgeny Kovalchuk. "Optical parametric oscillators for precision IR spectroscopy and metrology". PhD thesis. Humboldt-Universität zu Berlin, Dec. 22, 2006.
- [38] Tim Kroh. "Charakterisierung von Quantenpunkt-Einzelphotonen für Quantenrepeater-Anwendungen". MA thesis. Humboldt-Universität zu Berlin, Oct. 31, 2012.
- [39] MagiQ. Q Box. Aug. 14, 2013. url: <http://www.magiqtech.com/>.
- [40] T. H. Maiman. "Stimulated Optical Radiation in Ruby". In: *Nature* 187.4736 (Aug. 6, 1960), pp. 493–494. doi: 10.1038/187493a0.
- [41] Leonard Mandel and Emil Wolf. *Optical Coherence and Quantum Optics*. Cambridge University Press, 1995. ISBN: 0521417112.
- [42] Fabio Massacci and Laura Marraro. "Logical Cryptanalysis as a SAT Problem". In: *Journal of Automated Reasoning* 24 (1-2 Feb. 1, 2000), pp. 165–203. doi: 10.1023/A:1006326723002.
- [43] Christian Maurer et al. "A single-photon source based on a single Ca + ion". In: *New Journal of Physics* 6.1 (2004), p. 94.
- [44] P. Michler. "A Quantum Dot Single-Photon Turnstile Device". In: *Science* 290.5500 (Dec. 2000), pp. 2282–2285. doi: 10.1126/science.290.5500.2282.
- [45] Frank Miller. *Telegraphic code to Insure Privacy and Secrecy in the Transmission of Telegrams*. Charles M. Cornwell, New York, 1882.

- [46] W E Moerner. "Single-photon sources based on single molecules in solids". In: *New Journal of Physics* 6 (Jan. 2004), pp. 88–88. doi: 10.1088/1367-2630/6/1/088.
- [47] Sir Isaac Newton. *Opticks or a treatise of the reflections, refractions, inflections and colours of light*. Printed for Sam. Smith, and Benj. Walford, Printers to the Royal Society, at the Prince's Arms in St. Paul's Church-yard, 1704.
- [48] Z. Y. Ou and Y. J. Lu. "Cavity Enhanced Spontaneous Parametric Down-Conversion for the Prolongation of Correlation Time between Conjugate Photons". In: *Phys. Rev. Lett.* 83 (13 Sept. 1999), pp. 2556–2559. doi: 10.1103/PhysRevLett.83.2556.
- [49] Zhe-Yu Jeff Ou. *Multi-Photon Quantum Interference*. Springer, 2007. ISBN: 038725532X.
- [50] I. Ozdur et al. "Modified Pound-Drever-Hall scheme for high-precision free spectral range measurement of Fabry-Perot etalon". In: *Electronics Letters* 44.15 (July 17, 2008), pp. 927–928. doi: 10.1049/el:20080647.
- [51] Pantita Palittapongarnpim, Andrew MacRae, and A. I. Lvovsky. "Note: A monolithic filter cavity for experiments in quantum optics". In: *Review of Scientific Instruments* 83.6, 066101 (June 7, 2012), p. 066101. doi: 10.1063/1.4726458.
- [52] Matthew P Peloso et al. "Daylight operation of a free space, entanglement-based quantum key distribution system". In: *New Journal of Physics* 11.4 (Apr. 2009), p. 045007. doi: 10.1088/1367-2630/11/4/045007.
- [53] A. Pérot and Ch. Fabry. "Sur les franges des lames minces argentées et leur application a la mesure de petites épaisseurs d'air." In: *Annales de chimie et de physique* 12 (1897), pp. 459–501.
- [54] A. M. Prokhorov. "Molecular amplifier and generator for submillimeter waves". In: *Journal of Experimental and Theoretical Physics* 34 (June 1958). Sov. Phys. JETP, vol. 7, pp. 1140–1141, December 1958., 1658–1659.
- [55] Edward Mills Purcell. "Spontaneous Emission Probabilities at Radio Frequencies". In: *Proceedings of the American Physical Society* 69 (11-12 June 1946), pp. 674–674. doi: 10.1103/PhysRev.69.674.2.
- [56] ID Quantique. *Cerberis and Clavis*. ID Quantique. Aug. 14, 2013. URL: <http://www.idquantique.com/>.
- [57] Charles Santori et al. "Indistinguishable photons from a single-photon device". In: *Nature* 419.6907 (Oct. 2002), pp. 594–597. doi: 10.1038/nature01086.
- [58] Charles Santori et al. "Single-photon generation with InAs quantum dots". In: *New Journal of Physics* 6 (Jan. 2004), pp. 89–89. doi: 10.1088/1367-2630/6/1/089.
- [59] A. L. Schawlow and C. H. Townes. "Infrared and Optical Masers". In: *Physical Review A* 112 (6 Dec. 15, 1958), pp. 1940–1949. doi: 10.1103/PhysRev.112.1940.
- [60] Matthias Scholz. "New Light Sources for Quantum Information Processing. Single Photons from Single Quantum Dots and Cavity-Enhanced Parametric Down-Conversion". PhD thesis. Humboldt-Universität zu Berlin, Jan. 22, 2009.
- [61] M. Scholz et al. "Narrow-band single photons from a single-resonant optical parametric oscillator far below threshold". In: *Applied Physics Letters* 91.19 (2007), p. 191104. doi: 10.1063/1.2803761.

- [62] Claude E. Shannon. "Communication Theory of Secrecy Systems". In: *Bell System Technical Journal* 28 (1949).
- [63] Anthony E. Siegman. *Lasers*. University Science Books, 1986. ISBN: 0935702113.
- [64] Glenn S. Solomon et al. "Manipulating single photons from disparate quantum sources to be indistinguishable". In: *J. Opt. Soc. Am. B* 29.3 (Mar. 2012), pp. 319–327. doi: 10.1364/JOSAB.29.000319.
- [65] Daniel A Steck. "Cesium D line data". In: *Los Alamos National Laboratory* (2003).
- [66] Damien Stucki et al. "Fast and simple one-way quantum key distribution". In: *Applied Physics Letters* 87.19 (2005), p. 194108. doi: 10.1063/1.2126792.
- [67] D. Stucki et al. "Continuous high speed coherent one-way quantum key distribution". In: *Optics Express* 17.16 (2009), pp. 13326–13334.
- [68] M Vaughan. *The Fabry-Perot Interferometer: History, Theory, Practice and Applications (Series in Optics and Optoelectronics)*. 1st ed. Taylor & Francis, Jan. 1989. ISBN: 9780852741382.
- [69] Michael Wahl et al. "An ultrafast quantum random number generator with provably bounded output bias based on photon arrival time measurements". In: *Applied Physics Letters* 98.17, 171105 (2011), p. 171105. doi: 10.1063/1.3578456.
- [70] Herbert Walther et al. "Cavity quantum electrodynamics". In: *Reports on Progress in Physics* 69.5 (May 2006), pp. 1325–1382. doi: 10.1088/0034-4885/69/5/R02.
- [71] Stephen Wiesner. "Conjugate coding". In: *ACM SIGACT News* 15.1 (Jan. 1983), pp. 78–88. doi: 10.1145/1008908.1008920.
- [72] F. Wolfgramm et al. "Bright filter-free source of indistinguishable photon pairs". In: *Opt. Express* 16.22 (Oct. 2008), pp. 18145–18151. doi: 10.1364/OE.16.018145.
- [73] W. K. Wootters and W. H. Zurek. "A single quantum cannot be cloned". In: *Nature* 299.5886 (Oct. 1982), pp. 802–803. doi: 10.1038/299802a0.
- [74] Zhen-Sheng Yuan et al. "Experimental demonstration of a BDCZ quantum repeater node". In: *Nature* 454.7208 (Aug. 2008), pp. 1098–1101. ISSN: 0028-0836.
- [75] M. Żukowski et al. "Event-ready-detectors" Bell experiment via entanglement swapping". In: *Phys. Rev. Lett.* 71 (26 Dec. 1993), pp. 4287–4290. doi: 10.1103/PhysRevLett.71.4287.
- [76] Valéry Zwiller, Thomas Aichele, and Oliver Benson. "Quantum optics with single quantum dot devices". In: *New Journal of Physics* 6 (Jan. 2004), pp. 96–96. doi: 10.1088/1367-2630/6/1/096.